PHYSICO-CHEMICAL STUDIES IN FLOW ANALYSIS

by

F.E. POWELL, B.Sc., M.Sc., Dip.Ed., C.Chem., F.R.S.C.

A Doctoral Thesis

Submitted in partial fulfilment of the requirements for the award of the Doctor of Philosophy Degree of the Loughborough University of Technology.

DEDICATION

To my wife, June, to whom I owe everything.

ACKNOWLEDGEMENTS

The author wishes to express his grateful thanks to the Governors and Principal of the Humberside College of Higher Education for the provision of equipment and facilities; to his supervisor Dr. Arnold Fogg for help and encouragement; to Mr. Tim Simmonds for assistance with computing and to Mr. Douglas Hankin for help in the design and for the construction of the flow injection signal analogue.

ABSTRACT

The first part of this study was the characterisation of an impinging jet electrode in an amperometric detector; the device having found extensive application in flow injection analysis.

A voltammetric study of the detector in the stopped flow mode was carried out and evidence is presented of restricted diffusion imposed by the shallow depth of the cell. In hydrodynamic voltammetry, the detector exhibited a gradual progression from thin-layer to wall-jet behaviour as the flow rate increased. This gradation is discussed in terms of a model in which flow in the electrode chamber forms concentric rings, the streamlines being successively perpendicular, oblique and parallel to the electrode.

The response of the detector and its associated equipment was studied by two experiments. Firstly, the fidelity of the electrochemical instrumentation and recording system was ascertained from its electronic response to a RC (resistance-capacitance) circuit functioning as a flow injection transport analogue. Secondly, the dynamic response of the electrochemical cell was established from an experiment using a concentration step input delivered through a short, straight manifold. The results indicated that laminar flow in the delivery tube was modified by mixing stages in the cell channel and its connections to produce a final dispersion which defines an effective detection volume of only 7μL. The electronic and cell responses indicate that the total detection system would impose little extra dispersion in a practical flow injection line.

In the second part of this study, photometric titrations were carried out in a stirred tank reactor in which the volume changed linearly with time. The general relation for the concentration gradient when the tank is used as a mixing device was examined experimentally under various flow conditions. In particular, the precision of linear concentration gradients was ascertained when peristaltic pumping was employed. These gradients were utilised to titrate analyte within the tank by means of titrant delivered by pump flow with photometric detection in an exit stream. Self-indicating titrations, following changes in the absorbance of analyte, titrant or reaction product, were perfomed each conforming to theoretical prediction. Due to the external detection system employed, dispersion and transportation lag effects were observed and accounted for.

CONTENTS

SECTION ONE

INTRODUCTION

1.1 Perspectives in Flow Analysis

Flow analysis appears in a number of different guises. Flow may be a prerequisite for the proper functioning of the sensing element; the natural matrix may be a flowing medium or flow may be used to transport sample so as to achieve a degree of automation in the analysis.

The central theoretical problem in these methods is the spatial and temporal distribution of the analyte in the flow regime. This dispersion arises from the twin spontaneous processes of momentum transfer due to viscosity and mass transfer due to diffusion, and must satisfy the generalised differential equation (1):

$$\frac{\partial C}{\partial t} = D\nabla^2 C - \text{grad}\,(UC) \qquad 1.1$$

D is the analyte diffusion coefficient, C the concentration at time t, U is the linear velocity of the flow, and ∇^2 is the Laplace operator. The first term on the right hand side admits the diffusion process and the second the convective process.

1.1.1 Flow sensitive sensors

In steady-state voltammetry, reproducible response is achieved by the establishment of a constant diffusion layer thickness through the relative movement of fluid and electrode. Historically, this condition was first realised by means of a moving sensor, notably the dropping mercury electrode and rotating platinum electrode. Later, the motion was produced in a flowing liquid with a stationary electrode in a technique popularly known as hydrodynamic voltammetry which reached maturity following the pioneering theoretical work of Levich (2).

Flow methods offer improved performance of ion-selective electrodes because of the permanent conditioning of the sensor membrane, stable liquid junction and streaming potentials, lower response time and freedom from contamination from membrane components which are washed away (3).

Because of these inherent attributes, both voltammetric and potentiometric sensors figure prominently in flow analysis. In addition to these electrochemical methods, flame spectroscopic techniques also employ transport to deliver sample in a reproducible manner.

1.1.2 On-line analysis

In on-line analysis, the flowing liquid may be chemically and physically homogeneous for long periods of time as in process streams, water and effluent monitoring or the analyte may occur in discrete slugs in the flowing medium as in liquid chromatography. The successful detection unit in these systems should have a short response time relative to the changing analyte concentration profile. On the other hand, these various applications impose differing criteria on detector performance; control operations in the plant or in the field demand stable, rugged and easily calibrated detectors, whereas in laboratory situations less robust devices can be tolerated if of sufficient sensitivity, accuracy and precision. Although in clinical situations, such as flowing blood, all criteria have to be met concurrently.

1.1.3 Discrete sample flow analysis

Flow may be utilised to transport a discrete sample to a detector often with chemical reactions and other analytical operations engineered to occur in transit. In this way, samples can be processed sequentially, on the conveyor belt principle, to achieve automation. The earliest application of this philosophy used sample segments separated by air bubbles (4). Later, samples in a non-segmented stream were successfully analysed (5); and by confining convective and diffusive mixing to a narrow tube flow manifold, a high sample throughput was achieved by this technique, subsequently called flow injection analysis (6).

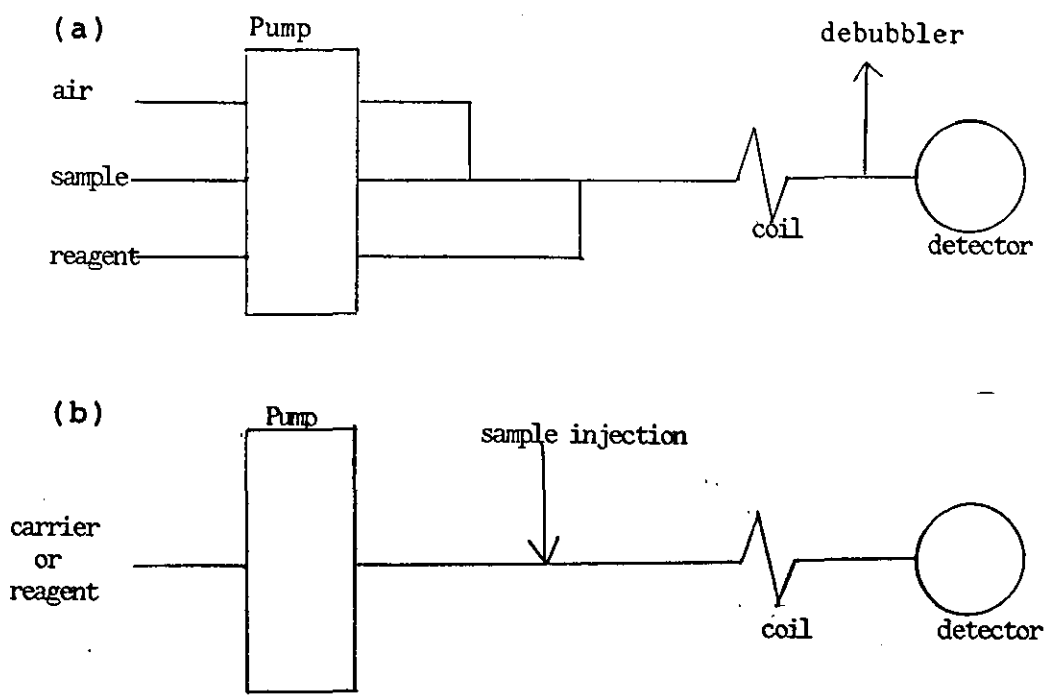

Fig. 1.1 Schematic flow manifolds for (a) Segmented Flow Analysis, SFA and (b) Non- segmented Flow or Flow Injection Analysis, FIA.

Common features of these two methods include propulsion and detection units and a coil allowing delay for reactions to occur. Provision can also be made in the lines for various separation operations such as dialysis and solvent extraction.

The essential difference between the techniques lies in the use of air bubbles in segmented flow. The differing flow patterns that result are shown schematically in Fig 1.2 along with the transient signals they produce at the detector.

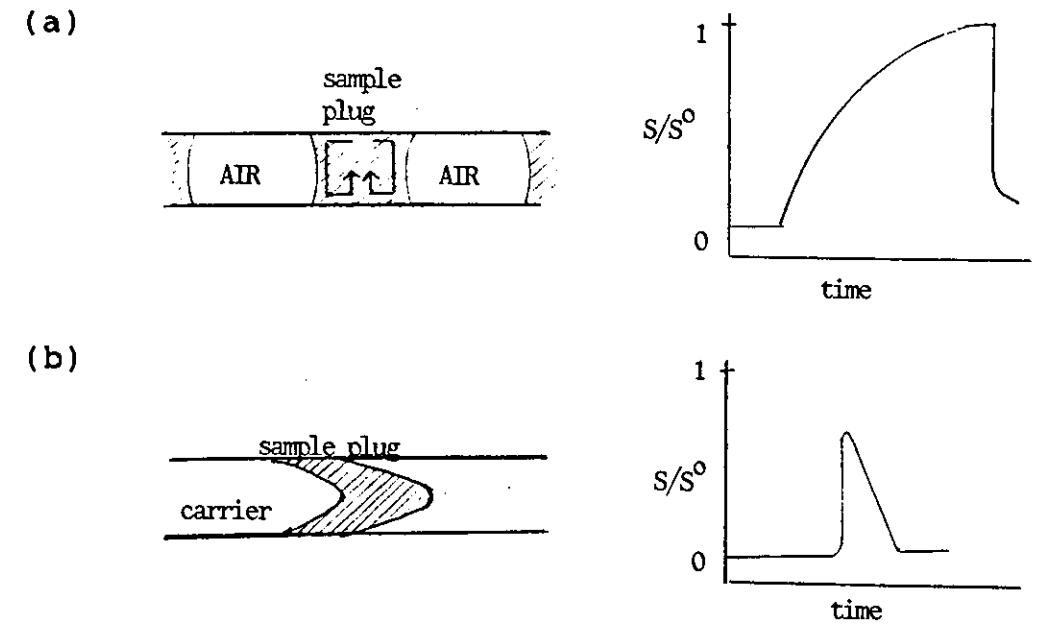

Fig 1.2 Schematic flow patterns (a) SFA (b) FIA. S^{o} is a steady-state signal.

In each case the analyte concentration is related to a peak height; although in FIA, peak width also may be used an an index of concentration, but with less precision (7). In SFA, the air bubbles compress the sample plug and induce turbulence which homogenises the zone so that a full steady state signal is attained. In FIA on the other hand, dispersion by convective and diffusive mixing of the sample plug into the flow occurs but this is incomplete and the steady-state is not attained. Essentially, SFA and

FIA are kinetic techniques whose reproducibility is attained by the consistent hydrodynamic conditions met in the flow manifold. Inherently, FIA is less sensitive than SFA because of the lower signal generated.

The differing flow regimes also impose different sampling techniques. In SFA, the sample is aspirated into the line using a withdrawal pipette to introduce air bubbles. The injected volume may be controlled by using the pipette in fixed time or fixed volume modes. Typically, these volumes range from 0.2 and 2 ml and are accommodated in wide manifold tubing of ca. 2 mm bore. In FIA, sample volumes are introduced from a loop by rotary or sliding valves. Smaller volumes of between 10-100 µl can be delivered reproducibly and narrow manifold tubing can be employed, which serves to curtail excessive dispersion. Inherently, FIA possess a higher sample throughput than SFA and this difference is amplified by the necessity of using a wash solution between sample plugs in SFA if cross-contamination is to be avoided. Peristaltic pumping is usually employed to propel the streams in both techniques. This is an advantage in SFA as it induces compression; however it is not a necessity in FIA and other methods can be employed, e.g. pressure regulated hydrostatic flow can be used if pulsation is undesirable.

A complex, commercial instrument, the Technicon Auto-Analyzer, has been developed to meet the demanding requirements of SFA. This achieved practical success, particularly in medicine as an instrument dedicated to analysing similar samples in a busy laboratory. This function is challenged by FIA because of its simplicity and low cost.

In addition to its attribute in automated analysis, FIA also possess features which may enhance general methodologies. Thus analyses based on empirical procedures may be more reproducible in the fixed time context of FIA than in a traditional batch mode (8), standard addition calibrations can be performed economically (9), also kinetic and thermodynamic information can be gathered at a fast rate (10,11). Because of this potential, considerable research activity exists in FIA and a number of innovations may be mentioned:-

(i) Economies have been achieved by limiting the amount of reagent consumed by injecting sample and reagent simultaneously into carrier streams which subsequently merge (12). Similarly, if the sample is plentiful and cheap, the reagent may be injected into the flowing sample in a reverse-FIA manner. This variation of the method could be employed profitably in process control (13,14). On the other hand in clinical chemistry, the amount of sample available is frequently small and in limited supply, for this situation a programmed probe has been developed which withdraws reagent and sample alternately without loss of the latter (15).

(ii) Flow variations have been investigated in attempts to increase the scope of the method. In the stopped flow mode, the sample plug is stationary in the detector and greater sensitivity may be obtained for slow reactions or kinetic analysis may be performed on the fiagram (16). Scan techniques, such a linear voltage sweep voltammetry may also be utilised providing scope for simultaneous analysis and speciation studies (17).

Multiple pass flow methods have been used in which a reacting plug circulates many times through a closed sub-loop manifold containing the detector, producing a set of fiagrams which contain kinetic information (18) and flow reversal though delay coils affords an economic method of varying the residence time in a simple manifold (19).

(iii) On-line separation techniques have been developed using a variety of separation steps adapted to flow conditions. Calcium has been extracted from milk into a cresolphthalein complexone colorimetric reagent stream using dialysis (20). Thiochrome, the oxidation product of Vitamin B_1, has been extracted from an aqueous line into chloroform and estimated fluorimetrically (8); and the free fatty acid content of oils has been determined by the reverse phase separation into an aqueous stream (21). Non-aqueous samples have also been handled by utilising the enhanced reactivity existing at the interface of water/oil emulsions (22). Phase separation without special segmentation apparatus has been achieved by injecting a plug of non-aqueous extracting solvent into a sample stream in a r-FIA manner and reversing the flow of the organic plug through an optical detector until maximum extraction is obtained (23).

Precipitation reactions have been utilised in FIA, by means of a reaction coil followed by a filter, which is cleaned by a subsequent dissolution wash step (24). In a similar way activated alumina has been used to pre-

concentrate oxyanions by adsorption, before elution with alkali into an ICP-AES detector (25).

(iv) Solid reactors have been used in various forms. The selectivity and economy of immobilised enzymes has been utilised by many workers following an early study on glucose, ethanol and testosterone (26). A Cd column was used to reduce nitrate to nitrite followed by its determination by the Griess reaction (27) and an ion-exchange column in the CNS^- form was used as a general anion analyser by estimating the CNS^- released photometrically after reaction with Fe(III) (28).

(v) Simultaneous analysis of multicomponent samples has been achieved using a number of detectors arranged sequentially or in parallel (29). More economic are arrangements using a single detector with splitting of the flow line into streams of differing residence times so that the sample is resolved into peaks. This type of manifold has been employed to exploit differential kinetic effects and determine both pyridoxal and its 5-phosphate derivative after oxidation (30). Alternatively each stream may be subject to different chemistries so that the peaks contain different analytical information. Thus sucrose and glucose were determined together in soft drinks using a bifurcated manifold in which one path only involved inversion (31).

1.2 Dispersion and Mixing

Mixing effects, whether natural or enforced, underpin many aspects of flow analysis and appreciation of them is a matter of necessity.

1.2.1 Enforced mixing

A continuous stirred tank reactor (CSTR), properly operated, is a practical unit providing perfect mixing. Fig. 1.3 shows such a reactor of constant volume V_o in schematic form and in form finding application in analysis.

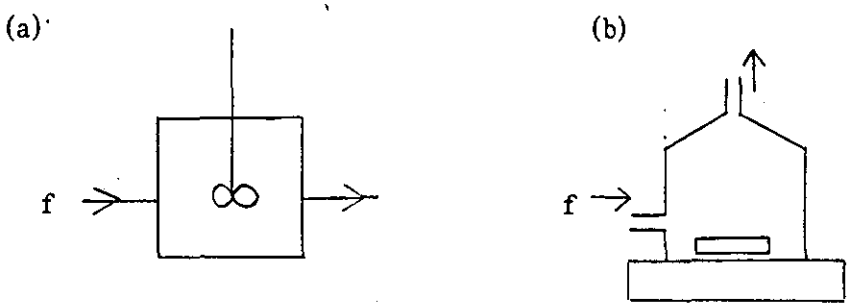

Fig. 1.3 Constant Volume CSTR
(a) Schematic representation, (b) Magnetically stirred chamber.
f is the constant flow rate through the tank.

Elements of fluid passing through the tank have a statistical distribution of exit times. Thus a unit impulse input displays a relative time distribution or E curve of exit times. For an ideal CSTR this distribution is given by $e^{-t/\tau}/\tau$ (32), where τ is the mean residence time (V_o/f). Concentration gradient transients from the tank for real situations can be obtained by integrating this distribution. In particular, the situations given below are of significance in flow analysis:

(i) Feed or F curve

$$F = \int_0^t E dt$$

Input: infinite plug of solution
Concentration of solute in input = C^o
Original concentration of solute in tank = 0
Transient concentration of solute in tank = C

Integration gives:

$$C = C^{o} (1 - e^{-t/\tau}) \qquad 1.2$$

(ii) Wash or W curve

$$W = \int_{t}^{\infty} E dt$$

Input: pure solvent

Original concentration of solute in tank = C^{o}

Transient concentration of solute in tank = C

Integration gives:

$$C = C^{o} e^{-t/\tau} \qquad 1.3$$

The F curve has been employed as a well defined concentration profile to perform continuous calibration of atomic absorption (9), ion-selective electrode (33) and liquid chromatography (34) equipment. In a similar way, serial dilution of a flowing protein solution by merging with a reagent gradient has been achieved in a rapid manner in the study of protein binding equilibria (35).

In their version of FIA, Pungor and co-workers have consistently used a stirred tank in an effort to achieve reproducible mixing of an injected sample with an inert carrier before presentation to the detector (36). Assuming plug flow in the transmission line, the transient from an input sample of volume V_s, follows the F curve from the time the plug enters the chamber to a time V_s/f when all the plug has entered, from whence the sample is washed out by the carrier (Fig. 1.4b). When the sample plug is intercalated in a reagent stream, reaction modifies the signal to that shown in Fig. 1.4c (37).

From the time the sample enters the tank, an induction period t_1 occurs, when all the analyte reacts with reagent occupying the tank. In the next period, analyte is in excess and accumulates until at t_2 all the sample volume V_s has entered the tank. Finally, the entering reagent stream both reacts with and washes out the analyte. Mathematical analysis shows the total transient time (Δt) to be logarithmically related to the analyte concentration:

$$\Delta t = \tau \ln C_A^{\circ} - \text{constant} \qquad 1.4$$

This theoretical treatment gives good account of an actual trial system in which triodiode is injected into a thiosulphate stream with amperometric monitoring (38). A similar equation but with a different constant term was derived based on the simplistic assumption of instant dispersal of the injected sample in the chamber followed by an exponential wash out (39). The equation 1.4 has further relevance in so called FIA titrations discussed in section 1.4.3

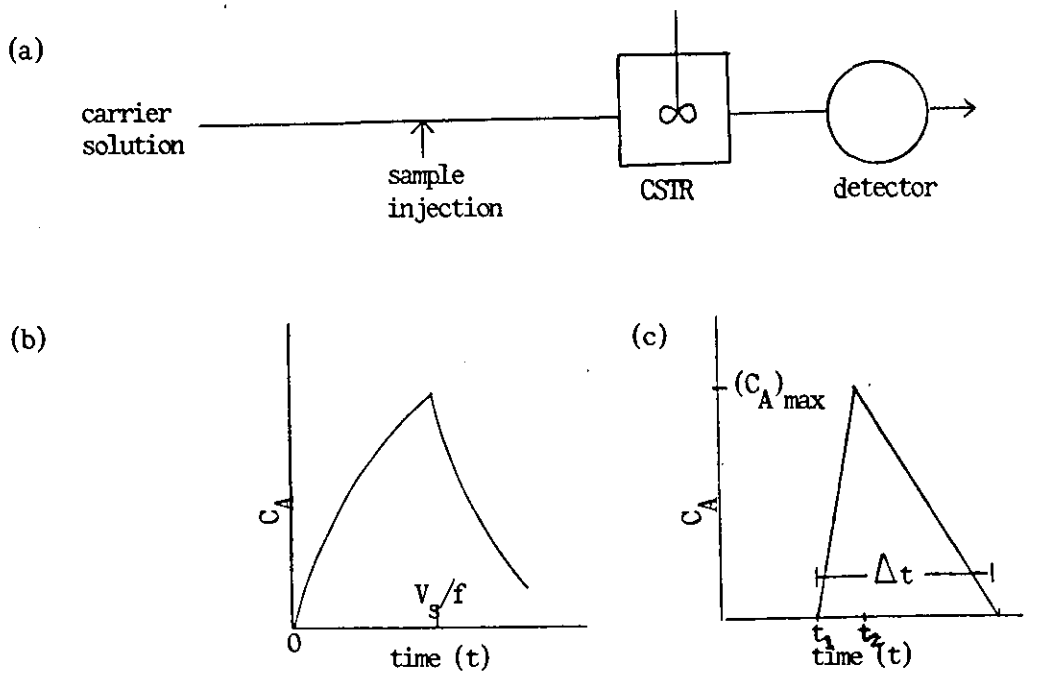

Fig. 1.4 Schematic manifold and transients with in-line CSTR

(a) Manifold

A volume V_s of sample containing analyte at concentration C_A^o is injected into a carrier flowing at a rate f and is dispersed in a mixing tank of residence time, τ.

(b) Dispersion without reaction (36)

Transient follows F curve given by:

$C_A = C_A^o (1 - e^{-t/\tau})$, up to V_s/f,

subsequently following W curve given by:

$C_A = C_A^o (1 - e^{-Vs/f}) e^{-(t-Vs/f)/\tau}$

(c) Dispersion with reaction (37)

Carrier contains reagent at concentration C_R^o. Reaction between analyte and reagent is

$A + R \rightarrow$ products.

After an induction period t_1, analyte accumulates at a rate given by:

$C_A = C_A^o (1 - e^{-(t-t_1)/\tau})$, reaching a maximum $(C_A)_{max}$ at t_2. Whereafter analyte is removed by reaction and washing out at a rate given by:

$C_A = (C_A)_{max} e^{-(t-t_2)/\tau} - C_R^o (1 - e^{-(t-t_2)/\tau})$.

Δt is the total transient time and is given by equation 1.4

Another use of the mixing chamber in the FIA context is the performance of matrix compensation on the delivered sample by dilution in the tank; and because of the low frequency of the ensuing output compared with normal FIA signals, downstream reagent can be employed in a reverse-FIA manner. The method is useful in handling samples directly in on-line situations (40).

Despite these achievements, the use of mixing chambers in FIA is not without its critics. The main reservation is that peak broadening occurs at the expense of peak height, so reducing sampling frequency and producing an unfavourable ratio between base line noise and recorded signal (41). However, whatever the practical merits of the CSTR, the notion of the device as a perfect mixing stage and its mathematical description play prominent parts in theories of chemical transport processes, conceptually parallel to the theoretical plate concept in chromatography.

Methods of less active mixing producing reduced dispersion of sample in the carrier stream have been sought. Single bead string reactors in which the flow meanders around impervious glass beads of diameter slightly less than that of the tube (42); coiled or knotted tubing, where secondary flow patterns due to centrifugal forces induce mixing (43), are both partially successful in this regard. The mixing of confluent streams has also received serious attention and various tee-piece configurations have been described sometimes incorporating a small passive chamber (44,45). A tee with each entry line making a 30^{o} angle with the merged stream is particularly effective (46). A drip

vessel, in which confluent streams merge in a drop whose rotation and splashing effectively mix the components has been described (47), but is less commonly used.

1.2.2 Dispersion in continuous streams

Taylor (48) examined the dispersion of a moving interface into the flow occurring in a straight tube of circular cross-section. Equation 1.1 was solved analytically for the extreme cases of pure convective dispersion in laminar flow called the Taylor A region, and for longitudinal diffusion in the absence of momentum transfer constituting the Taylor B region (48). In the intermediate case of combined convection/diffusion, numerical solution is necessary (49-55). Theoretical and practical work, on both bolus and infinite plug injections, are in broad accord and can be summarised schematically by the profiles displayed by the injection of an impulse of material:

(a) Flow profile

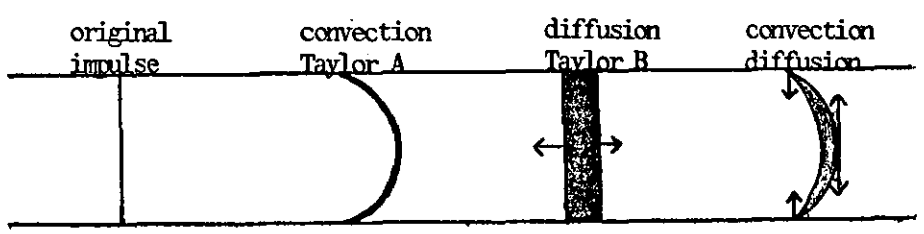

(b) Concentration profile

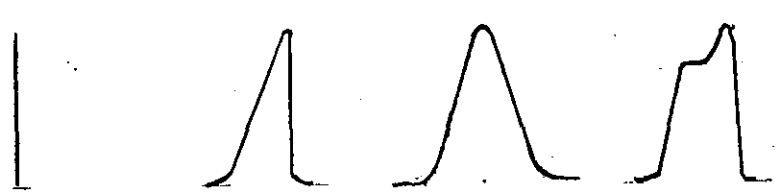

Fig. 1.5 Flow and Concentration Profiles of an injected impulse of material

Characteristically, pure convection results in a concentration profile with an extended tail whereas pure longitudinal diffusion produces a Gaussian profile of more limited dispersion. Taylor A behaviour is encouraged by short tubes and high flow rates and Taylor B by the opposite conditions. In the final case, radial diffusion mitigates against the effects of convection and dispersion is again curtailed. Also in this case humps may appear in the concentration profile indicative of the dual nature of the mixing process, although the slightest turbulence or pulsation tends to smooth these out (54). Reaction of sample with reagent can be treated by including a rate expression in equation 1.1, numerical solution of which again predicts humped peaks and were observed in carefully straightened tubes (56).

The hydrodynamic domains in which these effects operate are mapped out in Fig. 1.6, following Anathakrishnan et al. (49).

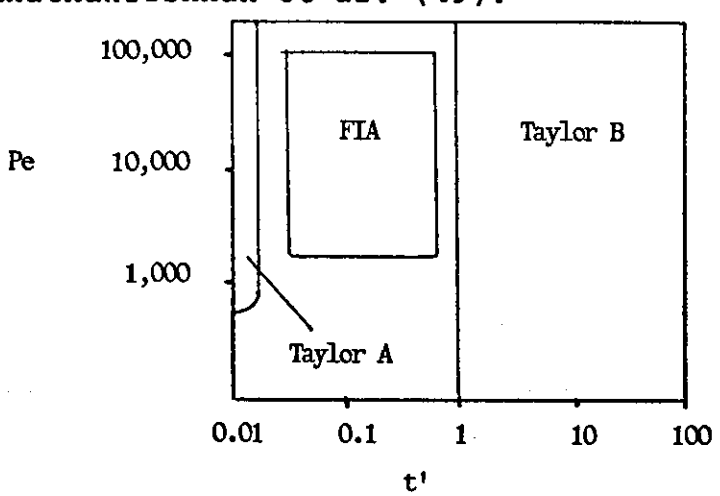

Fig 1.6 Hydrodynamic map for dispersion in a laminar stream. Pe is the Peclet Number ($U_o a/D$) and t' the reduced time (Dt/a^2); a is the tube radius; Uo is the maximum linear velocity and D is the solute diffusion coefficient.

The Peclet number is an index of convective/diffusion components and the reduced time is indicative of the time scale of the experiment. As indicated, normal FI conditions are intermediate between Taylor A and Taylor B behaviour (57).

The time between the injection of sample and appearance of the signal also contains information about the flow in the manifold. Thus for plug flow, the appearance time (t_A) is determined by the mean flow rate, but for laminar flow t_A is one-half of this value since here the central leading front moves at twice the mean flow rate. In the convection/diffusion region, it was proposed that (54):

$$t_A \text{ (theory)} = 109\ a^2\ D^{0.025}\ (L/f)^{1.025} \qquad 1.5$$

where L is the tube length and f the volumetric flow rate. However to obtain concordance with experimental results, an accommodation factor (ϕ) had to be introduced (54):

$$t_A \text{ (expt)} = \frac{t_A \text{(theory)}}{\phi} \qquad 1.6$$

This treatment has been criticised by Gomez-Nieto et al. (58) since on application to an extensive set of fresh experimental data, ϕ was found to be sensitive to L and f. However, it has been pointed out that these latter results are not self-consistent as the appearance times obtained in some instances exceed the plug flow limit, implying the presence of stagnant mixing zones in the manifold (59).

Early in the development of FI techniques, it was recognised that peak height was an obvious measure of dispersion. Accordingly, a dispersion coefficient (D_s) was defined (41):

$$D_s = \frac{C^o}{C_{max}} \qquad 1.7$$

C^o is the original concentration of injected sample and C_{max} is the concentration at the apex of the FI transient (Fig. 1.2). This empirical approach has been universally adopted and has proved a fruitful description of real flow manifolds comprising coiled reactors, connectors, etc.

In a theoretical approach to these real manifolds, models based on mixing tanks have been one way forward. Tyson et al. (7,60) has favoured a single tank mode, whereas Ruzicka et al. (41) proposed a tanks in series array:

(a)

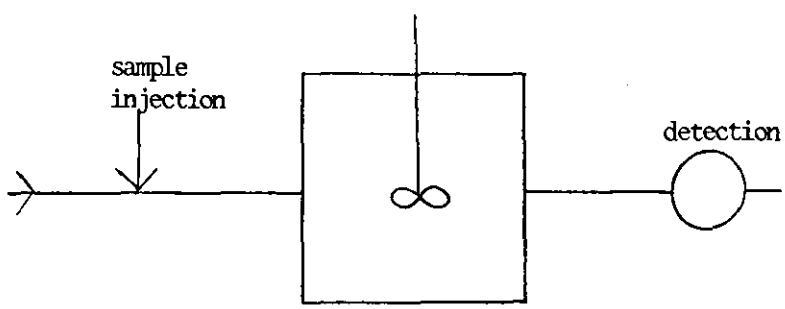

(b)

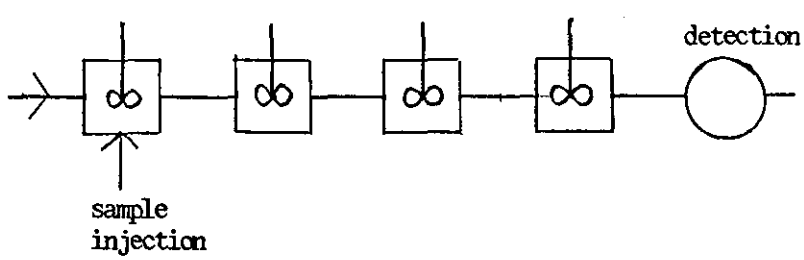

Fig. 1.7 Mixing tanks models of a FI manifold
(a) Single tank model, with injection without mixing
(b) Multiple tank model, with injection step constituting an initial mixing stage.

In each line, mixing is confined to the CSTRs. The single tank model is formally identical to the Pungor real mixing tank manifold (36) and produces a sharp maximum displayed when all of the sample plug has entered the tank. The width of the peak (Δt) when the transient concentration attains the particular value C′ is given by (7):

$$\Delta t = \ln \left[\left(\frac{C^o - 1}{C'} \right)^{1/(Ds-1)} \right] \qquad 1.8$$

where τ is the residence time in the tank.

The tanks-in-series model produces a transient which for n tanks is (61):

$$\frac{C_n}{C^o} = \frac{(t/\tau)^{n-1} \; e^{-t/\tau}}{(n-1)!} \qquad 1.9$$

and is shown plotted in Fig. 1.8

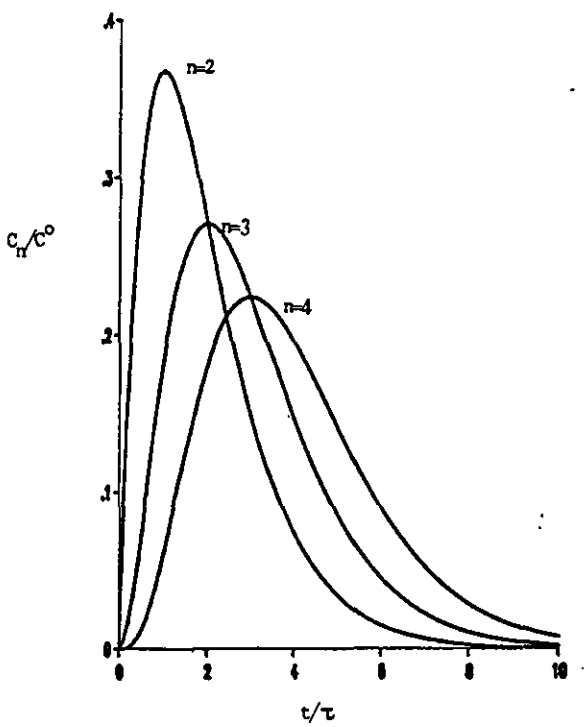

Fig. 1.8 Transients for tanks in series model (n = 2 to n = 4)

These shapes, with their rounded maxima, resemble observed FIA grams and indicate that multimixing stages model the actual dispersion processes more realistically than does a single tank.

The main value of these theories is in the conceptual generalisations they afford for the rationalisation of experimental studies on the effect of residence time and injected volume on D_S, which aid method design. Generally D_S increases with increase in flow rate, tube radius and length and decreasing injected volume (9,41). One disconcerting observation in these studies is that D_S can show minor variation on opening and closing connections, due to irreproducible turbulences (62,63).

The single tank model has been used to treat an interacting sample and reagent stream (64). By a theoretical construction whereby an element of sample plug is mutually exchanged for the same volume of reagent, dispersion arises and the dispersion coefficient of sample (D_S) reagent (D_R) before reaction are mutually related by:

$$D_R = \frac{D_S}{D_S - 1} \qquad 1.10$$

From this relation the ratio of reagent/sample at the peak maximum R_{max} can be related to the original concentration ratios C_R°/C_S°:

$$R_{max} = (C_R^{\circ}/C_S^{\circ})\ (D_S-1) \qquad 1.11$$

Thus if a 10-fold excess of reagent over sample is desired in a manifold of $D_S = 5$, then the original reagent need only be 2.5 times more concentrated than the sample. Further it may be noted that if the

sample concentration exceeds the reagent concentration at the centre of the plug, a twin peaked fiagram will be displayed when the product is monitored, as may be observed when a large sample (500 µL) of Cu(II) is injected into EDTA (64).

Another theoretical approach to FI theory entails adopting a stochastic treatment of the diffusion component occurring along with normal Poiseuille flow and chemical reaction (65). Simulations based on 1500 molecules, although showing considerable statistical noise, allow significant rationalisations to be made. As expected, predictions include a decrease in peak height with residence time in the absence of reaction, and enhanced product formation for large diffusion constants and reaction rates. Other, more subtle, effects are also indicated such as the observation that sample molecules in the plug head are the last to undergo reaction.

All these theories are useful guides to experimentalists, but can be augmented on an empirical basis by optimisation techniques (66,67).

1.3 Detection

In flow analysis, the detection unit will comprise a detector, usually in the form of a flow cell, housing a sensor, with an associated instrument to provide an energy source and possessing signal processing capability. The concentration information in the flow is thus transduced by the detector and suitably registered.

A variety of detection systems have been employed in flow analysis, the more popular can be gaged from citations of FIA applications through the decade from 1974 (68):

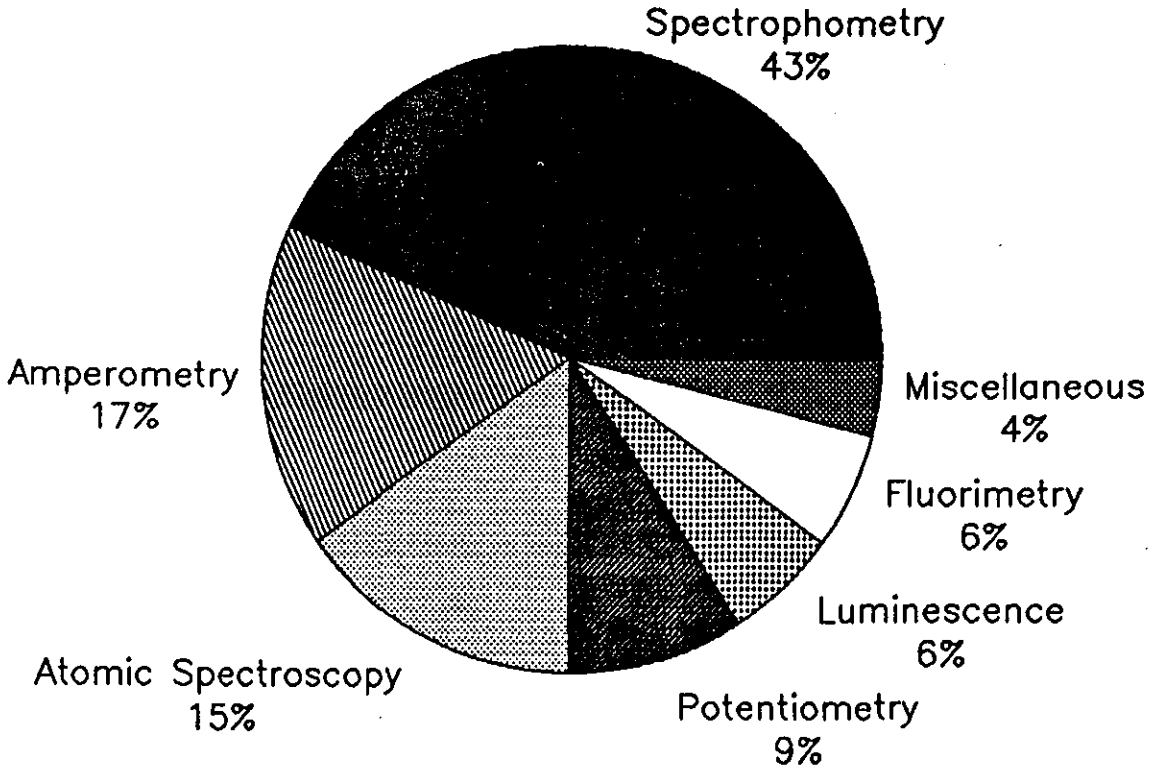

Fig. 1.9 Citations of Detection Systems used in FIA 1974-1984

Universal criteria of detector performance are:-

(i) Sensitivity, or response per unit concentration change.
(ii) Limit of detection, set by an acceptable signal to noise ratio.
(iii) Signal stability and reproducibility.
(iv) Dynamic range, in which the detector responds to analyte concentration, preferably in a linear manner.

In addition, because of the dynamic nature of the signal in flow analysis, detectors may also be characterised by the particular signal average recorded and by their contribution to the variance of the signal.

1.3.1 Flow response

When the concentration profile in the flow is not uniform, alternative concentration averages can be defined which practical devices actually measure or approximate to (57,69):

Fig. 1.10 Concentration Averages in Flow

Volumetric flow rate f, tube radius a, radial distributions of concentration and linear velocity are C(r) and U(r) respectively.

(a) Mean value average concentration, given by

$$\int_0^a (C(r)2\pi r dr)/\pi a^2$$

(b) Bulk average concentration, given by

$$\int_0^a (C(r)U(r)2\pi r dr)/f$$

The mean value average is approximated by some spectrophotometer cells and by emission detectors based on radioactivity and fluorescence.

The bulk average could be obtained by collecting thin fractions, homogenising and determining the concentration. This technique is often employed in residence time distribution studies in chemical plant: hence the alternative name of mixed-cup average. Mass detectors such as continuous titrators

and coulometric devices work on this principle; also detectors in which a degree of mixing precedes the sensing event, e.g. due to the presence of a sharp bend in the entry line, approach this behaviour (57).

The type of average determined by the detector can have a profound effect on the output function for highly dispersed flows. Thus for laminar flow, the parabolic concentration profile of the leading edge of the injecting slug will be modulated differently by each detector:-

Mixed cup detector (61):

$$C/C^o = 1 - t_A^2/t^2 \quad , \quad t > t_A \qquad 1.12$$

Mean value detector (48):

$$C/C^o = 1 - t_A/t \quad , \quad t > t_A \qquad 1.13$$

t_A is the appearance time of the plug, and C^o is the bulk concentration of solute.

In the former case, dispersion is apparently reduced by the mixing step in the detector.

These averages are not always appropriate. Thus in some spectrophotometric cells the optical path is parallel to the flow:

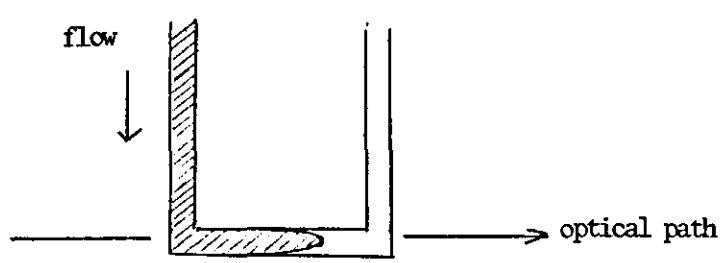

Fig. 1.11 Spectrophotometric cell with longitudinal optical path

Statistical averaging in this case tends to flatten out concentration differences in a profile so that the cell contributes to the apparent dispersion. Surprisingly, the measured dispersion in large cells of this type are flow rate dependent implying the presence of a turbulent region possibly at the bend in the tube (63). This study suggests that response characteristics of most detectors should be examined individually.

Signals contain a distribution of information described by a mean or first moment and by a width described by a variance or second moment, σ^2. The contribution from detector performance to the overall signal width is formally represented by the principle of additivity of variances (69).

$$\sigma^2 \text{ peak} = \sigma^2 \text{ injection} + \sigma^2 \text{ transport} + \sigma^2 \text{ detection} \qquad 1.14$$

The detection variance can be further divided into contributions from the response of detector cell and from the measuring instrumentation (34):

$$\sigma^2 \text{ detection} = \sigma^2 \text{ cell} + \sigma^2 \text{ electronic} \qquad 1.15$$

The cell contribution is usually attributable to finite volume and slow equilibration effects whilst the electronic contribution arises from finite time constants of the circuitry. These operate by broadening the signal, and hence for a given area or amount of analyte reduce the maximum, so increasing the apparent dispersion. As well as this signal degradation, peak width broadening reduces the frequency of analysis of flow methods. These factors are thus best minimised.

The ability of the detector to follow analyte concentration changes is often studied by a dynamic response experiment in which the system is subjected to a concentration step input and the output is monitored from which the response time (τ_D) can be ascertained:

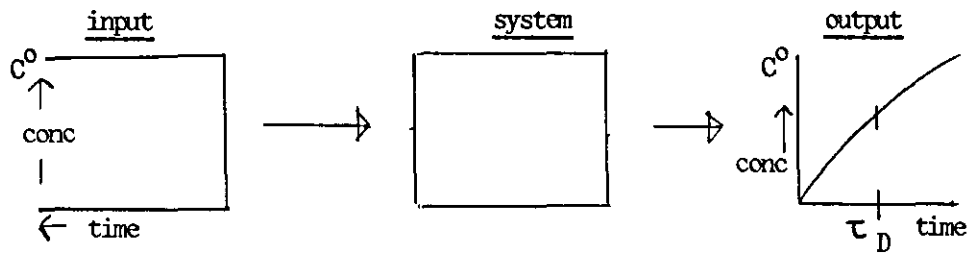

Fig. 1.12 Dynamic Response of Detector System

Output response times and variances are mathematically related. Thus a linear output of duration τ_D has a variance of $\tau_D^2/18$, whilst an exponential output of time constant τ_D has a variance of τ_D^2. If the detector response function is known the modification of any arbitrary input function can be ascertained by convolution (70).

In experimental studies, the influence of the amplifier time constant in photometric detectors has been explored from the distortion of Gaussian peaks (34,71). The high dispersion of an atomic absorption detector has been measured by comparison with that of a photometric detector using the same flow manifold (62), and in a similar way the peak broadening effects of a coulometric detector was ascertained by placing it in series with a UV detector (72). The complex dynamic response of the atomic absorption detector above was modelled by a parallel tank model possessing two time constants (73).

With ion-selective electrodes, slow diffusion phenomena cause sluggish response, particularly in the case of liquid membranes (74). Their application in flow analysis is limited and solid membrane sensors are preferred. Ion selective electrodes are best suited to continuous monitoring where slowly changing analyte concentrations are encountered (74).

The dynamic response of amperometric detectors, including dropping mercury electrodes and glassy carbon electrodes in various configurations, has been studied extensively (75-86). Usually the responses are rapid except in the cases of slow electron transfer (81) and with coated electrodes in which membrane diffusion plays a controlling part (86). In a number of studies, the cell has been assumed to function as an exponential mixing tank, so that the response time could be taken as 63 per cent of the final steady state signal value (78,79,83,84). This allows an effective detector volume to be calculated via the flow rate, which when compared with the geometric volume of the cell facilities interesting comparative studies of different detectors. Thus, using a carbon paste electrode in a wall-jet configuration, the effective volume was less than the geometric volume when an amperometric mode was used but this position was reversed in the potentiometric mode (83). Large effective detector volumes, indicative of diffusion control, were encountered with dropping mercury electrodes arranged with parallel liquid flow. But this volume was reduced by directing flow at the electrode when efficient mixing was attained. This situation also prevailed in the Metrohm EA-1096/2 wall-jet electrode with a glassy carbon sensor (79). Smaller response volumes in

solid electrode detectors compared with cells using mercury electrodes have also been reported, but in each case the effective volume exceeded the geometric value (84).

1.3.2 Amperometric Detectors

Amperometric detectors usually operate at a fixed potential in the limiting current region of the voltammogram. A variety of electrode materials and cell geometries have been employed some of which are illustrated in Fig. 1.13.

1.3.2.1 The Limiting Current

The limiting current (i_L) at each type of electrode originates from the flux to the electrode (j) via Faraday's laws of electrolysis:

$$i_L = n F A j \qquad 1.16$$

A is the electrode area, n the number of electrons transferred and F is the Faraday constant.

The flux is obtained by solving the general diffusion-convection equation 1.1 following methods developed by Levich (2). Results can be systematized by the introduction of selected dimensionless parameters (87):-

tubular electrode

length l; radius r.

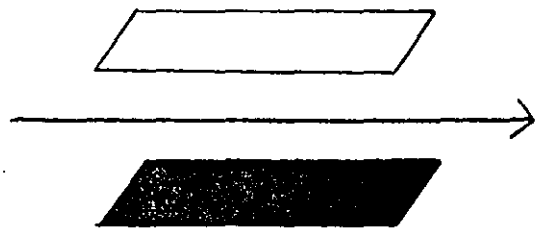

channel electrode

length l; width w; channel depth, b.
(i) deep channel, $b \rightarrow \infty$
non-parabolic flow.
(ii) thin channel, b finite, parabolic flow.

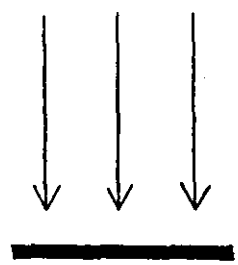

disc electrode

radius, r

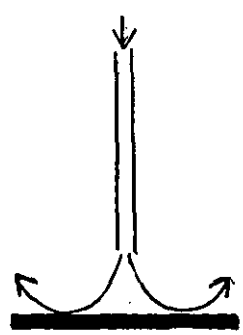

wall-jet electrode

radius, r.
jet width, a.

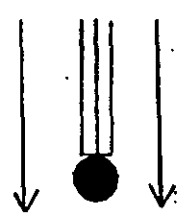

polarographic electrode

dropping mercury,
radius r_{Hg}

Fig. 1.13 Amperometric Detectors.

Flow directions are arrowed. Working Electrodes are shaded.

Table 1.1

Number	Symbol	Definition	Significance
Sherwood	Sh	$\frac{j}{DC/l}$	ratio of total mass transfer to mass transfer by diffusional flux in equivalent stationary field
Reynolds	Re	Ul/ν	ratio of inertia force to friction force
Schmidt	Sc	ν/D	ratio of momentum transfer by velocity effects to mass transfer by diffusion effects.

D is the diffusion coefficient, C the concentration, ν is the kinematic viscosity, l is a characteristic length and U is the average linear flow rate.

These numbers are dimensionally related:

$$Sh = k\,(Sc)^{\beta}\,(Re)^{\alpha} \qquad 1.17$$

k is a numerical constant and α and β are independent exponents.
For electrode configurations, β is usually 1/3.

From the definition of the Sherwood number, the general hydrodynamic voltammetry equation 1.16 can be restated:

$$i_L = n\,F\,A\,D\,\frac{C}{l}\,Sh \qquad 1.18$$

Or, in the more expanded form (87)

$$i_L = kn\ F\ w\ D\ C\ (Sc)^{1/3}\ Re^{\alpha} \qquad 1.19$$

w is a characteristic width. Particular values of the parameters are given in Table 1.2.

Table 1.2 Specific forms of general equation for limiting current.

Detector	k	w	l	α	Ref
Tubular	8	$l^{1/3}r^{2/3}$	l	1/3	88
Deep channel	0.8	w	l	1/2	89
Thin layer	1.47	$w(l/b)^{1/3}$	l	1/3	90,91
Disc	3-3.3	r	r	1/2	92,93
Wall-jet	1.15	a	r	3/4	94
Polarographic	7.9	r_{Hg}	l	1/3	95

l is the particular form of the length variable in Re.

The responses of each type of electrode are sensitive to the flow rate to an extent determined by the Reynolds number exponent (α).

The equation for the tubular electrode was derived by Blaedel et al. (88) using an expression for the flux given by Levich (2). Experiment confirmed the 1/3 dependence of limiting current on flow rate provided $Re < 100$, which is much lower than the critical value expected for turbulence in a smooth pipe and was attributed to an entry effect (88). A flow rate independent component of the current was also reported at low flow rates and attributed to diffusion at the tube ends (96), but this conclusion has been challenged on statistical grounds (97).

The limiting current expression for the deep channel electrode (89) was derived from the expression for diffusion to an infinite plate (2), and gives a flow rate exponent of 1/2, which is characteristic of flow containing a vertical component. However when the flow is confined to a narrow channel the profile is parabolic, there is no velocity component normal to the surface and the exponent becomes 1/3 (90). Weber (98) has reviewed experimental results on rectangular channel detectors and makes the observation that most practical devices are dimensionally of the thin layer type and should conform to the 1/3 power law. Apparent exceptions (99) may be due to the presence of a vertical component in the flow or to the dubious practice of measuring the current signal from a transient peak height rather than at the steady state. The entrance zone, where the hydrodynamic boundary layers associated with parabolic flow are being established, is of negligible size in typical flow cells (98).

Radial flow from the centre of a disc electrode embedded in a narrow channel produces a limiting current of dimensionally similar form to the rectangular channel case, so that this electrode too responds to flow rate by the 1/3 power law (90,91).

Theoretical equations for a disc electrode totally exposed to the flow were developed independently by Marchiano et al. (92) and Matsuda (93). The expressions obtained are identical save for the numerical factors, which reflect the different flow distributions selected by the authors. Marchinao et al. chose uniform flow and deduced a Sherwood number:

$$Sh = 0.78\ Sc^{1/3}\ Re^{1/2} \qquad 1.20$$

Matsuda developed his treatment for a disc situated at the nose of a cone placed in a laminar flow and deduced:

$$Sh = 0.68\ Sc^{1/3}\ Re^{1/2} \qquad 1.21$$

These ideal electrodes are difficult to construct, but the problem may be circumvented if the electrode is embedded in a larger disc. This arrangement of uniform accessibility is hydrodynamically similar to the previous cases with a Sherwood number given by (100):

$$Sh = 0.53\ Sc^{1/3}\ Re^{1/2} \qquad 1.22$$

With this device, the 1/2 dependence of the signal on the flow rate was demonstrated (100). The flow to the electrode can be produced from a nozzle, and theoretical behaviour is realised when the nozzle diameter exceeds that of the electrode but for larger electrodes the flow rate exponent increases suggesting a transition to wall-jet behaviour (101,102). There has been little application of this electrode to analysis, but the simplicity of design merits further attention (103).

The mechanical principles of the wall-jet were elucidated by Glauert (104). An impinging jet, reflected from a wall, mixes with a stagnant region and develops a boundary layer oblique to the surface and spreads radially over it. Yamada and Matsuda (94) realised the possibilities of the phenomenon in electrochemistry and deduced the theoretical equation given in Table 1.2 which may be stated in alternative form:

$$i_L = k\ n\ F\ C\ D^{2/3}\ \nu^{-5/12}\ a^{-1/2}\ R^{3/4}\ \phi_v^{3/4} \qquad 1.23$$

here $\mathscr{Q}_v$ is the volumetric flow rate, a is the jet diameter and R is the electrode radius. Experimental confirmation was obtained over a wide range of variables with k taking the value 1.38 provided R>0.15 cm and the nozzle was placed between 2 and 4 mm from the electrode. The restriction on radius being attributed to the finite width of the jet and so implicitly recognises a small central zone where disc type response may be relevant. The restriction imposed by the jet height was further examined by Gunasingham and Fleet (105) who attributed the failure of theory at low nozzle heights to its interference with the hydrodynamic boundary layer. The integrity of jets at fairly large separations of about 4 mm were validated and consequently large volume cells have been advocated for wall-jet response, and have been successfully employed in liquid chromatography detection (106). Elbicki et al. (90) examined confined wall-jet electrodes, recognised the small central zone of disc-like response and realised that a developing wall-jet hydrodynamic boundary layer would be restricted by the cell channel depth, thereafter parabolic flow would evolve. Conditions under which essentially wall-jet or thin-layer behaviour would prevail were delineated.

Central to the ideas of Gunasingham et al. (105) and Elbicki et al. (90) is the estimate of the hydrodynamic boundary layer thickness (δ_{bL}). Gunasingham and Fleet (105) on hydrodynamic considerations following Glauert (104) and Yamanda and Matsdua (94), calculated δ_{bL} as a function of distance (x) from the electrode centre:

$$\delta_{bL} = 5.8\,\pi^{3/4}\,a^{1/2}\,\nu^{3/4}\,x^{5/4}\,\mathscr{Q}_v^{-3/4} \qquad 1.24$$

Alternatively, this hydrodynamic dimension can be evaluated from the much smaller diffusion boundary layer thickness (δ_{dL}) using the similarity relation (2):

$$\delta_{dL} = k'(Sc)^{-1/3} \delta_{bL} \qquad 1.25$$

where k' is a numerical constant.

δ_{dL} is defined by the general Nernst diffusion equation:

$$i_L = n F A D \frac{C}{\delta_{dL}} \qquad 1.26$$

Equating this expression to the Matsuda equation for the wall-jet produces:

$$\delta_{dL} = 0.725 \; a^{1/2} \nu^{5/12} D^{1/3} x^{5/4} \phi_v^{-3/4} \qquad 1.27$$

Using equations 1.24 and 1.27 in equation 1.25, gives $k' = 0.17$.

Elbicki et al. (90) quote an alternative estimate for δ_{bL}:

$$\delta_{bL} = 6.11 \; a^{1/2} \nu^{3/4} x^{5/4} \phi_v^{-3/4} \qquad 1.28$$

which implies $k' = 0.37$. These k' values may be compared with 0.6 for a flat plate and 0.5 for a rotating disc (2).

1.3.2.2 Flow Analysis Applications

Direct application of the aforementioned relations for the limiting current are only strictly applicable at the steady state when the flowing solution is homogeneous. In flow injection and liquid chromatography detection, the sample plug suffers dispersion or chromatographic peak broadening, both effects being flow sensitive. These intrinsic phenomena interact with the flow dependency of the

signal so that the peak current, which is the usual analytical parameter measured, bears a complex resultant relation to flow rate. Thus under flow injection conditions with laminar flow through a tubular electrode, the peak current variation with flow rate evolved from the theoretical 1/3 power law at low dispersion to a -1/6 dependency at high dispersion (107). Similarly, with a thin layer cell in a liquid chromatography experiment, the flow rate exponent increased continuously from 5/6 to -1/6 as the flow increased, passing through an optimum value when the signal was independent of flow rate (108).

Amperometry is a prominent method of detection in liquid chromatography and has been thoroughly reviewed (109). The technique is also popular in other methods of flow analysis, particularly in conjunction with flow injection. In this situation, solid electrodes are more rugged than mercury ones and possess the advantage of a wider anodic range obviating the necessity of deoxygenating the flowing stream when used in the oxidative mode. Glassy carbon is particularly suitable because of its low background noise level (110). Further, recent advances in electrocatalysis using chemically modified electrodes and in permselectivity using polymer coated electrodes have been incorporated into flow detectors to improve selectivity and stability (111). The latter application should prove useful in process stream monitoring where electrode fouling is often a problem. High selectivity is also afforded by enzymes attached either mechanically (112) or covalently (113) to platinum wire electrodes.

The wall-jet configuration has been favoured by many workers and the commercial Metrohm EA-1096 cell has often been used. Fogg and co-workers have used a similar impinging jet design to exploit a variety of chemistries at the glassy carbon electrode. Thus nitrate was determined, after cadmium reduction, as nitrosyl bromide (114); and also as the nitro-derivative of thiophene-2-carboxylic acid following nitration (115). Bromine is reduced at positive potentials and because of its chemical reactivity permits a range of indirect analyses (116,117). Iodine has been used in a similar way (118,119). Phosphate has been determined as phosphomolybdate by reverse-FIA (120), whilst nitroprusside, sulphite and EDTA have been determined by direct anodic oxidation (121).

Wire electrodes, because of their simple construction, are also frequently employed in flow analysis. A platinum wire electrode in the reductive mode has been used in the important analysis of dissolved oxygen (122), and an attempt to elucidate the response of such a wire placed annuarly in a tube has been attempted (123). The use of twin wires operated biamperometrically is an attractive extension of this usage since the deployment of reference and counter electrodes is then avoided; the displacement of working and reference electrodes in particular can introduce large iR drops in narrow cells. The biamperometric method was used in the indirect estimation of reducing sugars from the Fe(II) produced on reaction with hexacyanoferrate (III) (124); and from H_2O_2 produced enzymatically (31). The main drawback of this configuration is the theoretical limitation of a non-linear calibration (125).

Tubular and rectangular channel cells are less favoured in flow injection analysis, although the latter are common in liquid chromatography (74).

Comparative studies of electrochemical detectors are not frequently encountered in the literature. With this regard, a figure of merit has been proposed incorporating the signal-to-noise ratio and cell dispersion as an index of performance (126).

1.4 Flow Titrations

Flow titrations may be defined as those methods using differential flow rates or concentration gradients to perform a titration.

1.4.1 Variable flow rate methods

To a sample stream flowing at a steady rate, and containing analyte at a fixed but unknown concentration, is added titrant at an adjustable rate. If the streams are thoroughly mixed, the end-point is located when the rate of titrant addition is stoichiometrically equivalent to the rate of analyte flow and a predetermined signal is registered by a suitable detector system. In the earliest application of this principle, the titrant was produced coulometrically in the sample stream using a variable generating current (127). Any out-of-balance signal in the detector may be used, by feedback, to adjust the generator current and return the system to its steady state. In particular, the method has been used in the continuous monitoring of gas streams with absorption. Thus SO_2 in air has been determined by iodine titration and organic sulphur compounds by bromine titration (127).

Alternatively, the titrant may be added volumetrically as a merging stream, the titration variable being the titrant flow rate (128). When titrating Fe(II) by Ce(IV), a turbular platinum electrode was used as a potential indicating electrode, the off-set value of which was used to adjust the peristaltic pump used for titrant delivery via a servo-mechanism. Equipment of this type is readily incorporated into the control loop of an on-line analyser (129).

Complete titration curves can be obtained by the flow merging technique by variation of the ratio of analyte to titrant through the equivalence point by a programmed differential flow rate schedule. The method was demonstrated for a sample flow rate increasing linearly with time with constant titrant delivery. A number of acid-base and redox titrations were performed successfully using photometric and potentiometric detection (130). By simultaneously varying analyte and titrant flow rates in a reproducible cyclic programme, chloride was determined in waters with potentiometric and conductimetric detection (131). These methods are particularly suitable for the analysis of discrete samples using the flow characteristics of the system to introduce automation.

1.4.2 Linear concentration gradient methods

When a reagent is washed from a continuously stirred tank reactor operating at a discharge rate of twice the inlet rate, concentration gradients decreasing linearly with time are produced at the outlet. Conversely when a inlet stream is diluted in the tank similarly operated an increasing linear gradient is produced (132).

On merging and mixing these gradient streams with a constant flowing sample stream a titration is performed with an end-point occurring at time, t_e:

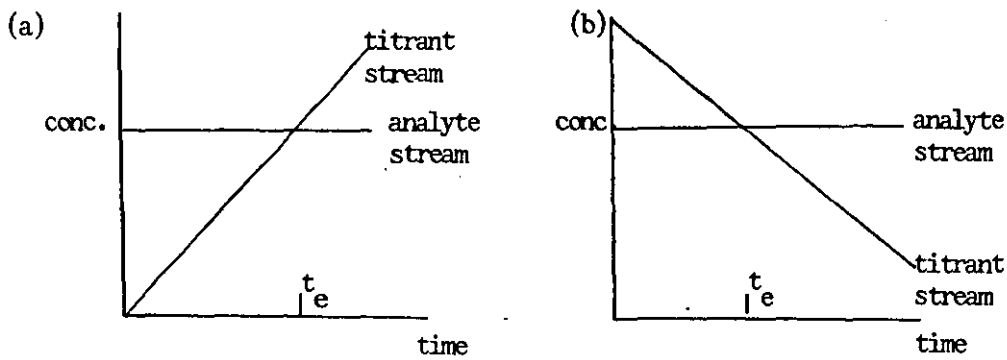

Fig. 1.14 Merging streams titration with linear concentration gradient of titrant
(a) Increasing gradient
(b) Decreasing gradient

The first application of this method employed a segmented stream manifold to achieve thorough mixing of the merged streams (133). Sodium hydroxide was titrated with hydrochloric acid with photometric detection using thymol blue as indicator, which is coloured in excess sample. When using an increasing titrant concentration gradient, it was advantageous to place the indicator in the titrant stream as the start of the titration was then signalled by the rise in absorption due to excess sample and the end-point by the disappearance of colour due to excess reagent. Titration times between 20 and 120s were obtained. Phosphoric acid was titrated with sodium hydroxide using a pH electrode detection system. A full titration curve was obtained and a titration rate of 10 samples hr^{-1} was achieved. A similar manifold was used to titrate sulphide with mercury (II) nitrate potentiometrically (134). Titration times of 28-179s were reported and ten replicate titrations of a 4×10^{-4} M solution of sulphide gave a coefficient of variation of 1.16%.

A linear concentration gradient of titrant can also be introduced into a flowing sample coulometrically (135). By using a saw-tooth generating current, a triangular titrant concentration profile is produced and forward and back titrations can be performed on the analyte in succession:

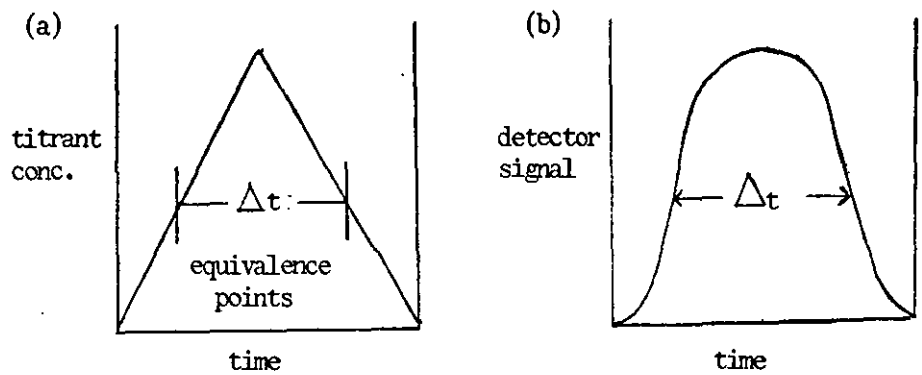

Fig. 1.15 Triangular Programme Titration
(a) Titrant concentration profile
(b) Detector response

The peak width at the equivalence points decreased linearly with analyte concentration. This regime removes the uncertainty in the location of the start of the titration and has been used with electro-generated Ag(I) (47,135), bromine (136,137) and iodine (138) as titrants.

As well as these continuous titrations, linear gradients can be used to titrate discrete amounts of sample. If the contents of the variable volume tank reactor described earlier in this section are well mixed, the temporal concentration gradients described exist internally. Thus if titrant at concentration C_T^o is fed into a tank containing analyte at an initial concentration C_A^o, the concentration of the former increases whereas that of the latter decreases, so that titration is possible (139):

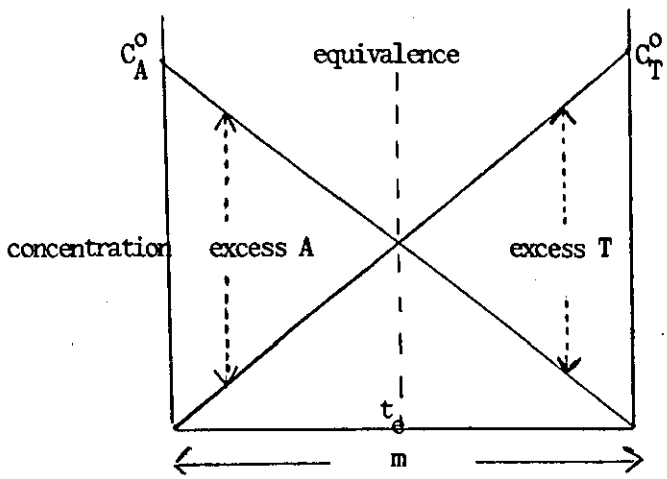

Fig. 1.16 Linear concentration gradients within variable volume tank reactor. Tank originally contains analyte at C_A^o and is fed with titrant at C_T^o. Outlet flow is twice inlet flow. t_e is the equivalence time, and m is the emptying time of the tank.

By similar triangles:

$$C_A^o = \frac{C_T^o \, t_e}{m - t_e} \qquad 1.29$$

Using this technique chloride was titrated by Ag(I) using an ion-selective sensor located externally to the reactor in the outlet stream. Titration times from 1-3 mins. were obtained, but observed end-points differed from theoretical values:

observed end-point = 1.3 (calculated end-point)-0.159

This discrepancy was attributed to small variations in the flow rate and to the contribution from the dead volume between tank and detector. Nevertheless, repeatable results were obtained on replicates and a serum sample was successfully analysed using an empirical calibration curve.

1.4.3 Flow injection titrations

If a sample plug containing analyte is injected into a flowing titrant stream using a mixing tank as in the manifold shown in Fig. 1.4, then the width of the transient shown in Fig. 1.4c, viz Δt, corresponds to a distance between equivalence points and thus denotes a titration time in a similar manner to the triangular titration previously discussed. In this flow injection case, the titration time, given by equation 1.4, responds to the logarithm of the analyte concentration and is thus analytically significant. The value of the constant term has been derived rigorously without assumptions, and is given by (64):

$$\text{constant} = \tau \ln C_T^{\circ} (D_s - 1) \qquad 1.30$$

where C_T° is the concentration of titrant in the flowing stream and D_s is the dispersion coefficient of the analyte. However, this term is of academic interest as most applications of the method rely on empirical calibration.

In the first application of the technique using mixing chamber manifolds, hydrochloric acid was titrated by sodium hydroxide using bromothymol blue as indicator with a photometric detector tuned to the relevant colour change and calcium (II) was titrated by EDTA with potentiometric detection. Between 20 and 60 samples per hour were titrated (39). Subsequently the versatility of the method was demonstrated by titrations based on conductimetric, fluorescence and flame photometry detection (140), and by titrations involving acid-base, redox, complexometric and catalytic chemistries (141). In a variation, the alkanity of neutral waters was established by injecting titrant into the flowing sample stream (142).

The natural dispersion in an open tube was shown to be sufficient to perform a number of indicator titrations photometrically. The low hold-up volume achieved by dispensing with the mixing chamber allowed throughputs of up to 240 titrations hr^{-1} to be attained (143). Impressed by this statistic, the Ruzicka school has persisted with gradient tubes and applications using amperometric (17), and optosensing detectors based on immobilised indicators (144) have been reported.

Most applications use detection systems based on the properties of the analyte. However, if a large sample is injected and the product is monitored, then analyte is in excess at the centre of the plug and product concentration shows maxima at the equivalence points occurring in the leading and trailing edges of the plug. A doublet transient is recorded and the distance between peaks directly gives the titration time, Δt. By injecting 480 µl of a Cu(II) sample into a EDTA titrant and dispersing in a 400 µl coiled tube, the complex formed was monitored in this way (145).

Flow injection titrations have attracted interest because of the simple apparatus involved, ease of automation, high throughput and the self restoring nature of the system in that the titrant stream washes out the manifold between injections.

Although this flow injection technique has many similarities with a classic titration, the use of the term 'titration' in this context has been criticised by Pardue et al. (37), because viewed as a whole, the analyte is incompletely reacted with titrant. These authors prefer to categorise the method as a kinetic one since it is based on the measured time interval

between pre-selected reference values. However, this objection has not been sustained by popular practice, although the compromise term 'pseudo-titration' has been mooted (140).

SECTION TWO

CHARACTERISATION OF A FLOW AMPEROMETRIC DETECTION SYSTEM - EXPERIMENTAL

2.1 Electrochemical Cell

2.1.1 Working electrode detector

Details of the construction of the working electrode detector are given in Fig. 2.1 (146). This was made of PTFE in two detachable parts, a part holding the electrode and a part allowing entry of a stream of solution. These parts define a small chamber from which the flowing inlet solution can escape radially. The electrode holder was designed to accommodate centrally a Metrohm glassy carbon electrode (EA 286) of diameter measured as 2.88 mm set in a cylindrical PTFE rod of 7 mm o.d. The inlet block was drilled as follows. The first 1 cm depth was drill threaded and flat-bottomed for convenient butting of a flanged tube. The next 1 cm depth was drilled straight with a diameter of 1 mm and the remaining small depth, approximately 1 mm, was drilled straight with a diameter of 0.35 mm. The depth and width of the X-channel, which allows separation of the two parts, and permits escape of the flowing solution, were 0.25 and 2.5 mm respectively. The dimensions allowed snug fit with mutual clamping of the entry port onto the electrode holder.

2.2.1 Cell Assembly

The working electrode detector was mounted either vertically or horizontally along with reference and auxiliary electrodes in beakers usually containing supporting electrolyte as in Fig. 2.2. An electroysis beaker (Metrohm) was used with the vertical electrode; and a plastic beaker, with suitably drilled holes, sealed with a reusable adhesive (Blue-tack, Bostic) was used with the horizontal electrode.

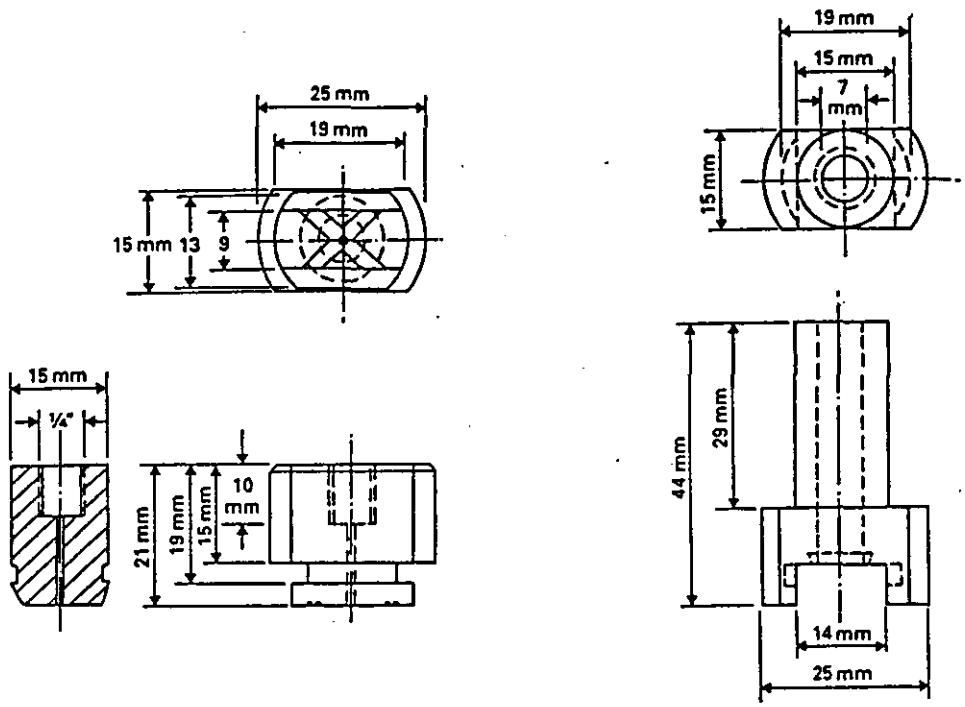

Fig. 2.1 Details of Construction of Working Electrode Detector.
(a) Entry part. (b) Part holding electrode. (146)

The auxiliary electrode was a platinum spiral of large surface area. A saturated calomel electrode (Metrohm, 6.0702.100) and a silver/silver chloride electrode were used as the reference on different occasions. The latter electrode was prepared from a clean silver billet (Radiometer, P.4011) by anodising in 1 M HCl for one hour at 4-6 mA. The blue-black chloride surface produced was stable indefinitely when the electrode is stored in 1 M KCl. The potential difference of the two electrodes measured in saturated KCl was 37 mV, close to the theoretical difference of 45 mV.

A significant iR drop in the cell was not anticipated as the resistance between working and auxiliary electrode, measured by a WPA CM25 Conductivity Meter, was only 156 Ω.

2.1.3 Solutions

The performance of the working electrode detector was investigated using hexacyanoferrate (II) as the electroactive probe whose transport properties and electrochemical response at glassy carbon are well documented. The species undergoes single electron oxidation:

$$Fe(CN)_6^{4-} = Fe(CN)_6^{3-} + e$$

Solutions containing up to 1 mM $Fe(CN)_6^{4-}$ in supporting electroyle were prepared fresh daily by weighing A.R. $K_4\ Fe(CN)_6.3H_2O$.

Supporting electroyle was either 1 M KCl or a phosphate buffer containing 0.08 M NaH_2PO_4, 0.08 M Na_2HPO_4 and 0.48 M $NaNO_3$ adjusted to pH 7 by dropwise

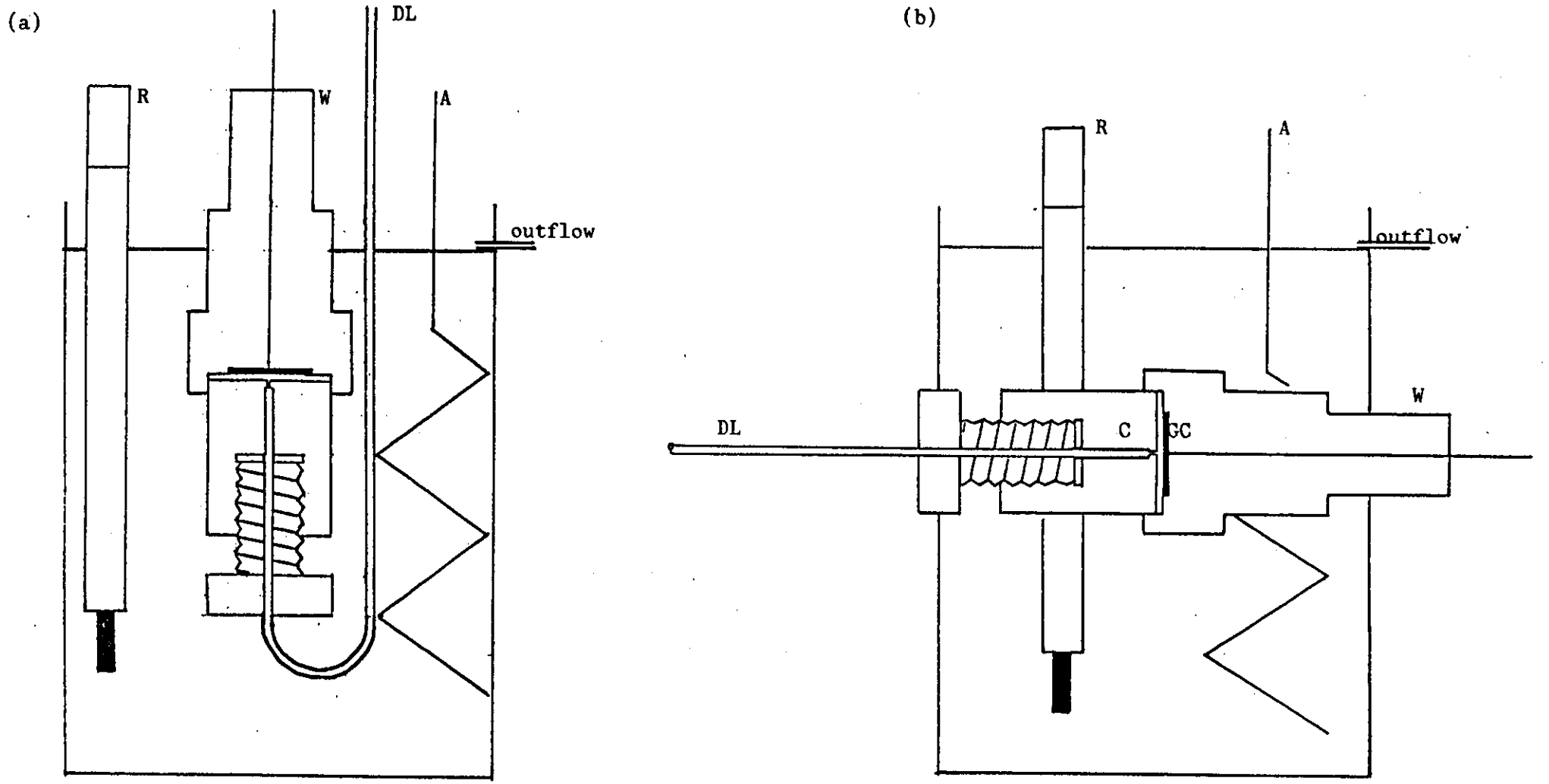

Fig. 2.2 Cell Assembly, with working electrode detector (W) mounted (a) vertically, and (b) horizontally. R is the reference electrode, A is the auxiliary electrode. DL is the delivery line. The detector is in two sections, a part contaning the inlet channel and jet (C) and a part housing the glassy carbon electrode (GC). The electrode chamber is the space between these sections.

addition of 40 per cent w/v NaOH. The ionic strength of the buffer was at least 0.8, to ensure adequate conducting capacity.

All measurements were made at ambient room temperature of 20-23°C.

2.2 Instrumentation

The instrumentation used and their inter-relationships are shown in Fig. 2.3

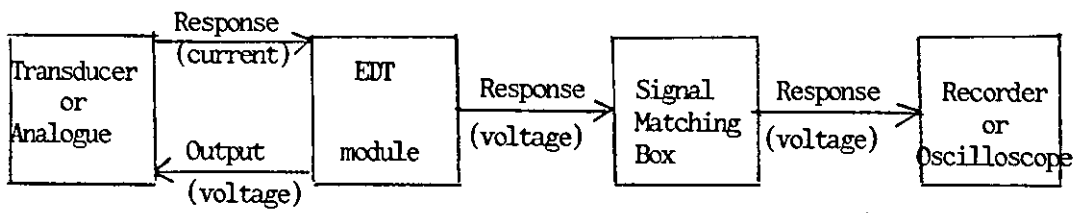

Fig. 2.3 Schematic diagram of instrumentation
Signals originated either from an experimental transducer or its electronic analogue.

The EDT model ECP 1000 polarograph unit (EDT Analytical) was the voltage source and response current processor. Constant voltage and linear voltage sweep output modes were used. The instrument had an optional filtering time constant facility calibrated as 1.2s. The output from this module was 1 V full scale and for interfacing purposes this could be attenuated without loss of sensitivity via a laboratory built operational amplifier signal impedance matching box.

Signals were recorded either by a potentiometric pen recorder or, in the case of fast transients, by oscilloscope. The pen recorder was a Howe YT 1000 model, with variable chart speed, an internal event marker and a socket for connection to an external event marking circuit.

The recorder response was 100 mV fsd and was used with the signal matching box set at 10:1. Also used were the Telequipment DM 64 storage oscilloscope, set at 20 mV/division with signal matching box at 10:1; and the Telequipment S51B oscilloscope set at 0.1 v cm^{-1} with signal matching box at 1:1. Permanent records of the oscilloscope traces were captured on Polaroid 667 black and white film using a hooded Polaroid CR-9 camera on open exposure. The films were enlarged x 1.5 on a photocopier for measurement.

2.3 Working Electrode Pretreatment

Glassy carbon is an arrangement of tangled aromatic ribbons with varying degrees of cross-linking. The state of the surface has not been completely defined but oxygen functional groups such as quinones are probably present. These groups might serve as mediators of electrons between the electrode and electroactive species (147,148).

The redox state of the surface can be modified by many diverse treatments such as mechanical polishing, chemical oxidation, electrochemical preconditioning, radio-frequency plasma and laser irradiation (149). Procedures based on these processes have been suggested to produce a well activated electrode, which is one having minimal over-potential and maximum current response for the electrode process in question. Electrochemical methods are particularly convenient since no extra equipment is involved.

Engstrom (147) has made a systematic study of electrochemical pretreatments involving the sequence, magnitude and duration of applied voltages. A number of electrode reactions were studied and different conditions were prescribed. For the electro-oxidation of hexacyano-ferrate (II), electrode activation was achieved by anodising at +1.5 V for 5 minutes followed by cathodisation at -0.5 V

for 10s. Voltages and durations greater than these limits being equally effective. These conditions were rationalised by the assumption that anodisation causes the formation of an oxide multilayer which inhibits hexacyanoferrate (II) oxidation. Subsequent cathodisation reduces this oxide layer and activates the electrode towards hexacyanoferrate (II). The treatments are equally effective in both the presence and absence of electroactive species, but are influenced by the supporting electrolyte composition; thus at pH7 the half-wave potential of the hexacyanoferrate (II) oxidation at a rotating GC electrode were less anodic in citrate buffer than in phosphate buffer (148).

In view of this research, a pretreatment procedure of applying an anodising voltage of +1.5 V or greater for 5 minutes followed by a cathodising voltage of at least -0.5 V for 1 minute was adopted. In voltammetry, successful activation was indicated by low thermodynamic potentials. Deterioration of the surface was diagnosed by drawn out voltammograms presumably attributable to build up of inactive oxide multilayers after repeated scans to high positive potentials. Restoration was achieved by electrochemical retreatment.

Electrodes of unknown history were repolished for 4-5 minutes with an aqueous alumina slurry applied with a soft cloth. After washing with distilled water in an ultrasonic bath the electrodes were electrochemically activated.

2.4 Stopped Flow Voltammetry

Working electrode, S.C.E. reference and auxiliary electrode were mounted vertically in the electrolysis beaker. When required, solution was delivered to the working electrode detector by means of an Ismatic MS-4 Reglo/8 peristaltic pump. The instrumentation was as in Fig. 2.3, with the pen recorder in position.

Linear voltage sweep voltammograms were recorded on static solutions of 0.74 mM hexacyanoferrate (II) ion in phosphate buffer producing peaked currents due to competing influences of increased electron transfer and increasing diffusion layer thickness with time. One set of results were recorded with the working electrode freely placed in a large volume of solution. A second set was recorded with the solution confined to the cavity of the fully assembled flow-through detector. These conditions were achieved by the following procedure:

(i) Buffer solution in cell. Record background currents at the series of scan rates chosen.

(ii) Pump electroactive solution into the cavity of the fully assembled working electrode detector for a short period. Disperse the small amount of this solution exuding from the cell exit into the surrounding buffer solution. Thus the electroactive solution was trapped in the cavity of the detector cell and in contact with a buffer reservoir of infinite volume. Record scan. Duplicate to confirm repeatability.

(iii) Remove inlet port of working electrode detector. Suspend electrode freely in electroactive solution filling the beaker. Record scan. Duplicate to confirm repeatability.

(iv) Repeat steps (ii) and (iii) for the series of voltage scan rates, interchanging the sequence randomly.

The electrode was activated at +1.5 V for 5 minutes and at -0.5 V for 1 minute followed by three conditioning runs to ensure uniformity of response before step (i) and before the sequence (ii)/(iii).

2.5 Hydrodynamic Voltammetry

Fully assembled working electrode detector, Ag/AgCl reference and auxiliary electrode were mounted in the electrolysis beaker containing 1 M KCl supporting electrolyte as in Fig. 2.2a. The instrumentation was as in Fig. 2.3, with the pen recorder in position.

Linear voltage sweep voltammograms were recorded on a flowing solution of hexacyanoferrate (II) ion in 1 M KCl. The flowing solution maintains a constant diffusion layer thickness and so the current increases through the half-wave potential to a limiting value.

2.5.1 Peristaltic pump manifold

At low flow rates below 2 ml min^{-1}, flow was maintained by an Ismatec MS-4 Reglo/8 peristaltic pump. Smooth voltammograms were obtained by inserting a small glass bulb of volume ca 25 ml on the discharge side of the pump (150). During operation the bulb remains partly filled with air, the elastic properties of which removes energy from the flow eliminating the pulse amplitude.

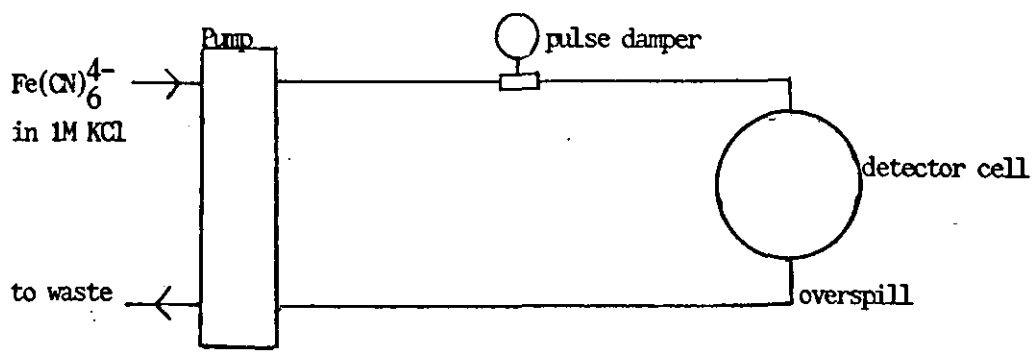

Fig. 2.4 Flow manifold with peristaltic pumping for Hydrodynamic voltammetry

Flow rates were determined gravimetrically following the electrochemical experiments. Using distilled water, the discharge of the pump over a timed period was weighed directly into a tared beaker on a Mettler 1600 top loading balance with a precision of ± 0.01g. The variation in flow rate using peristaltic pumping over a period commensurate with the total voltammoagram scan time was estimated by recording the flow rate at 30s continuously successive periods over a total of 5 minutes. The average relative standard deviation for four flow rates between 1 and 5 ml min^{-1} was 1.75 per cent. In hydrodynamic voltammetry, the limiting current (i_L) is related to the volumetric flow rate (V_f) by the relationship:

$$i_L = \text{constant } V_f^{\alpha} \qquad 2.1$$

Where the exponent α, is a numerical factor (Section 1.3.2). Thus the uncertainty in the limiting current due to flow rate variation is (151):

$$\frac{\Delta i_L}{i_L} = \alpha \frac{\Delta V_f}{V_f} \qquad 2.2$$

Since α is always <1, the residual fluctuation in limiting current using damped peristaltic pumping will be small and would probably not exceed 1.3 per cent.

2.5.2 Hydrostatic Head Manifold

At high flow rates, smoother voltammograms were obtained by hydrostatic head delivery than by peristaltic pumping. In this case, a reservoir of electroactive solution was placed above the cell and connected to the working electrode detector inlet by pieces of narrow PTFE tubing joined by short

connections of soft PVC tubing. The flow rate range available was fixed by the bore of the tubing used and adjustment made by altering the hydrostatic head. The system was calibrated by plotting the volumetric flow rate (V_f ml min^{-1}) vs. hydrostatic head (h). The latter was maintained at a consistent level during a measurement by recirculating the overspill from the cell back to the reservoir by peristaltic pumping.

The curvilinear graph produced (Fig. 2.5) can be rationalised by a mechanical analysis (152). Laminar flow in straight segments of length L/m and diameter d/m, in which V_f is directly proportional to h, are described by the Poiseuille-Hagen equation:

$$h/m = \frac{128 \times 10^{-6}}{60 \pi d^4} \frac{\eta L V_f}{\rho g} \qquad 2.3$$

In addition, there will be pressure losses incurred due to changes in kinetic energy when the cross-section area changes at the connection joints. These are dependent on $V_f^2/2g$. Thus for an area change from A_1/m^2 to A_2/m^2, there is a contribution:

$$h/m = \frac{1}{(C_d^2 - 1)} \frac{V_f^2 \times 10^{-12}}{2g \times 60^2} \cdot \left(\frac{1}{A_2^2} - \frac{1}{A_1^2} \right) \qquad 2.4$$

C_d is an empirical term, the coefficient of discharge. Similarly, the energy loss when the solution flows from the detector nozzle of diameter 0.035 cm at V_f into a reservoir at zero flow contributes a term computed to be:

$$h/m = 1.54 \times 10^{-3} \; V_f^2 \qquad 2.5$$

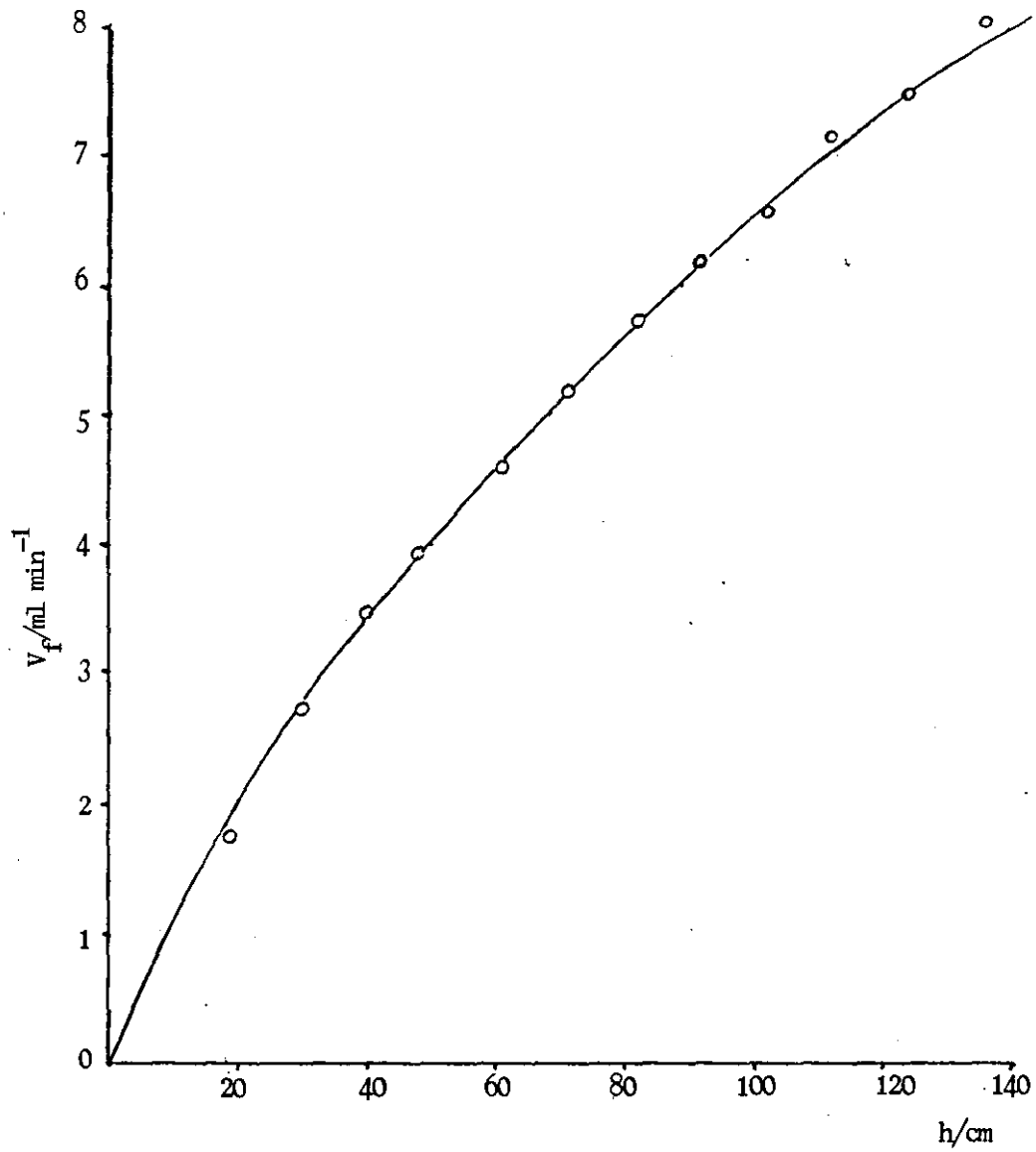

Fig. 2.5 Calibration Curve, Volumetric Flow Rate (V_f/ml min^{-1}) vs. Hydrostatic tread (h/cm).
O represent measured points.
Full curve given by equation 2.6.

This is a significant contribution and demands that the calibration be carried out with the inlet section of the working electrode detector in position.

Taking the standard gravitational acceleration (g) as 9.81 ms^{-2}, and coefficient of viscosity (η) and density (ℓ) to be 1.14 x 10^{-3} kg m^{-1} s^{-1} and 1000 kg m^{-3} respectively, which are the values for water at 25°C, the relations above were evaluated for the flow manifold used. Adjusting the coefficient of discharge to 0.44, equations 2.3, 2.4 and 2.5 additively combine to give:

$$h/cm = 7.37\ (V_f/ml\ min^{-1}) + 1.23\ (V_f/ml\ min^{-1})^2 \quad 2.6$$

This semi-empirical equation describes the calibration curve and confirms that the flow manifold is hydrodynamically well behaved.

2.5.3 Voltammetry

After activating the electrode, hydrodynamic voltammograms were recorded on flowing solutions using a linear voltage scan from the polarograph unit. A study was made of the effect of a range of flow rates from 0.41 - 7.10 ml min^{-1} on the limiting currents produced by 0.75 mM hexaxyanoferrate (II) in 1 M KCl. In addition the variation in limiting current for hexacyanoferrate (II) concentrations up to 1.0 mM was studied at constant flow rates. The limiting currents measured were corrected for the residual current contribution which was demonstrated to be independent of flow rate.

2.5.4 Computation

To assist in the interpretation of results a hydrodynamic model of the detector cell was developed. Calculations on this model were performed on an IBM PC machine using the Supercalc 3 spreadsheet as software.

2.6 Instrumentation Response

The electronic response of the signal processing equipment was tested by a sine wave of known characteristic and by a novel flow injection analogue based on a RC (resistance-capacitor) electrical circuit.

2.6.1 Flow injection analogue

The F- and W- curves that form the basis of solution mixing models discussed in Section 1.2 are examples of first-order linear response functions, which have their counterparts in other physical systems. In particular, RC electrical circuits can replicate such behaviour and have been useful in the study of transport in a physiological context (153). A diagram of such a circuit which can generate a full F-curve or the partial F/W curve which can serve as a flow injection (FI) model (60) is shown in Fig. 2.6.

The voltage developed at the output mimics the concentration from a CSTR. The RC circuit uses a decade resistance box and five calibrated 1-μF capacitors to provide RC charge time constants (equivalent to tank residence times) adjustable from 10 ms to 5s. A 0.21 function of the input reference voltage is taken to a multiplier, in the form of a summing amplifier, which provides for equal steps from 0.21 to 0.84 and simulates the dispersion (D_s)

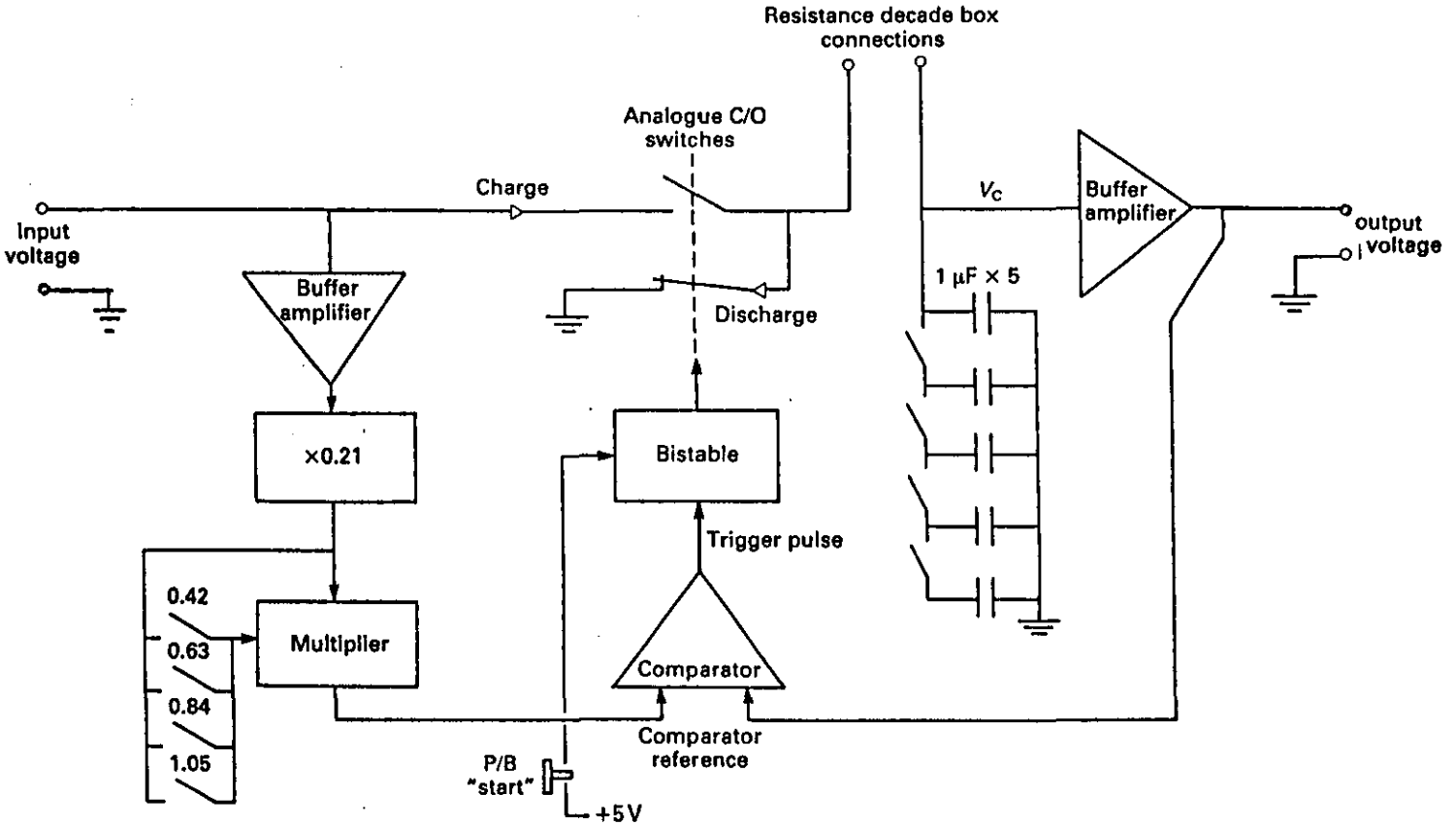

Fig. 2.6 Diagram of analogue circuit for the single-tank concentration step and the FI-pulse simulator.

of the FI model in a reciprocal manner. Thus five dispersion values can be simulated. At the end of the charge cycle when the capacitor voltage (V_c) equals the comparator reference voltage, the comparator switches, thus triggering the bistable. The bistable controls the two ganged CMOS analogue switches, switching from charge to the discharge cycle. The resistance and leakage effect of these switches is assumed to be negligible. The push-button resets the bistable and switches to charge and the start of another sweep. In addition to these fractional input voltages, there is a 1.05 option, which when operation, ensures that the bistable cannot trigger; a full F curve with a plateau at the input reference value is thus produced. High input impedance operational amplifiers minimise errors due to shunt currents by buffering the input reference voltage to the control circuit and ensuring the accuracy of the output.

The analogue circuit can be used with any suitable voltage source and recording system. In this work it was used in conjunction with instrumentation shown in Fig. 2.3 by replacing the electrochemical cell as a signal source by using the voltage output and signal processing facilities of the EDT polarograph module. To do this, additional interfacing was required as shown in Fig. 2.7. "Auxiliary" and "reference" connections on the polarograph were isolated by a 1 MΩ resistor functioning as a solution resistance, and connected to the analogue input. 1 volt was taken from the polarograph module. It was also necessary to convert the simulated voltage output into a current form using a voltage follower and a series 1 MΩ current-limiting resistor between the RC circuit output and the "test" connection of the polarograph.

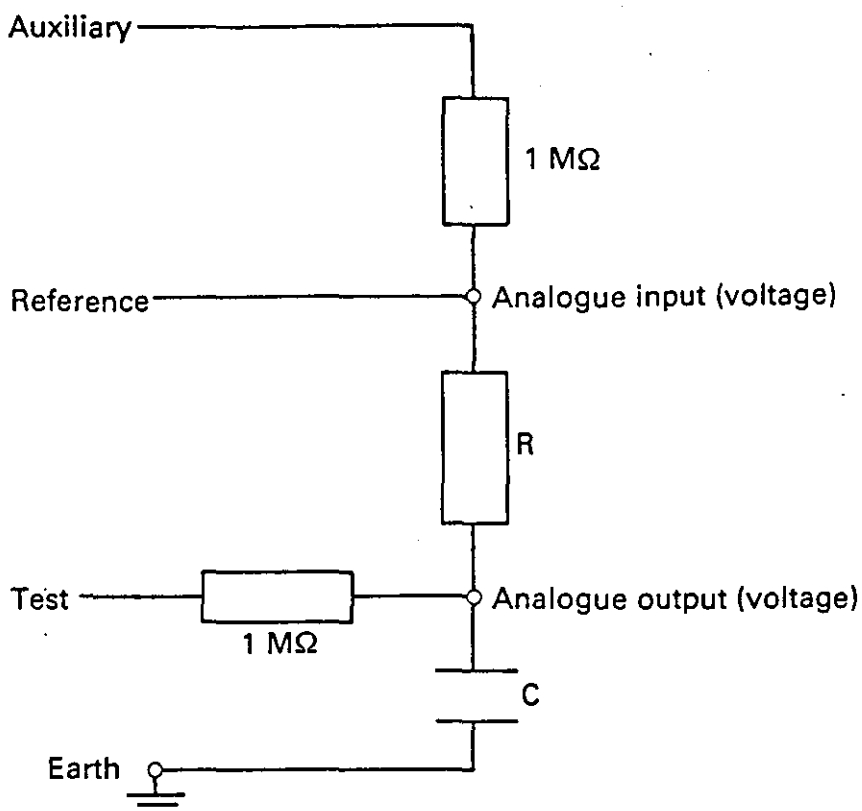

Fig.2.7 Schematic diagram of the interface between flow analogue and EDT Model ECP100 polarograph. "Auxiliary," "reference" and "test" (or "working"), typically electrode connections from the polarograph to an electrochemical cell; R, resistance and C, capacitance components of the flow analogue circuit. C is connected to earth via the polarograph and "test" held to ground by the "virtual earth" of the current/voltage converter within the polarograph

The analogue circuit and interfacing resistors were wired together in a permanent package which allowed connections to the polarograph and standard resistance box and possessed switches for the selection of capacitance and dispersion values.

Experiments were first conducted to establish the validity of the analogue as a FI model and the device was subsequently used to test the faithfulness of response of the potentiometric recorder and to calibrate the time base of the Telequipment S51B oscilloscope.

2.6.2 Sine wave testing

An independent assessment of the Howe YT-1000 recorder was made by a method based on the amplitude modulation of standard sine waves. This allows direct measure of the recorder response time, i.e. the time for full scale deflection (154).

A generator (Feedback Ltd) produced sine waves at 1 volt peak-to-peak over a range of frequencies. After passing through the signal matching box, the waves were registered by the pen recorder and the amplitude measured. The faster the response time, the higher is the threshold frequency at which the recorder starts to faithfully represent the input and record the maximum and theoretical amplitude. A frequency ($\int_t$) corresponding to a amplitude relative to the maximum of 0.85 was identified experimentally, and the response time was calculated from the theoretical relation:

$$\text{response time} \sim 0.59/\int_t \qquad 2.7$$

Alternatively the response time can be estimated from the slope of the rise curve to a step input, but unlike the amplitude method this technique is dependent on chart speed.

2.7 Dynamic Response of Working Electrode Detector

In the classical form of this experiment the response of the detector to a step concentration input of electroactive species is monitored. The experiment was conducted in the manner described below.

2.7.1 Flow manifold

The flow manifold is shown schematically in Fig. 2.8. Two solutions were employed, viz. 1 M potassium chloride and 0.75 mM hexacyanoferrate (II) in 1 M potassium chloride. The supporting electrolyte is delivered by hydrostatic head to the amperometric detector (D) at ca. 1 ml min^{-1}; whilst the electroactive solution is delivered at a controlled rate by a peristaltic pump (Ismatec Reglo 100). In the pump line, a glass bulb serves as a pulse damper, the T piece in series prevents a pressure build up in the bulb when the line is closed with the pump operating. The unused flow portion is recycled to conserve material. The net flow rate is measured at F, and is steady and reproducible. The solutions can be switched instantaneously by means of a 0.8 mm i.d. flow passage slider valve of negligible dead volume (Rheodyne 5301). This valve is connected to the detector cell by a straight stainless steel tube of length 9.4 cm and i.d. 0.8 mm. This delivery tube is attached to the slider valve and electrode channel by means of conventional screw thread connectors with flush Omnifit gripper end-fittings.

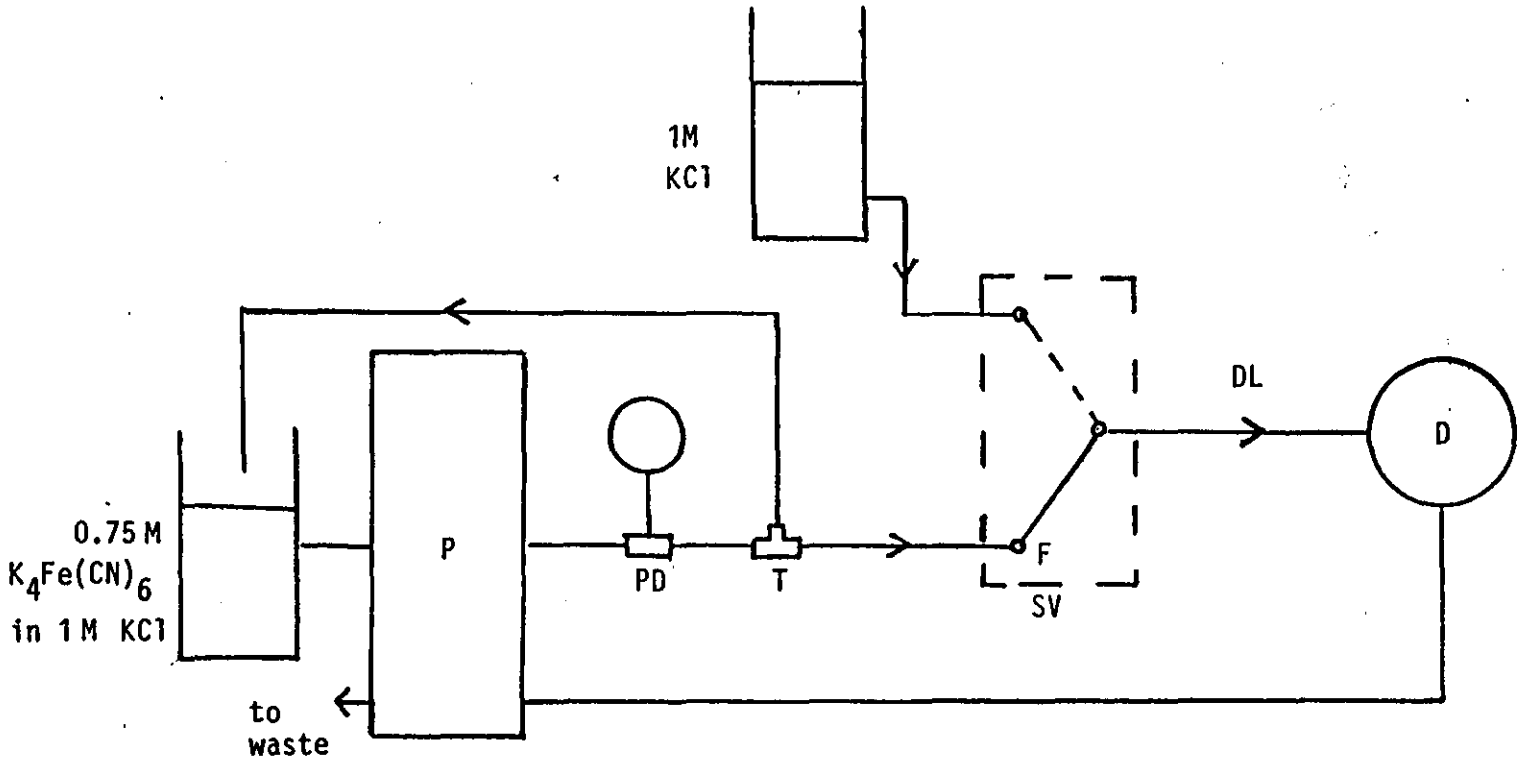

Fig. 2.8 Flow manifold for Dynamic Response Experiment.
Peristaltic pump (P). Pulse damper (PD). Tee-piece (T). Slider-value (SV).
Detector (D). Flow rate measured at F, when disconnected.
Stainless steel delivery tube (DL).

The working electrode detector was mounted in the cell horizontally as shown in Fig. 2.2b. The input electroactive concentration step formed at F thus had a straight, unimpeded path to the surface of the electrode. It should be noted that the connection of the delivery tube to the detector is an integral part of the latter, and any contribution it makes to the overall dispersion is real and not an artefact.

The electrochemical cell also contained auxiliary and Ag/AgCl reference electrodes, and was filled with supporting electrolyte. The cell overflow was sent to waste via the peristaltic pump.

2.7.2 Method

The instrumentation was as in Fig. 2.3. The working potential of 0.75 V vs. Ag/AgCl and current output (20μA fsd at 1 volt) were from the polarograph module interfaced via the signal matching box, to either the Howe YT 1000 recorder or the Telequipment oscilloscope S51B as required.

The electrode was activated by holding at +1.5 V for 5 minutes, then at -0.5 V for 1 minute in a flowing 1 M potassium chloride solution prior to starting a daily run. This, together with the selection of the working potential, ensured that slow electron transfer was not a rate limiting factor in the signal.

The experiment was conducted by switching from the supporting electrolyte to the electroactive solution. The slider action of the valve (SV) actuating a spring loaded microswitch which in turn closes a parallel RC circuit external to the event marker of the recorder. Thus a short pulse is presented to the

recorder by the remote action of the slider and registers the start of the experiment. The appearance time of the response signal was thus read from the pen recorder trace using the known chart speed. The ensuing rise curve was faithfully captured by photographing the corresponding oscilloscope trace from which a response time was calculated. The time base of the oscilloscope had previously being adjusted to a convenient valve between 10 ms m^{-1} and 100 ms m^{-1} and calibrated using a flow analogue signal of known time constant.

2.7.3 Flow visualisation

The flow profile developed in a delivery tube by switching streams was studied by photographing a concentrated solution of bromocresol green in borax buffer injected using a Rheodyne 5020 rotary valve, into PTFE tube of the same diameter as the stainless steel tube.

An Olympus OM30 camera fitted with a 50 mm lens on a Vivitar extension tube with f/8 aperature setting and a Miranda 650 flash unit was employed.

SECTION THREE

CHARACTERISATION OF A FLOW AMPEROMETRIC DETECTION SYSTEM RESULTS AND DISCUSSION

The impinging jet electrode designed by Fogg and Summan (146) was subsequently used amperometrically in a number of successful FIA applications (114-121). In this section, the fundamentals of the mode of operation and response of the device and its associated instrumentation is examined. This study is prompted by the exhortations of Stulik and Pacakova (74): "The dynamic properties of analysers (thus) depend on many factors, from the measuring principle, through the analyser design, to the particular experimental conditions. The dynamics of a given detector must therefore always be determined experimentally"; and of Poppe (156): "The dynamic behaviour of detection systems should be more carefully measured and described than is normally done in analytical chemistry".

The performance of the detector is described and interpreted in static and flowing solutions by stopped flow voltammetry and hydrodynamic voltammetry respectively. Next the dynamic response of the instrumentation and the detector itself are determined separately.

3.1 Stopped Flow Voltammetry

In the stopped flow mode the flowing sample is arrested in the detector cell and there subjected to the analytic process. Features of this mode are an increase in sensitivity for analyses based on slow chemistries and opportunities to introduce kinetic methods (17). In the electro-analytical field Wang (156) has utilised stopped flow with constant potential amperometry to achieve sensitive analyses by subtracting out non-flow dependent background currents, also the selectivity inherent in stopped-flow potential-scanning techniques has been demonstrated and utilised (17,157).

3.1.1 Results

Scans in the range 1-500 mVs^{-1} were recorded for the free working electrode and for the electrode in the fully assembled detector cell under stopped flow conditions.

Representative voltammograms are shown in Figure 3.1. Peak potentials (E_p) and peak currents (i_p) were recorded. E_p values lack accuracy at very high sweep rates due to the chart recorder, even when operating at its maximum upper limit of 10 mms^{-1}, being unable to faithfully keep up with the voltage scan rate.

These results are displayed in the comparative Table 3.1, in which the currents are corrected for the background contribution due to the buffer solution alone.

A statistical test of the repeatability of ip values at slow and fast scans was also carried out. The fully assembled detector cell was used in these measurements which are reported in Table 3.2.

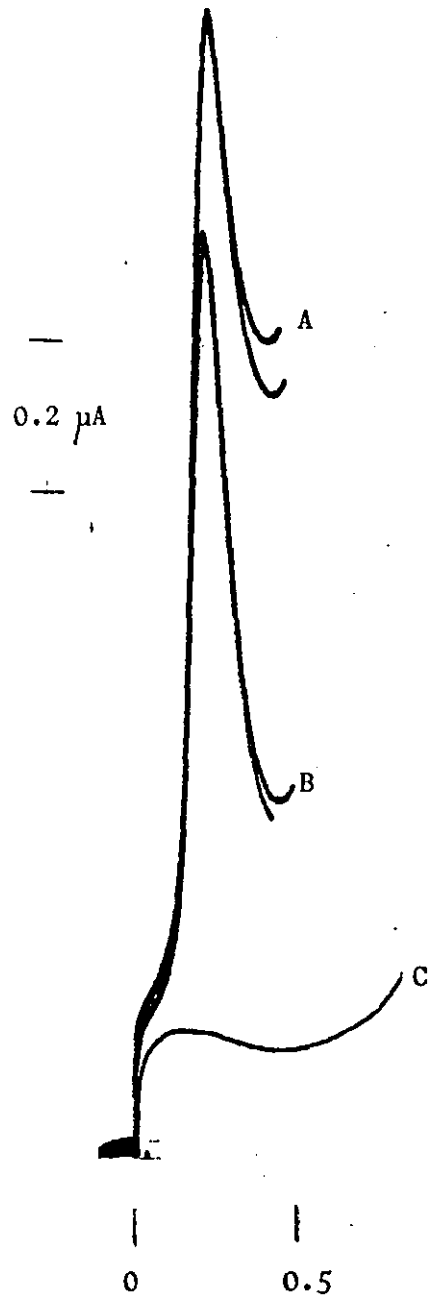

Fig. 3.1 Linear voltage sweep voltammograms. $2mVs^{-1}$.
0.744 mM Hexacyanoferrate(II) in pH 7 buffer.
(A) Free electrode, and (B) Stopped flow conditions;
duplicate scans shown in each case. (C) Residual current
for pH 7 buffer alone.

TABLE 3.1 Stopped Flow Voltammetry Results

Sweep rate (v)/ volt s^{-1}	ir at peak pot/ 10^{-6} A	Electrode in cell			Free electrode				(ip) cell / (ip) free
		Ep/ volts	peak current/ 10^{-6} A	ip/ 10^{-6} A	Ep/ volts	peak current/ 10^{-6} A	ip/ 10^{-6} A	$\frac{ip}{AC_v^{\frac{1}{2}}}$ *	
0.001	0.08	0.25	0.79	0.71	0.26	1.09	1.01	660	0.70
0.002	0.17	0.24	1.13	0.96	0.26	1.51	1.34	620	0.72
0.005	0.36	0.26	2.14	1.78	0.25	2.54	2.18	640	0.82
0.010	0.60	0.26	3.13	2.53	0.26	3.76	3.16	650	0.80
0.020	1.29	0.25	5.27	3.98	0.25	5.72	4.43	650	0.90
0.050	2.39	0.26	10.00	7.61	0.26	9.80	7.41	685	1.03
0.100	3.88	0.27	15.62	11.74	0.25	15.02	11.14	730	1.05
0.200	6.57	~0.27	22.69	16.12	~0.25	21.89	15.32	710	1.05
0.500	11.70	~0.27	32.59	20.89	~0.25	33.58	21.88	640	0.95

Electrode area (A) = 0.065 cm^2 Hexacyanoferrate(II) conc (C) = 0.74 x 10^{-6} mol cm^{-3}

i_r is the residual current due to buffer solution alone

* In the stated units.

Table 3.2 - Peak Current Repeatability

(a) Sweep rate : 5 mVs^{-1}

Successive i_p values/μA :

1.82 1.89 1.94 1.79 1.82 1.78

Mean = 1.84 μA

Relative standard deviation = 3.5%

(b) Sweep rate : 200 mVs^{-1}

Successive i_p values/μA :

19.80 20.20 19.90 19.60 21.99 23.98

Mean = 20.90 μA

Relative standard deviation = 8.5%

The final value of 23.98 μA in Table 3.2(b) was suspected of being an outlier.
On application of the Dixon-Q test (158) a value of 0.45 was obtained for Q defined as:

$$Q = \left| \frac{\text{Suspect value - nearest value}}{\text{Largest value - smallest value}} \right|$$

This was less than the critical value of Q of 0.621 at the 95 per cent confidence level for a sample size of 6. The value was thus retained.

i_p values reported were corrected from the measured values by the subtraction of background currents.

3.1.2 Discussion

3.1.2.1 Free Electrode Behaviour

E_p values for the free electrode are self-consistent and may be represented by the value of 0.26 volts vs S.C.E. Literature values for hexacyanoferrate(II) oxidation at glassy carbon are:

E_p/volts vs S.C.E.	Medium	Reference
0.28*	1 M KCl	(110)
0.33	pH 1.0	(159)
0.28	pH 4.2	(159)
0.29	pH 6	(160)
0.28	pH 8.5	(160)

*This was transposed from the reported $E_{p/2}$ value of 0.22 volt vs SCE, assuming reversibility, from (161):

$$E_p - E_{p/2} = 0.057$$

It should be noted that Ep values are influenced by pH and anion composition (162).

The peak current in linear voltage sweep voltammetry under semi-infinite linear diffusion conditions is given by the Randles-Sevcik equation, which for a single-electron transfer step may be written (163):

$$i_p = 0.452\ F^{3/2} \left(\frac{Dv}{RT}\right)^{1/2} AC$$

or

$$i_p = 2.72 \times 10^5\ A\ D^{1/2} C\ v^{1/2} \qquad 3.1$$

Where i_p is the peak current (amps), A is the electrode area (cm^2), v is the voltage sweep rate (volt s^{-1}), C is the concentration of the electroactive species (mol cm^{-3}) and D its diffusion coefficient ($cm^2\ s^{-1}$).

The parametric group $ip/ACv^{1/2}$ is thus identifiable with the constant $2.72 \times 10^5 D^{1/2}$, and here takes the value 680 in the stated units when utilising the hexacyanoferrate (II) diffusion coefficient (D) of 0.63×10^{-5} cm^2 s^{-1} (164). The average value obtained from the data in Table 3.1 is 665±40. Experimental values ranging from 410 to 860, depending on supporting electrolyte composition, are quoted by Noel et al. (162).

Thus the working electrode is well-behaved electrochemically giving i_p and E_p values consistent with theoretical and literature values. This conclusion validates the efficiency of the activation programme.

3.1.2.2 Comparison of i_p values

The response of the electrode in the detector cell is compared to the free electrode under various conditions as the ratio of peak currents in Table 3.1.

These results suggest that the electrode has a lower response in the cell at slow scans but it is not noticeably different from the free electrode at high scans above 20 mVs^{-1}. This conclusion was supported by a statistical test in which six successive measurements were made over a five hour period, each incorporating activation and conditioning steps. At a sweep rate of 5 mVs^{-1} a relative standard deviation in i_p of 3.5 per cent was obtained but this increased to 8.5 per cent at 200 mVs^{-1} (Table 3.2). The low precision at high sweep rates is due to a reduced signal-to-noise ratio resulting from an enhanced capacity current,

which varies directly with sweep rate in contrast to the faradaic process which increases only as the square-root of the sweep rate (163). Even so, these deviations are less than those reported in Table 3.1, so the reduced response at slow voltage scans when the solution is confined to the cell chamber appears to be real.

3.1.2.3 Restricted Diffusion

With linear voltage sweep at a stationary electrode, the electron transfer rate increases with potential but the rate of diffusion decreases as the diffusion layer thickens with time. The signal thus exhibits a peak.

A general equation for a diffusion limited electrochemical current can be obtained by combination of Faraday's laws and Fick's first law of diffusion viz, for single electron transfer:

$$i = FAD \frac{C}{\delta_{dL}} \qquad 3.2$$

With the implied assumption of the existence of a linear concentration gradient of thickness δ_{dL} extending from the surface of the electrode. An estimate of this parameter at the peak maximum can be obtained by identifying equation 3.2 with the Randles-Sevick equation (3.1) to give:

$$\delta_{dL} = 2.21 \left[\frac{DRT}{Fv}\right]^{1/2} \qquad 3.3$$

i.e. for hexacyanoferrate (II) oxidation.

$$\delta_{dL} = 8.90 \times 10^{-4} \, v^{-1/2}$$

Expected values are tabulated:

Sweep rate/mVs^{-1}	1	2	4	10	20	50	100	200	500
$\delta_{dL}/10^{-3}$cm	28	20	13	9	6	4	3	2	1

The geometric thickness of the detector cell is reported to be 25×10^{-3} cm (146). Thus the diffusion layer will extend to the cell boundary at sweep rates up to at least 2 mVs^{-1} and probably at faster rates as δ_{dL} underestimates the zone of solution depletion due to actual concentration gradients possessing greater curvature than the linear case (165). This situation will modify the response compared to the free electrode as the boundary condition:

$$\text{conc} \longrightarrow 0 \quad \text{as } x \longrightarrow \infty$$

replaces:

$$\text{conc} \longrightarrow C \quad \text{as } x \longrightarrow \infty$$

3.1.2.4 Thin Layer Electrolysis

When a linear voltage sweep is applied to a closed, finite volume of solution, the current response is symmetrical and bell-shaped (166) as in Fig. 3.2.

The concentration of the electroactive is uniform in the thin layer cavity and for Nernstian response the peak potential corresponds to the standard electrode potential, $E^{\ominus}$; also the peak current for a single electron transfer is given by:

$$i_p = \frac{CvAbF^2}{4RT} \qquad 3.4$$

The electrolysis is exhaustive so that the faradaic component eventually decays to zero.

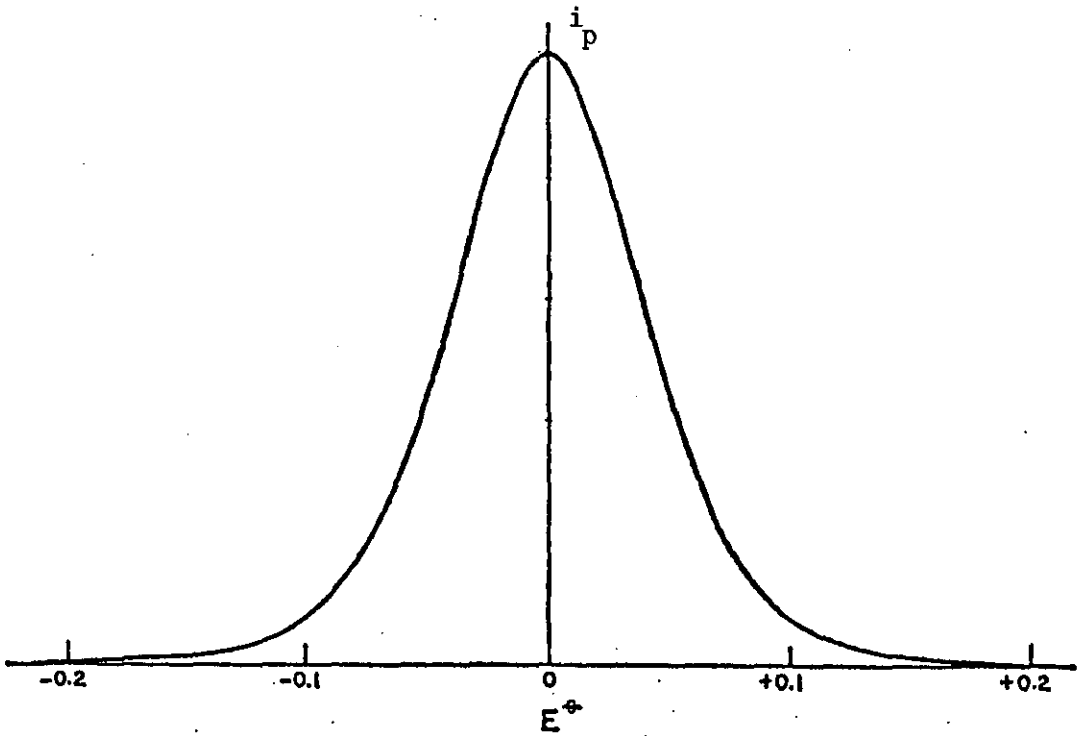

Fig. 3.2 Theoretical thin-layer electrolysis voltammogram

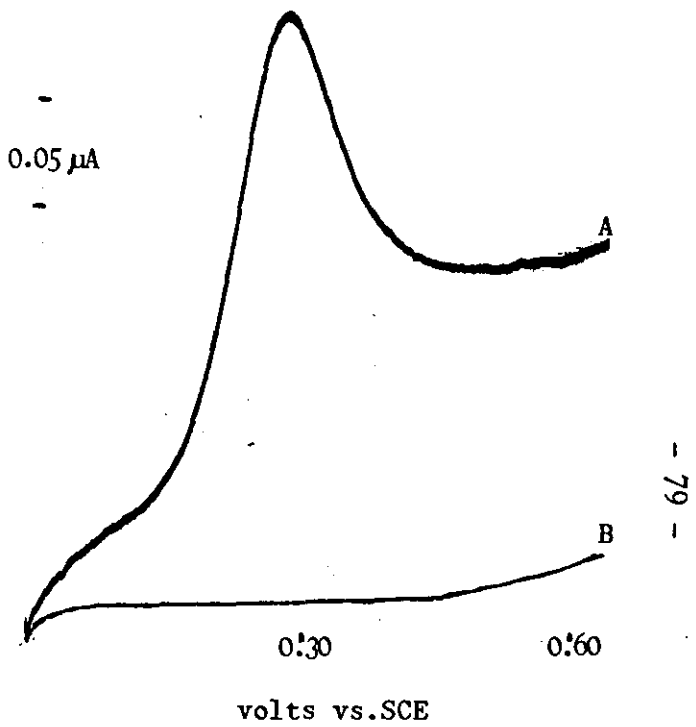

Fig. 3.3 Linear voltage sweep voltammogram. 0.2 mV s^{-1}.(A) 0.746 mM hexacyanoferrate(II) in pH 7 buffer. (B) Residual current in pH 7 buffer alone. Stopped flow conditions.

Thin layer electrolysis (TLE) should be displayed in a cell of thickness b when the sweep rate (v) is at least (167):

$$v = \frac{DRT}{Fb^2} \qquad 3.5$$

i.e. in this case, when the sweep rate is $0.25\ mVs^{-1}$.

In contrast to the free electrode, this slow sweep is accessible in the cell where the growing diffusion layer is shielded from disruptive convection. The resulting voltammogram is shown in Fig. 3.3. Although the measured peak current, $0.27\mu A$, is the same order of magnitude as that predicted from equation 3.4, viz. $0.22\mu A$, it is clear that TLE has not been achieved since the electrolysis is not exhaustive and the peak potential at 0.288 volts is far more anodic than the $E^{\ominus}$ value of 0.214 volt vs SCE recorded on this couple by TLE in a 0.64 µl cell with wire electrodes (168).

This failure may be attributed to an edge effect. The diffusion layer, defined by the electrode area and cell thickness, has a volume of 1.6 µl. However, this is surrounded by a trapped layer of solution which is estimated by direct measure to be approximately 25 µl in volume. This ring of solution provides a lateral flux of depolariser into the electrolysis zone at extended diffusion times, thus vitiating the semi-finite or bounded condition necessary for TLE.

3.1.2.5 Conclusion

Linear sweep voltammetry can be applied in the cell under stopped flow conditions. At fast scans infinite diffusion conditions apply and results are obtained as for the free electrode. However, at slow scans, when the growing diffusion layer approaches that of the cell depth, diffusion is restricted and a reduced response occurs; although since the depletion zone is not strictly a closed system, true thin layer electrolysis cannot be attained.

It is interesting to observe that true thin layer response has been achieved by others under stopped flow conditions using a reticulated vitreous carbon electrode where the electrolysis was confined to pores of diameter 0.025 cm (169).

3.2 Hydrodynamic Voltammetry

Although hydrodynamic voltammetry is a method of analysis in its own right (170), it is used in this study as a means of defining the nature of the amperometric response of the electrode. This is achieved through examination of the factors determining the limiting current (i_L), particularly the effect of the volumetric flow rate (V_f). Restating equation 2.1:

$$i_L = (\text{constant}) C V_f^{\alpha} \qquad 3.6$$

α is diagnostic of the nature of the electrode response (Table 1.2). This exponent was determined over a range of flow rates for a fixed concentration of electroactive species (C), and the equation is then examined explicitly using theoretically evaluated constant terms at fixed flow rates for a range of electroactive concentrations.

3.2.1 Results

3.2.1.1 Electrode Activation

In order to apply theoretical equations confidently to a solid electrode requires a well activated sensor. This was achieved using the electrochemical pretreatment outlined in Section 2.3. Consistently good voltammograms were obtained with typically $E_{1/2}$ of 0.229 V vs SCE and a slope ($E_{3/4} - E_{1/4}$) of 74 mV. This data was collected from a slow scan of 2 mVs^{-1} at V_f of 4.5 ml min^{-1}, the $E_{1/2}$ value being transposed from the potential measured with the Ag/AgCl electrode using thermodynamic data (171). These values compare well with the $E_{1/2}$ of 0.226±0.004 V vs SCE recorded after an efficient three stage metallographic polishing procedure (172) and the steep voltammograms ($E_{3/4} - E_{1/4}$ = 92±6 mV) recorded after electrochemical treatment (173).

3.2.1.2 Effect of flow rate on limiting currents

Hydrodynamic voltammograms were recorded over two flow rate regions and these are shown in Figs. 3.4(a) and 3.5(a). The lower range is typical of the flow rates used in HPLC whereas the higher range is used in FIA, where there is greater freedom from back-pressure constraints, to achieve high sample frequency and sensitivity. The values for the limiting current (i_L) were measured on the plateaux of the waves after correcting for he background current, which was independent of the flow rate. The apparent flow-rate exponent (α) is given by the slope of the graph of $\log_{10} i_L$ vs $\log_{10} V_f$ and changes gradually from 0.41 to 0.67 over the total V_f range [Figs. 3.4(b) and 3.5(b)].

Particular experimental conditions pertaining to these results are described below:

(a) Flow rate range 0.41 to 1.54 min^{-1}, by peristaltic pumping.
Electroactive solution was 0.75 mM $Fe(CN)_6^{4-}$ in 1M KCl.
Voltage scan rate was 5 mVs^{-1}.
Activation by electrochemical pretreatment at +1.5V for 5 min. followed by -0.5V for 1 min. prior to recording the complete set of voltammograms.
Limiting currents measured at +0.7 V vs Ag/AgCL.

(b) Flow rate range 1.3 to 7.1 ml min^{-1}, by hydrostatic head.
Electroactive solution was 0.75 mm $Fe(CN)_6^{4-}$ in 1M KCl.
Voltage scan rate was 5 mVs^{-1}.
Activation by electrochemical pretreatment at +1.75 for 5 min. followed by -1.0V for 1 min. prior to recording each voltammogram.
Limiting currents measured at +0.7 V vs Ag/AgCl.

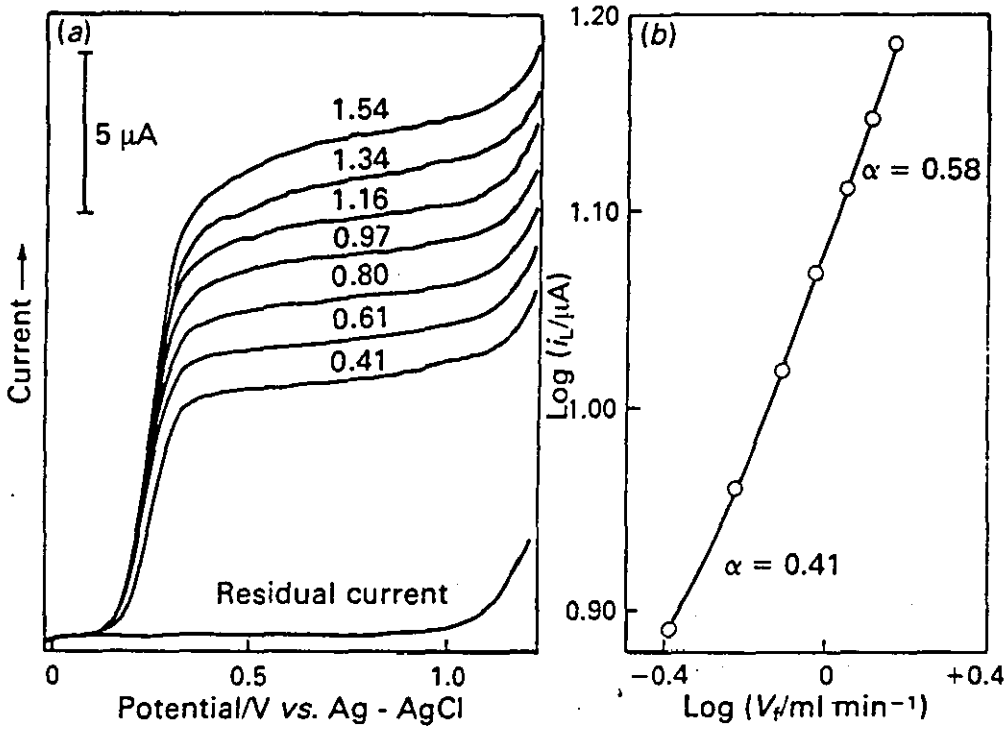

Fig. 3.4 (*a*) Residual current for 1 M KCl and voltammograms with 0.75 mM hexacyanoferrate(II) added. Linear voltage scans at 5 mV s^{-1}. Flow-rates given in ml min^{-1}. Residual current independent of flow-rate. (*b*) Log i_L *vs.* log V_f. Data from Fig3.4(*a*). i_L measured at 0.7 V *vs.* Ag - AgCl. α = Apparent flow exponent

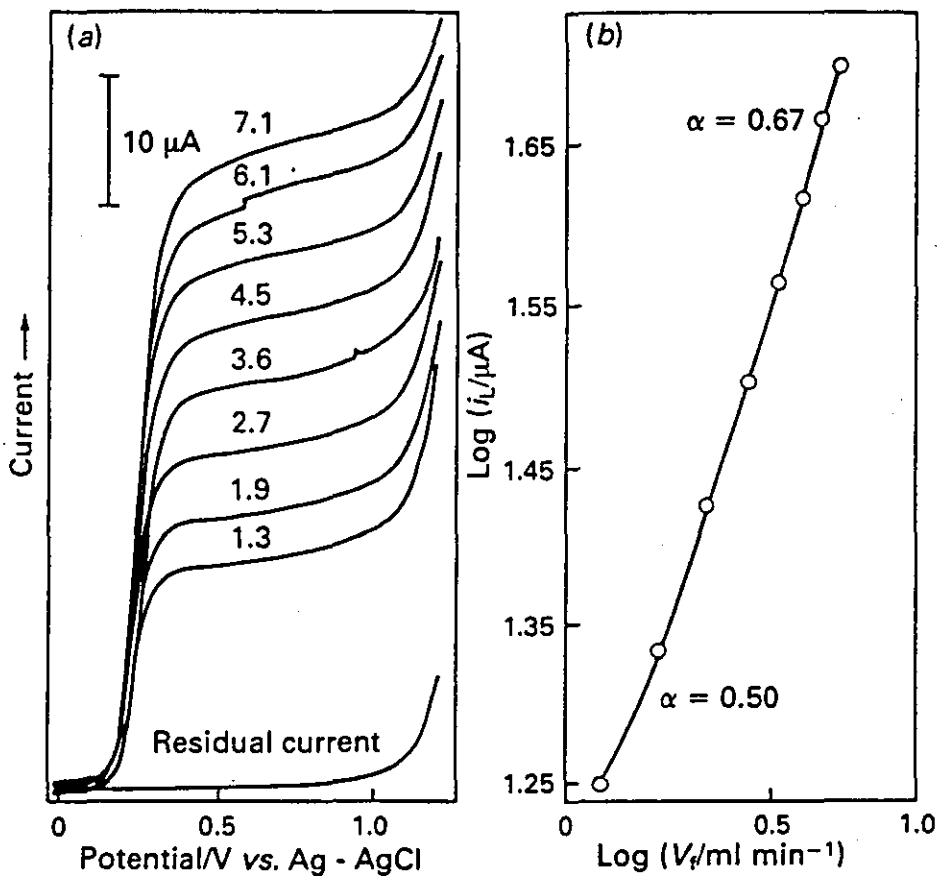

Fig. 3.5 (*a*) Residual current for 1 M KCl and voltammograms with 0.75 mM hexacyanoferrate(II) added. Linear voltage scans at 5 mV s^{-1}. Flow-rates given in ml min^{-1}. Residual current independent of flow-rate. (*b*) Log i_L *vs.* log V_f. Data from Fig3.5(*a*). i_L measured at 0.7 V *vs.* Ag - AgCl. α = Apparent flow exponent

Essentially similar results at the higher flow rates were obtained with peristaltic pumping as with the hydrostatic head but with a higher noise level particularly at fast flows. The Reynolds Number (Re) for jet flow from a nozzle is given by (174):

$$Re = \frac{\text{linear velocity x nozzle diameter}}{\text{kinematic viscosity}} \qquad 3.7$$

Using the value 10^{-2} cm^2 s^{-1} for the kinematic viscosity of water and a nozzle diameter of 0.035 cm which apply to this study, then the range of Re values increases from 24 to 424 as the flow rate increases from 0.4 to 7.0 ml min^{-1}. Although these values are not excessive, turbulence does occur in jets at lower Reynolds Numbers than in pipe flow, typically with a critical value <1000 (174). It may be conjectured that residual pulsations in the pumped system produces turbulence in the narrow confines of the electrode channel at lower flow rates than does continuous flow induced hydrostatically. Attempts to visualise the jet flow were made on a stream of potassium permanganate solution flowing through the electrode nozzle unconfined into a breaker of ferrous sulphate. At the highest flow rates, the extended jet had greater integrity when produced by hydrostatic means than by peristaltic pumping.

3.1.2.3 Effect of concentration on limiting currents

The voltammograms obtained with various concentrations of hexacyanoferrate (II) at flow rates of 0.58 and 0.31 ml min^{-1} are shown in Fig. 3.6(a) and (b) respectively. As predicted by theoretical relations, the limiting current (i_L) is directly proportional to the electroactive species

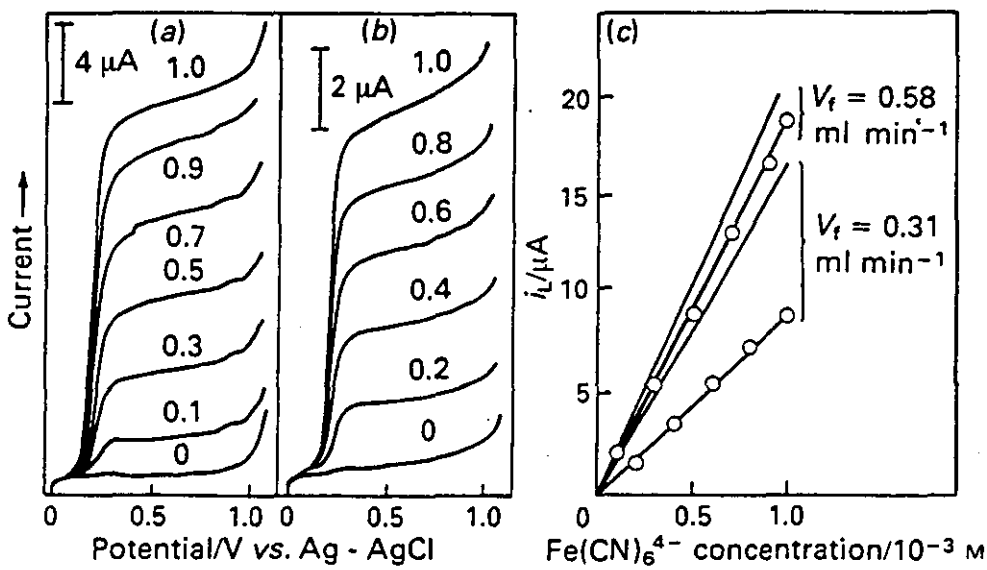

Fig. 3.6 (*a*) Voltammograms at a flow-rate of 0.58 ml min^{-1}. Concentrations of hexacyanoferrate(II) in 1 M KCl given in mM. Linear voltage scans at 5 mV s^{-1}. (*b*) Voltammograms at a flow-rate of 0.31 ml min^{-1}. Concentrations of hexacyanoferrate(II) in 1 M KCl given in mM. Linear voltage scans at 5 mV s^{-1}. (*c*) Limiting current *vs.* concentration. (○) Data from Fig3.6(*a*) and (*b*). Solid line, model calculations taking b (see Fig3.7) as 0.025 cm

concentration [Fig. 3.6(c)] and demonstrate the analytical utility of the technique. The theoretical plots are also shown in Fig. 3.6(c) and are discussed later. Particular experimental conditions pertaining to these results were:

Flow maintained by peristaltic pumping.
Electroactive solution was 0-1.0 mM $Fe(CN)_6^{4-}$ in 1M KCl.
Voltage scan rate was 5 mV s^{-1}.
Activation by electrochemical pretreatment at +1.5 V for 5 min. followed by -0.5 V for 1 min. prior to recording each set of voltammograms.
Limiting currents measured at +0.7 V vs Ag/AgCl.

3.2.2 Hydrodynamic Model of Detector Cell

3.2.2.1 Flow Regions

In a practical impinging jet cell a mixed response is possible. Following Elbicki et al. (90), the flow shown in Fig. 3.7 comprises three regions: a central, stagnation zone where the flow is perpendicular to the electrode, a mid-zone exhibiting wall-jet hydrodynamics until the boundary layer fills the chamber, followed by a region of thin layer, laminar, parabolic flow. All flows are axially symmetrical and each zone contributes a component to the total current.

(i) Stagnation Region

Electrochemical measurements at a chamber width to nozzle width (b/a) ratio of 1.0 indicate that the stagnation region matches the cross-sectional area of the nozzle at low Re values but is twice as large for turbulent nozzle flow (102). Similar

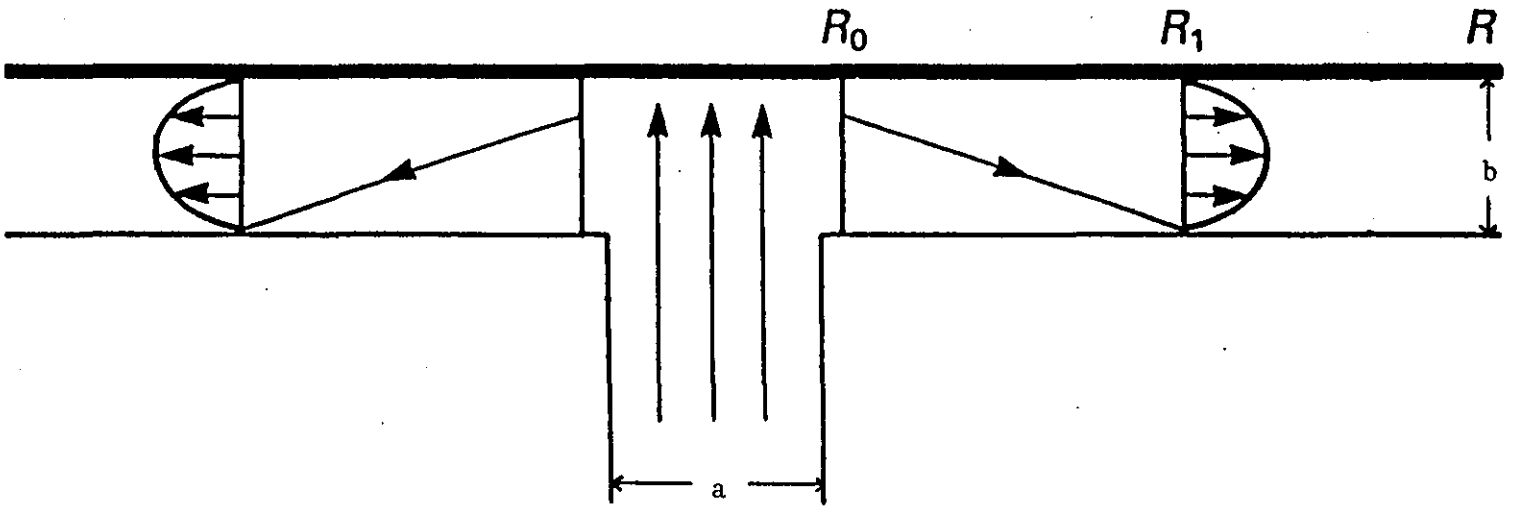

Fig. 3.7 Schematic cross-section through detector.
Channel width, b. Nozzle diameter, a.
Flow stream lines indicated: perpendicular flow out to R_o, oblique flow out to R_1 and finally parallel flow out to R.

conclusions were obtained from direct measure of an air jet impinging on a naphthalene surface. Thus with b/a ratio of 0.5 a transition from the stagnation to the wall-jet region occurs at a radius of 1.2 times the radius of the nozzle (175). This latter distance is chosen to define the stagnation zone in this model (R_o). For free, uniform flow perpendicular to the electrode, the limiting current is given by (100):

$$i_s/A = 1.673\ n\ FCD^{2/3}\ \nu^{-1/6}\ U^{1/2}\ R_o^{3/2} \qquad 3.8$$

This equation strictly applies as $^{b}/_{a} \to \infty$. Chin and Tsang (102) have reviewed stagnation flow from jets in terms of this dimensionless nozzle height. Of particular interest here, where $^{b}/_{a}$ is 0.7, is the mass transfer equation:

$$Sh = 1.0827\ Re^{1/2}\ Sc^{1/3} \qquad 3.9$$

applying to laminar, non-uniform jet flow. With the usual substitutions, this gives for the limiting current:

$$i_s/A = 3.40\ nFCD^{2/3}\ \nu^{-1/6}\ U^{1/2}\ R_o^{2}\ a^{-1/2} \qquad 3.10$$

However since the stagnation zone occupies only a minor part of the electrode area in the detector being studied here, the values predicted by each equation in the V_f range of interest (0.25 - 8.0 ml min^{-1}) are very similar viz. 0.5 - 3.1μA from equation (3.8) and 0.9 - 4.9μA from equation (3.10), so the choice between the two would not qualitatively affect the model. However, this might not be the case for wider nozzles and/or smaller electrodes. Since equation (3.10) addresses itself to a confined jet it has been

preferred in subsequent calculations, although the short length of the nozzle tube, viz. 0.1 cm (146) makes the assumption of parabolic, non-uniform jet flow doubtful above ca. 0.8 ml min^{-1} due to the pipe-entry effect where the distance required to establish a coherent flow pattern exceeds this dimension (152).

(ii) Wall-jet hydrodynamic boundary layer thickness

Gunasingham and Fleet (105) have given a derivation of this boundary thickness from a consideration of the skin friction coefficient; viz. equation 1.24:

$$\delta_{bl} = 5.8\, \pi^{3/4}\, a^{1/2}\, \nu^{3/4}\, x^{5/4}\, \phi^{-3/4}$$

x being the radial distance from the centre of the electrode. Thus the outer rim of the wall-jet region (R_1) is defined by:

$$R_1 = \left(\frac{b\phi^{3/4}}{5.8\, \pi^{3/4}\, a^{1/2}\, \nu^{3/4}} \right)^{4/5} \qquad 3.11$$

Most noteworthy is the increase in R_1 with flow-rate.

(iii) Wall-jet ring region

The limiting current in this region is given by (94):

$$i_{WJ}/A = 1.38\, n\, FCD^{2/3}\, \nu^{-5/12}\, \phi^{3/4}\, a^{-1/2}\, [R_1^{9/8} - R_o^{9/8}]^{2/3} \qquad 3.12$$

(iv) Thin layer ring region

The limiting current in this region is given by (91):

$$i_{TL}/A = 3.15\ n\ FC\phi^{1/3}\ b^{-2/3}\ D^{2/3}\ [R^2 - R_1^{\ 2}]^{2/3} \qquad 3.13$$

3.2.2.2 Explicit equations

The variables, corresponding to the cell and solutions employed experimentally, are given the values: $D = 0.6 \times 10^{-5}$ cm^2 s^{-1} (164), $\nu = 0.01$ cm^2 s^{-1}, which is the value for water; $C = 0.75 \times 10^{-6}$ mol cm^{-3}, $a = 0.035$ cm, $R_o = 0.021$ cm and $R = 0.143$ cm. This allows the equations referred to above to be written explicitly in terms of the principal parameters of chamber depth and volumetric flow rate as:

$$i_s/\mu A = 1.72\ v_f^{1/2} \qquad 3.14$$

$$R_1/cm = 0.64\ b^{4/5}\ v_f^{3/5} \qquad 3.15$$

$$i_{WJ}/\mu A = 55.56\ [R_1^{9/8} - 0.01296]^{2/3}\ v_f^{3/4} \qquad 3.16$$

$$I_{TL}/\mu A = 19.21\ b^{-2/3}[0.02045 - R_1^{\ 2}]^{2/3}\ v_f^{1/3} \qquad 3.17$$

These apply with the general condition: $R_o < R_1 < R$

The total current is: $i_L = i_s + i_{WJ} + i_{TL}$ 3.18

3.2.2.3 Classification of behaviour

In the detector being studied here b takes the nominal value of 0.025 cm. Using this, calculations have been performed in the appropriate flow domain to provide data for comparison with experiment. However, to place the behaviour of

this cell in a wider context, the calculations are accompanied by those taking other values for b, but with the same values for the complementary parameters.

Fig. 3.8 shows the development of the radius R_1 with V_f for the particular values of b chosen. From this, four classes of behaviour can be discerned in the V_f range given. Two limiting cases are discussed first:

(I) $R_1 = R_o$ throughout flow range.

In sufficiently narrow cells the wall-jet boundary layer extends to the channel wall even at its highest flow rate, occurring here if $b \leqslant 0.003$ cm. The electrode functions in a stagnation/thin layer manner.

(IV) $R_1 = R$ throughout flow range.

The wall-jet boundary layer is contained within the chamber even at the lowest flow rate limit. The electrode functions in a stagnation/wall-jet mode throughout, occurring here when $b \geqslant 0.435$ cm.

Next, in a limited, intermediate range of flows, R_1 will lie between R_o and R. The electrode will then be subject to stagnation/wall-jet/thin layer triple flow. However, in the context of the wide span of flows used in this study, the conditions is likely to be accompanied by each limiting case described above.

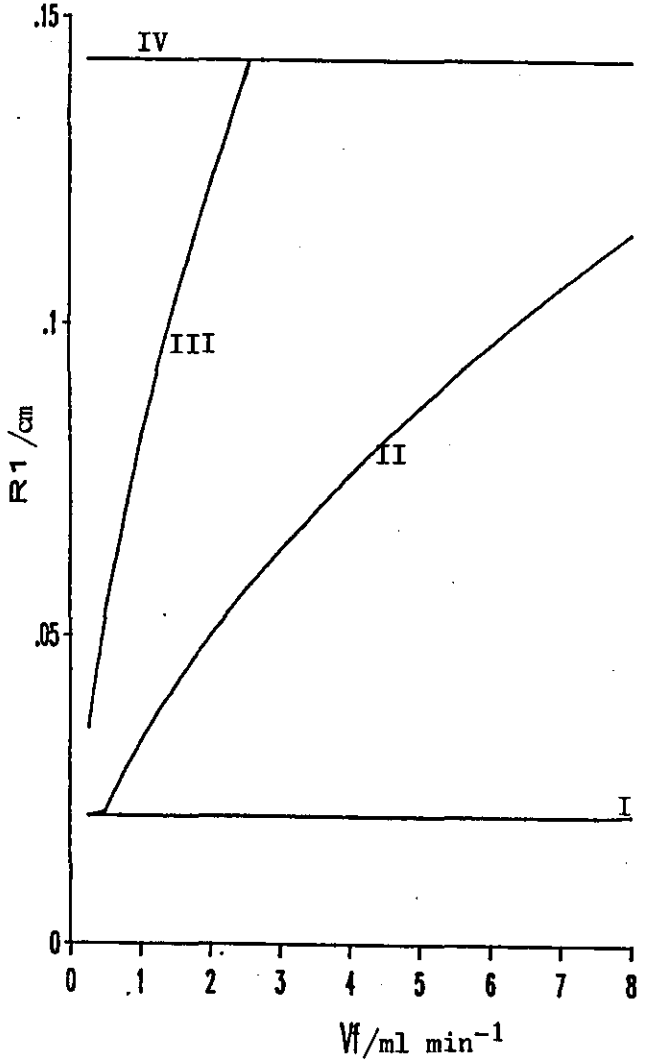

Fig. 3.8 Plot of equation 3.15, with the restriction $R_o \leq R_1 \leq R$. Values of the parameter b are I 0.003 cm; II, 0.025 cm; III, 0.075 cm; and IV, 0.430 cm.

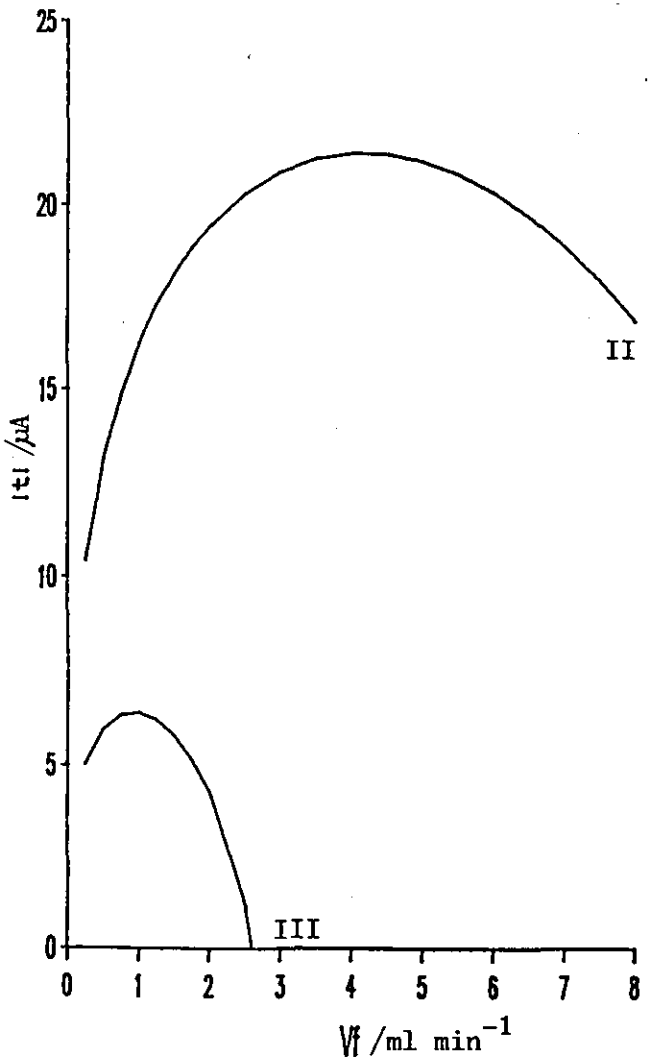

Fig. 3.9 Thin layer current component (from equation 3.17) vs. flow rate for cells exhibiting type II and III behaviour, taking b as 0.025 cm in II and 0.075 cm in III.

(II) $R_o \leqslant R_1 < R$ in a given flow range.

The flow evolves from stagnation/thin layer into the triple flow case. The thin layer current will show a broad maximum (Fig. 3.9) reflecting the competing influences of decreasing thin-layer area and increasing mass transfer with increasing V_f.

(III) $R_o < R_1 \leqslant R$ in a given flow range.

At low flows where $R_1 < R$, the electrode is subject to all three flow regimes as above. When $R_1 = R$, the thin layer contribution dies out and the electrode functions as a stagnation/wall-jet device. The thin layer current shows a sharp maximum in this case (Fig. 3.9).

3.2.2.4 Apparent Flow Exponent

Fig. 3.10 shows the resulting $\log_{10} i$ vs $\log_{10} V_f$ plots for all four classes of behaviour with the apparent flow exponent (α) calculated.

In the shallowest and deepest cells, classical thin-layer ($\alpha = 0.33$) and wall-jet ($\alpha = 0.75$) response are attained respectively, albeit with the slopes slightly modified due to the contribution from the stagnation region. In particular, the wall-jet line (IV) is a terminal case since the current is now independent of b, i.e. data from deeper cells would all fall along this line.

Type II and III behaviour yield intermediate results. In the former case, the α value increases between the limits 0.33 - 0.75 as the percentage wall-jet character increases. In the latter case, however, this pattern is disturbed as the thin

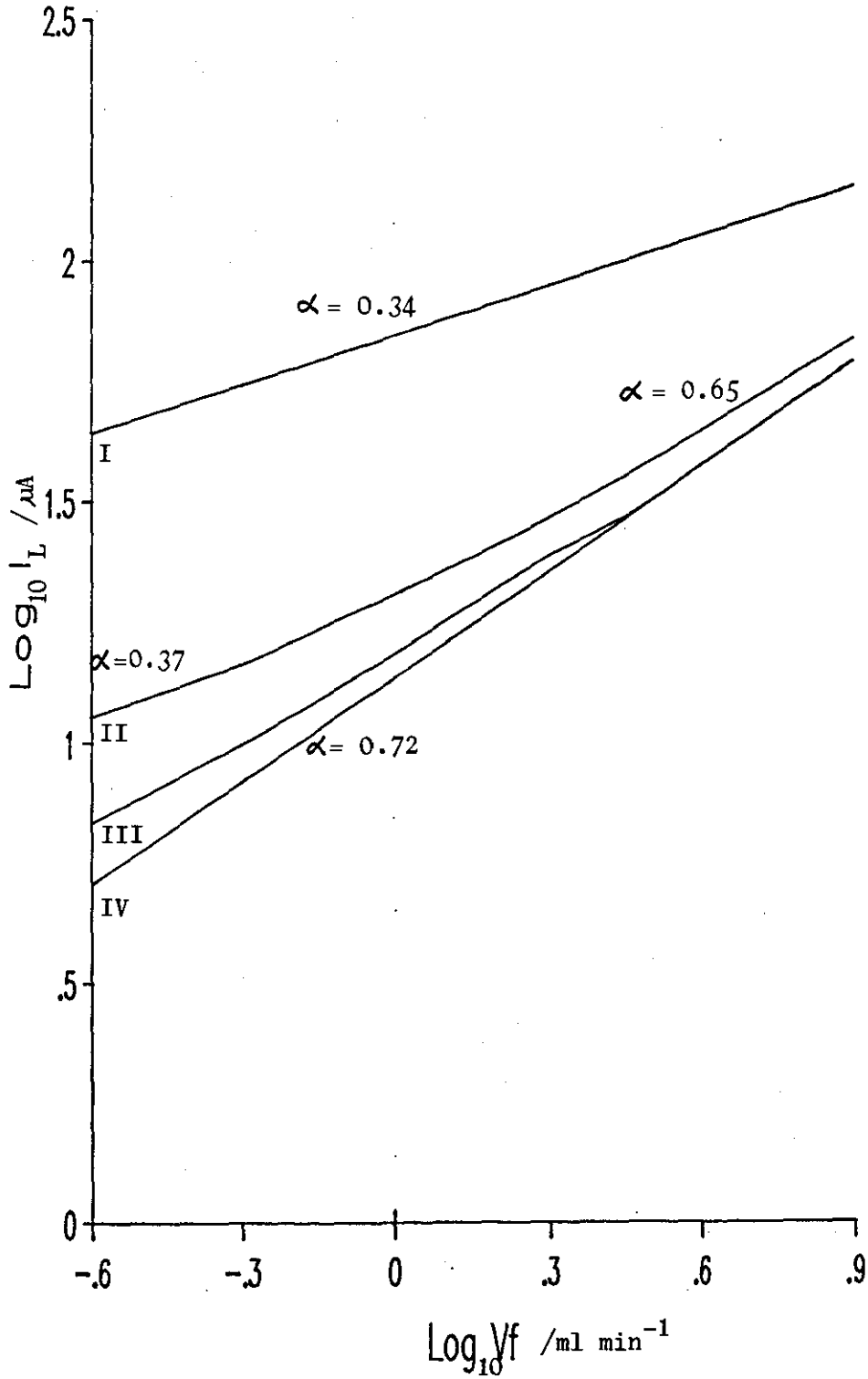

Fig. 3.10 Log_{10} vs. Log_{10} V_f for cells of Types I-IV
Apparent flow exponent (α) as indicated.

layer region rapidly dies out (Fig. 3.9) and there is a transition region before the response converts to stagnation/wall jet behaviour and the curve merges with the terminal case. In the transition region, the rapid decline of the mass-transfer efficient , thin layer contribution halts the rise in the total response and abnormally low α values may be recorded.

In theory, all these aspects of the flow response should be observable with a single cell, provided the flow range was sufficiently wide to provide the general condition, $R_o < R_1 < R$. Thus the detector being studied would be expected to function as a stagnation/thin layer device to 0.5 ml min^{-1}, followed by a region of steadily progressing wall-jet character to 10 ml min^{-1} when there would be a transition region coincident with the collapse of the thin layer component until stagnation/wall jet conditions prevail at 11.5 ml min^{-1}. However, in practice, the upper flow rates are probably not accessible since the critical Re for turbulent flow is considerably lower for jets than for pipe-flow (174).

3.2.3 Discussion

From the match in α values between experimental [Figs. 3.4(b), 3.5(b)], and model curves (Fig. 3.10, curve II), it may be diagnosed that the detector being studied approaches Type II behaviour in the flow range studied.

Direct comparison of measured and model total currents is given in Fig. 3.6(c). Although experimental and theoretical results are of the same order of magnitude, the correlation lacks precision.

Apart from small systematic errors in the values of D and Γ, there is a large uncertainty in the value of b. This is because in the detector cell the electrode is placed in position by hand and eye and a reproducible value for b cannot be guaranteed. Also, the test is particularly severe because at the low flow rates employed the thin layer component, which is very sensitive to the exact value of b, is predominant. A quantitative test of the model would require a chamber set with micrometer accuracy.

The model can also be used in commentary on other published work. Thus in the classic study on the wall-jet electrode (94) it was necessary that b exceed 0.2 cm and R be greater than 0.15 cm to achieve theoretical response, i.e. the cell was functioning in a type IV manner with negligible contribution from the stagnation region. Similarly a study is reported under conditions where type I conditions were expected; this was confirmed with an experimental α value of 0.36 (91). Intermediate conditions probably prevail in results reported by Gunasingham and Fleet (105), where in narrow cells ($b<0.05$ cm) α is <0.5 below 2 ml min^{-1} but approaches 0.75 at high flows, and by Hanekamp and van Nieuwerk (87) where an α value of 0.44 is reported for the Metrohm EA 1096 cell. Unusually low α values of 0.29 (176) and 0.16 (177) in impingement cells at slow flow rates might indicate the occurrence of the transition zone with type III behaviour.

3.2.4 Conclusion

The impinging jet amperometric electrode studied here thus shows a composite stagnation/wall-jet/thin layer response, the percentage wall-jet character increases at the expense of the thin layer component as the flow rate increases.

The flow rate exponents quoted apply only under the steady-state conditions achieved with hydrodynamic voltammetry. When used as a detector in HPLC and FIA, the transient signal is also influenced by the dispersion properties of the experiment (107, 108). However, the stated mode of action of the detector remains valid.

3.3 Instrumentation Response

3.3.1 Theory of the FI Analogue Characteristic

As discussed in Section 1.2.2., the continuous stirred reactor (CSTR) represents an idealised mixing stage in a transport process. The single tank has been adopted to model the FI process (60), which in its simplest form consists of the transportation of the analyte from the point of injection to the detector without reaction [Fig. 1.1(b)]. In the model, the dispersion in the transmission line is equivalent to the mixing in a single CSTR stage [Fig. 1.7(a)]. The concentration of analyte in the sample is C^o. A small volume of this solution is injected into the carrier as a slug and on reaching the detector produces the idealised FIA characteristic shown in Fig. 3.11. The leading edge of the slug initiates a F curve response but when the following edge reaches the detector at t_p, a wash process takes over, producing a W curve from the peak maximum at C_p. The shape of this characteristic can be described by the following parameters:

residence time (τ)
fraction of peak signal (f) = C/C_p
dispersion (D_s) = C^o/C_p
and peak width (Δt) = $t_2 - t_1$

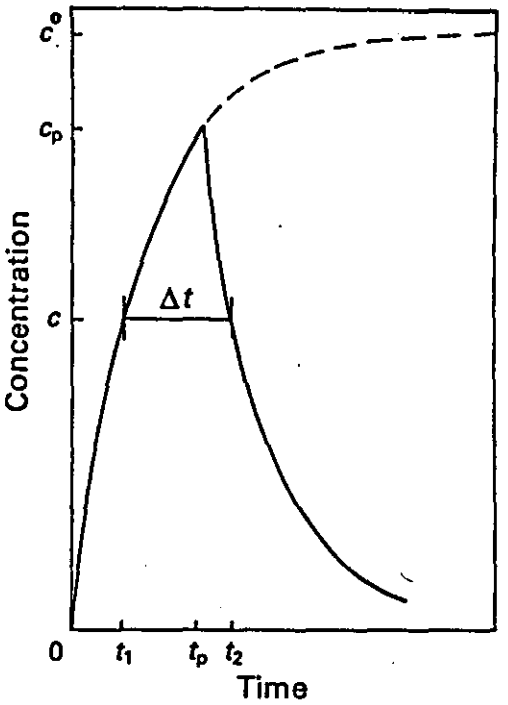

Fig. 3.11 Idealised FI response characteristic: c°, concentration of the injected sample; c_p, peak maximum concentration at time t_p; Δt, peak width at an arbitrary concentration at times t_1 and t_2

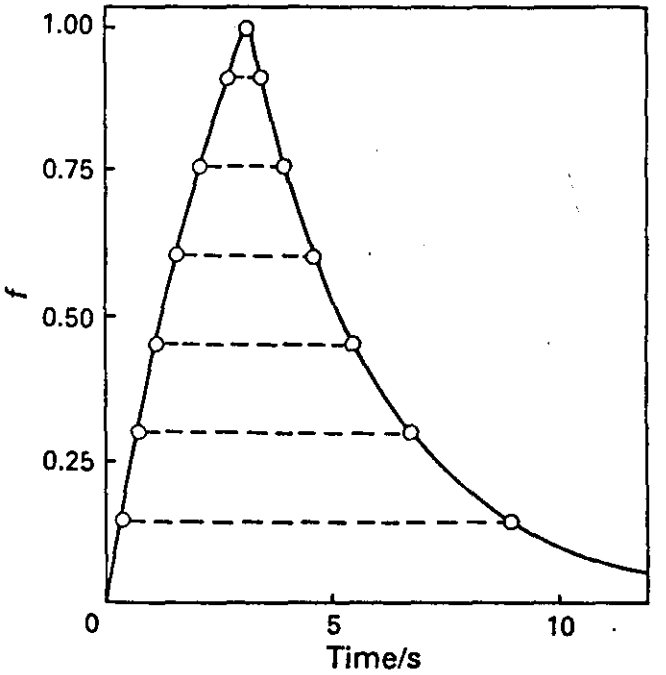

Fig. 3.12 Pulse trace from the analogue obtained with the Howe YT1000 recorder. Chart speed, 10 mm s^{-1}. Analogue output: τ, 3 s; D, 1.359. Hatched lines joining experimental points (O) represent peak width Δt values calculated from equation 3.24

The relationship between the parameters is obtained from the component F and W curves:

t_1 is determined from the F curve. Using equation 1.2:

$$C = C^o [1 - \exp(- t_1/\tau)] \qquad 3.19$$

or in parametric form:

$$t_1 = \tau \ln\left[\frac{D_s}{D_s - f}\right] \qquad 3.20$$

and at the peak maximum:

$$t_p = \tau \ln\left[\frac{D_s}{D_s - 1}\right] \qquad 3.21$$

t_2 is determined from the W curve. Using equation 1.3:

$$C = C_p \exp[- (t_2 - t_p)/\tau] \qquad 3.22$$

or in parametric form:

$$t_2 = \tau \ln\left[\frac{D_s}{f\ (D_s - 1)}\right] \qquad 3.23$$

$$\text{Thus,} \quad \Delta t = \tau \ln\left[\frac{(D_s - f)}{f(D_s - 1)}\right] \qquad 3.24$$

This expression is equivalent to that obtained by Tyson, quoted earlier as equation 1.8 (7).

The object of the electronic analogue, described in Section 2.6.1, is to simulate this characteristic and the full F curve by substituting voltages for concentrations, at D_s values selected by the voltage triggering level and at τ values given by the RC product.

3.3.2 Validation of the FI Analogue Characteristic

Fig. 3.12 shows the display obtained with the pen recorder using τ = 3s and D_s = 1.359 from the RC analogue; the Δt data points shown were calculated at selected f values from equation 3.24. The trace demonstrates that accurate analogue signals can be generated.

3.3.3 Electrochemical Module and Signal Matching Box Response

Many instruments have in-built exponential time constant circuitry to reduce high-frequency noise, but this can introduce over-all signal distortion. This effect can be demonstrated with the EDT module. F-curves were obtained with and without operation of the filter circuit (Fig. 3.13). The convoluted arrangement used, viz.

analogue function * filter circuit response
$(1 - e^{-t/\tau}, \tau = 1.2s)$ * $(e^{-t/\tau}, \tau = 1.2s)$

corresponds in transport terms to the response from two tanks in series having equal volumes (61):

$$C/C^o = 1 - e^{-t/\tau} (t/\tau + 1) \qquad 3.25$$

The experimental curves shown in Fig. 3.13 agree well with theoretical prediction. Thus the unfiltered curve follows equation 1.2, with a residence time of 1.2s corresponding to the 0.63 fraction as predicted. The filtered curve is distorted and follows equation 3.25, with the total residence time (2τ) corresponding to 2.4s occurring at the 0.59 fraction as predicted.

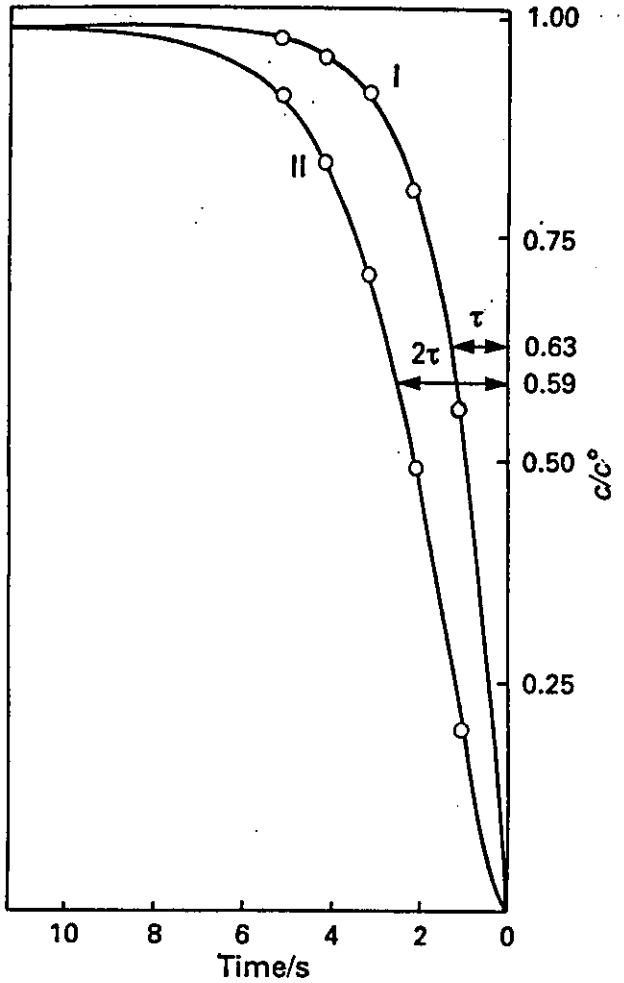

Fig. 3.13 *F*-curves obtained from the analogue to the EDT module. I, Without filter; II, with filter time constant $\tau = 1.2$ s in operation. The points shown were I, calculated from equation 1.2 and II, calculated from equation 3.25.

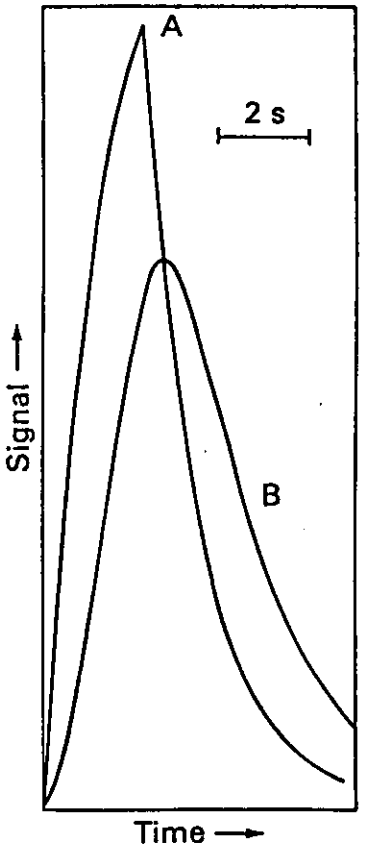

Fig. 3.14 Pulse signal ($\tau = 1.2$ s) through the EDT Model ECP100 polarograph. A, Without filtering; B, with filter time constant (1.2 s) in operation

using the 50 Hz mains frequency. A slow scan was used to establish the full-scale deflection and a fast scan was then employed to record the trace from which the experimental τ value was then interpolated from τ = 0.632 f.s.d. Theoretical time constant values from 2s to 0.1s were faithfully reproduced. Hence, at an RC value of 0.1s, τ was found to be 0.101 ± 0.002 s, based on five replicates.

These studies show that the filter time constant on the electrochemical module profoundly influences the response characteristics of the system, but when not employed no electronic distortion was discernible down to response times of at least 0.1s. Consequently, the filter circuit was not employed during data collection in this study.

3.3.4 Howe YT-1000 Recorder Response

3.3.4.1 Response time by the sine-wave method

Sine waves in the frequency range 5 to 0.4 Hz were registered on the Howe YT-1000 recorder at a chart speed of 10 mm s^{-1} and their amplitude measured. Representative traces are shown in Fig. 3.15 and a full set of data is shown plotted in Fig. 3.16. Reduced response is evident at frequencies in excess of 1.7 Hz as the pen fails to keep up with the varying voltage. From the curve and utilising equation 2.7, the response time of the recorder was estimated to be approximately 0.34s.

3.3.4.2 Response to flow analogue signal

FI pulses over a range of D_s values at τ values ranging from 4s to 0.25 s were generated from the RC analogue and recorded by the Howe recorder operated at the maximum chart speed of 10 mm s^{-1}.

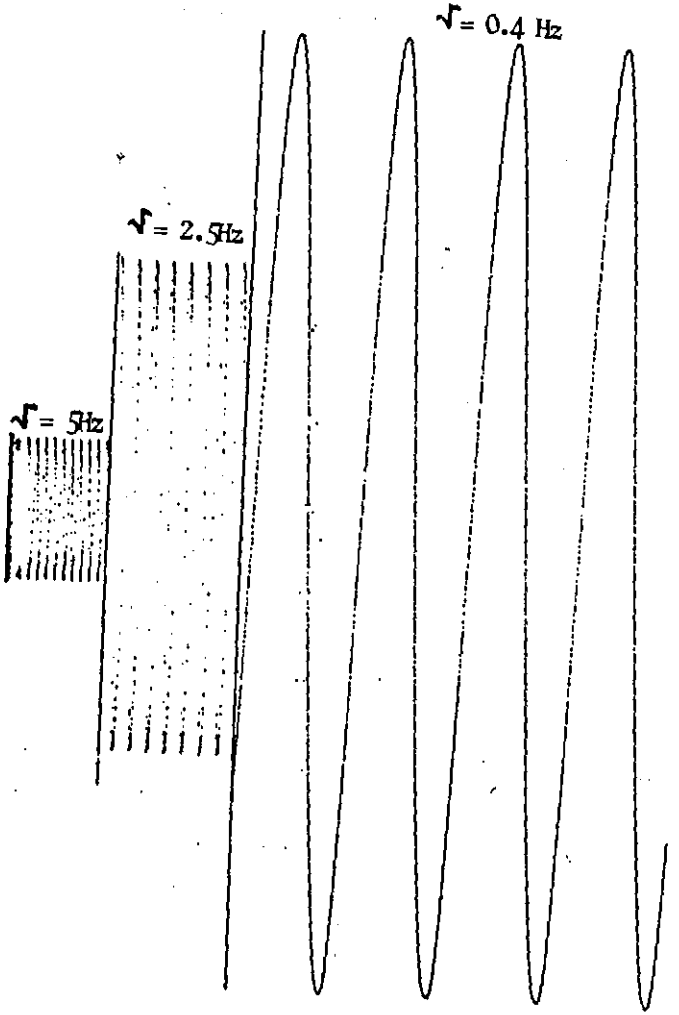

Fig. 3.15. Sine wave traces on Howe YT1000 recorder. Chart speed 10 mms^{-1}. Sine wave frequencies (√) as indicated.

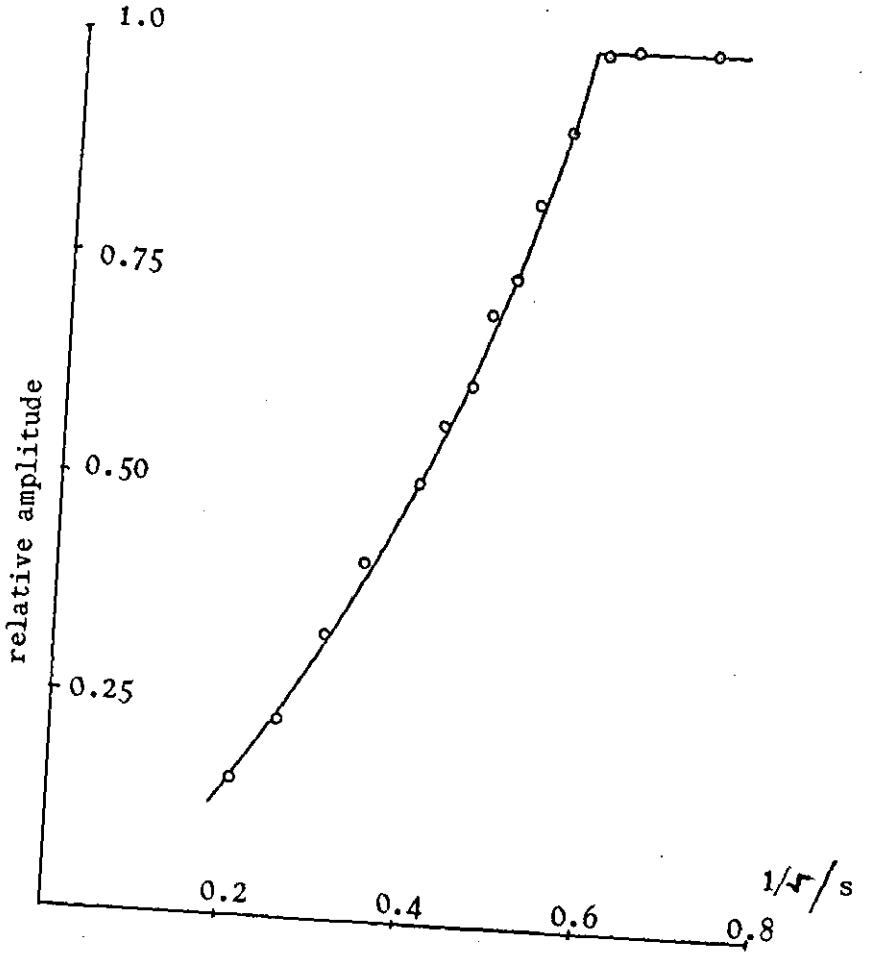

Fig. 3.16 Relative amplitude vs. 1/√

Measured values of D_s and Δt at f = 0.5 from the chart trace were compared with the selected dispersion value and with peak widths expected from equation 3.24.

Faithfully recorded values were obtained down to a τ value of approximately 1s. Thereafter, the response time of the pen was of the same order as the time constant of the transient signal and distortions in the peak parameters appeared and became progressively worse as the value of τ was reduced.

Hence it was anticipated that the Howe YT-1000 potentiometric recorder would prove inadequate in recording transport events having residence times within approximately three times its response time.

3.3.5 Recording Fast Transients

A chromatographic computing integrator (Trivector, Sandy Ltd) collecting data at rate of 40 ms per point was tested using FI analogue signals. The system has the attraction of possessing much signal processing capacity. However, below τ values of 1.5s the integrator displayed a systematic error of about 0.1s presumably due to additive coupling of the uncertainty in the data collecting rate when peak widths were calculated. Instead, the recording of transport events having short residence times was captured without inertia on a Telequipment 51B oscilloscope with photographic recording. The time base of this instrument was calibrated using the FI analogue circuit.

3.4 Dynamic Response of the Working Electrode Detector

In the classic dynamic response experiment discussed in Section 1.3.1, a step concentration input is aimed at the detector and the output response is monitored (Fig. 1.12). The delivery tube to the detector is usually short, in the belief that transmission line dispersion is thereby curtailed and plug flow conditions prevail (e.g. 73). However this assumption is questionable as true plug flow conditions are not easily achieved. In a unique study, the flow profile in such a delivery tube was established using microelectrodes made from individual carbon fibres and found to be parabolic (85). In would appear that the real choice in method design is between pure laminar flow, i.e. Taylor A conditions and flow with an element of diffusive mixing ultimately leading to Taylor B dispersion. Since the Taylor A regime is the more theoretically manageable option it should lead to results of less ambiguous interpretation. Thus the response experiment reported here was designed to favour this state.

Taylor A flow is realised by using the hydrodynamic criteria incorporated in Fig. 1.6 (49), viz.

dimensionless time parameter (t') $\leqslant 0.012$
Peclet Number (Pe) > 1000

In this case t' (Dt/a^2) and Pe (U_o/D) are evaluated from the diffusion coefficient (D) of the dispersing hexacyanoferrate (II) species viz. 0.6×10^{-5} cm^2 s^{-1} (164); the delivery tube radius (a) of 0.04 cm; U_o, the linear flow velocity at the centre of the presumed laminar flow; and t, the travel time in the tube of length 9.4 cm, evaluated from U_o. In this calculation, U_o is the variable. The stated conditions are fulfilled at volumetric flow rates in excess of about 0.4 ml min^{-1}. Consequently experiments were conducted at

flow rates between 0.44 and 1.98 ml min^{-1}. The upper limit ensured that the travel time in the delivery tube could be adequately measured by the pen recorder operated at its maximum chart speed of 10 mms^{-1}.

3.4.1 Measurement of the Appearance Time

The time of travel of the concentration step from its origin at the slider value to the electrode surface is the appearance time (t_A). This was read off the pen recorder trace as the interval between the time of injection, signalled by the external event marker actuated by the switching action on the valve, and the onset of detector response; as in Fig. 3.17.

3.4.2 Measurement of the Detector Response Time

The rise curve of the detector signal was faithfully captured by the oscilloscope whose time base was calibrated using a pulse from the FI analogue as in Fig. 3.18. The analogue dispersion, D_s, was set at 1.587 so that the time to analogue signal maximum was equal to the RC value, which was selected to give an adequate signal amplitude.

In general terms, the response of the detector to a unit impulse input is the E curve, this is related to the normalised response or F curve by:

$$E = \frac{dF}{dt} \qquad 3.27$$

The response time of the detector (τ_D) is usually defined as the first moment of the E curve (32):

$$\tau_D = \int_0^\infty t\, E\, dt \qquad 3.28$$

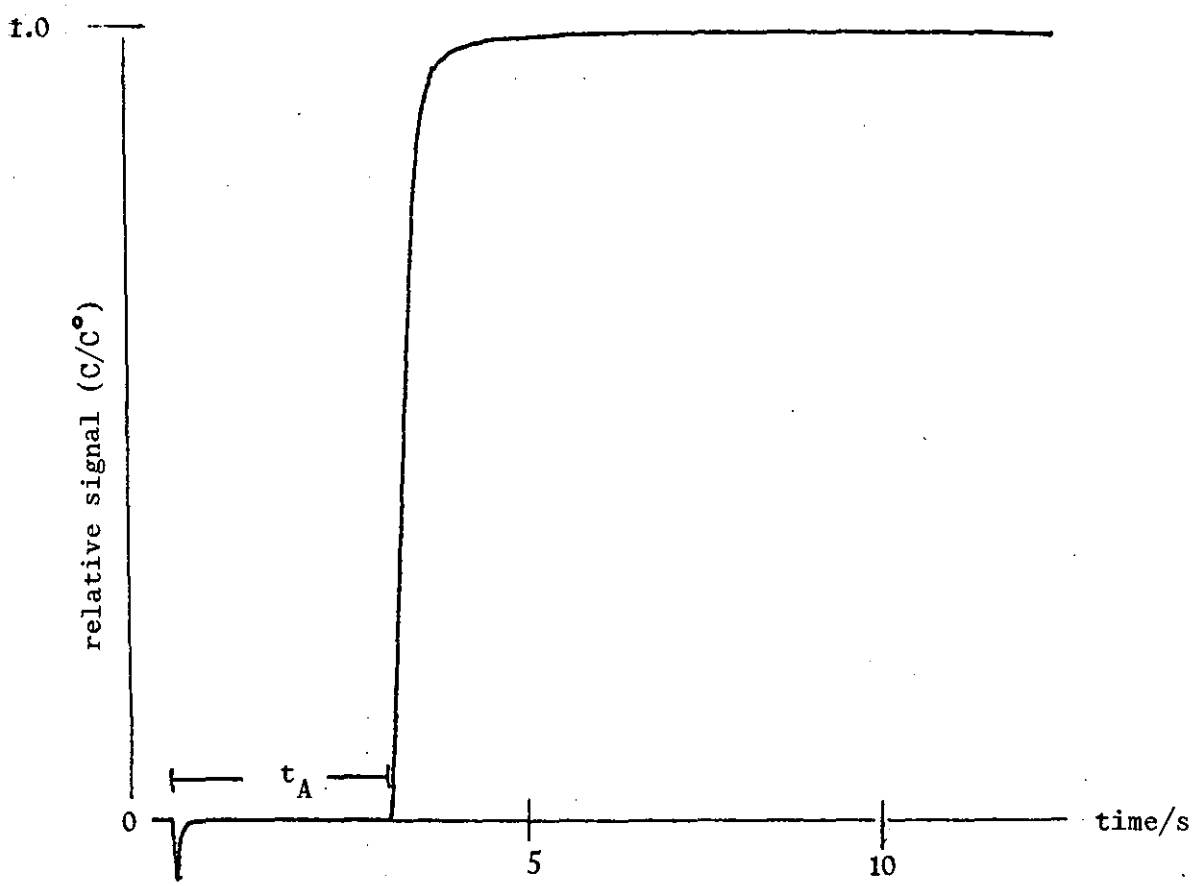

Fig. 3.17 Calculation of experimental appearance time (t_A), using Howe YT1000 pen recorder
V_f = 0.66 ml min^{-1}

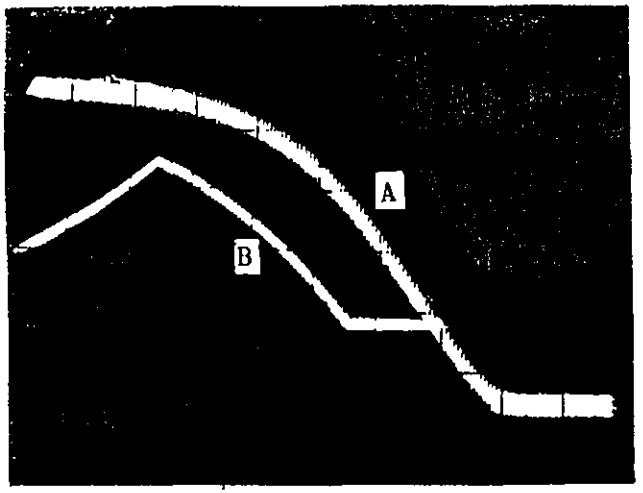

Fig. 3.18 Oscilloscope (Telequipment S51B) trace. A, Experimental curve at flow rate of 0.62 ml min^{-1}. B, Calibration signal from analogue, RC = 1s, peak maximum at 0.63 full-scale response, occurring at 1s.

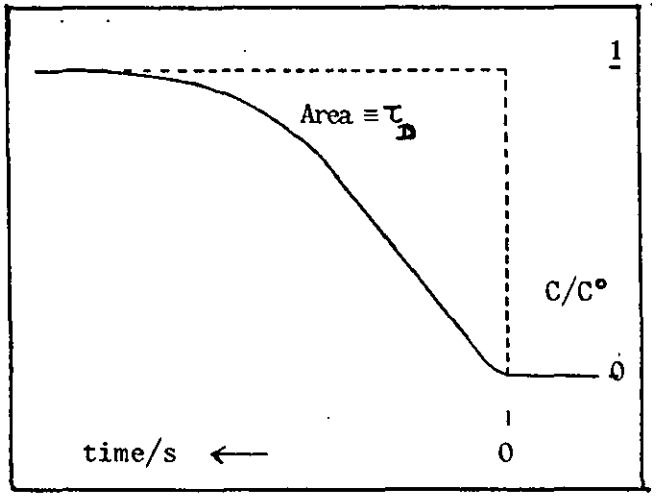

Fig. 3.19 Calculation of detector response time (τ_D) from response curve. Zero time indicated corresponds to a real time value of t_As. The indicated area defines $\int_0^\infty tdF$.

Experimental values obtained from oscilloscope traces.

Alternatively, τ_D can be evaluated from the F curve, since from equations 3.27 and 3.28, with the appropriate limits:

$$\tau_D = \int_0^1 t.dF \qquad 3.29$$

Thus τ_D can be evaluated from the normalised oscilloscope trace as the area indicated in Fig. 3.19.

In practice, the areas were determined by cutting out and weighing appropriate segments from the enlarged oscilloscope traces.

3.4.3 Results

Appearance time values are shown plotted as a function of the reciprocal volumetric flow rate in Fig. 3.20.

Each result was the mean of at least four replicates. There was good agreement between results obtained on different occasions after reassembling the flow line. Also plotted as guide lines are the appearance times expected for uniform plug flow occurring at the mean flow rate and for parabolic, laminar flow where the leading front proceeds at double the mean flow rate. In these calculations the total line volume used incorporated both the stainless steel delivery tube and the electrode channel, and for the given dimensions was 55 µl.

Response time values are also plotted in Fig. 3.20. The scatter observed may reflect a disturbance introduced on breaking and re-assembling the detector/delivery tube line on a day-to-day basis; a similar interpretation has been given to the variation in dispersion observed in a FIA line (63).

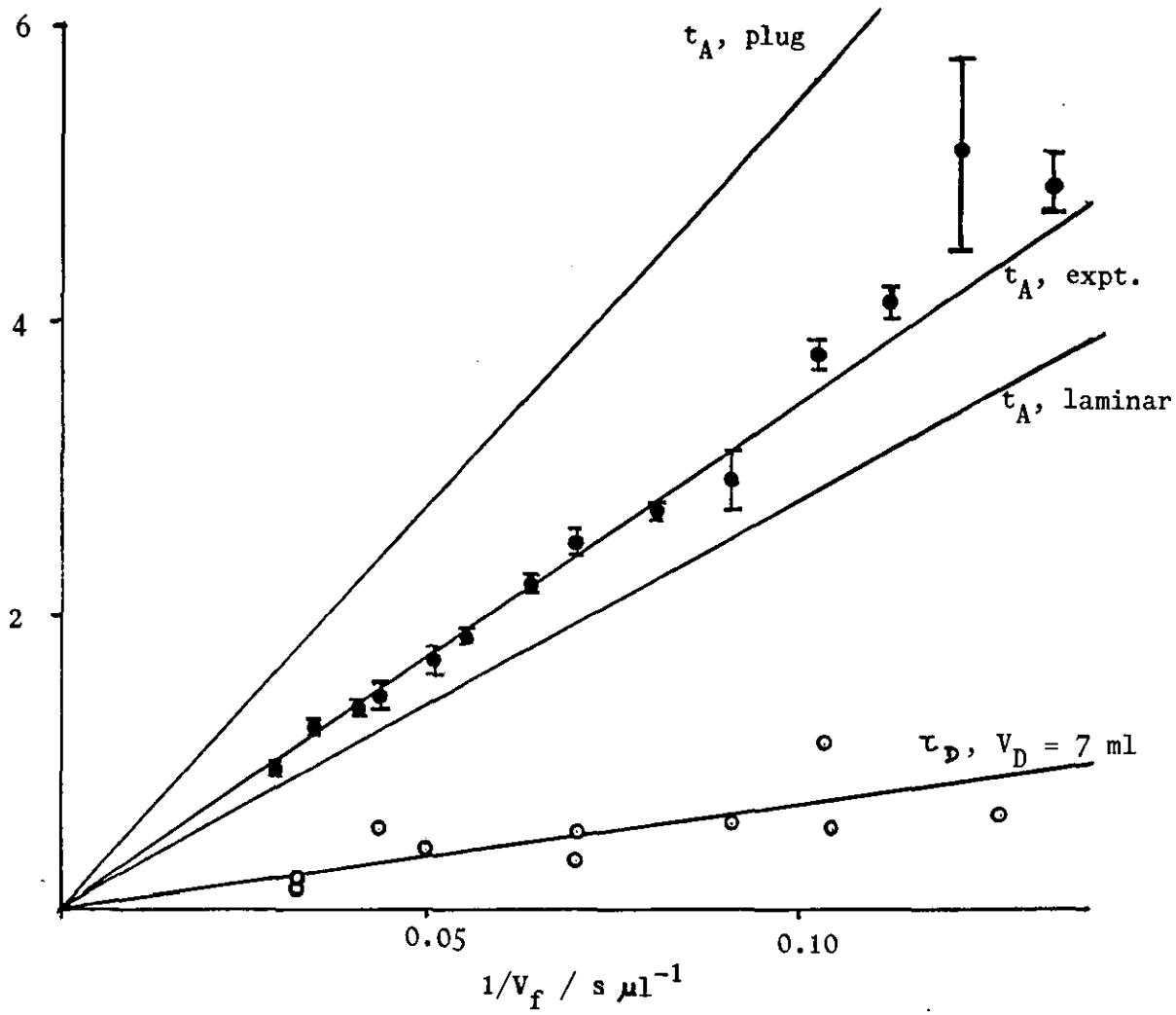

Fig. 3.20 Appearance times (t_A) and response times (τ_D) plotted vs. $1/V_f$. V_f is the flow rate in $\mu l s^{-1}$.
0 experimental response times.
● experimental appearance times.
Appearance times expected for plug and laminar flow also indicated.

The slope of the line through experimental τ_D values defines an effective detector volume (V_D):

$$\tau_D = \frac{V_D}{V_f} \qquad 3.30$$

A value of ca 7 µl is indicated for V_D.

3.4.4 Discussion

3.4.4.1 Appearance times

Vanderslice et al. (54) calculated appearance times in the region between Taylor A (pure convection) and Taylor B (pure diffusion) by numerical analysis. In the discussion of their complementary experimental results, they introduced an accommodation factor ϕ defined by equation 1.6

Adopting this parameter to this study which occurs in the Taylor A domain gives:

$$\phi = \frac{(t_A)\ \text{laminar}}{(t_A)\ \text{expt}} \qquad 3.31$$

This ratio can be calculated from the slopes of the relevant lines in Fig. 3.20 and is 0.81. Thus a strong element of near-laminar conditions probably prevail in the transmission line. This conclusion is given circumstantial support by the flow profile photograph taken in a dimensionally similar flow line to the stainless steel delivery tube (Fig. 3.21).

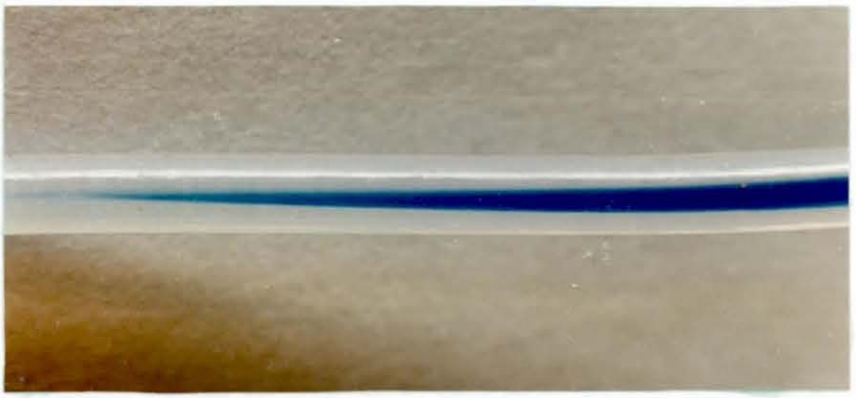

Fig. 3.21 Flow visualisation
Photograph of solute front on injecting a concentrated solution of bromocresol green in borax buffer into a borax carrier solution. Rheodyne 5020 injection value, sample loop = 0.5 ml, PTFE tubing, i.d. 0.8 mm.

Assuming laminar flow in the stainless steel delivery tube and plug flow in the electrode channel, the flow conditions during the experiment can be generated and are shown schematically in Fig. 3.22. The appearance times for pure laminar flow and for this mixed flow would then be given by:

$$(t_A)\ \text{laminar} = \frac{V_L + V_C}{2\ V_f} \qquad 3.32$$

$$\text{and } (t_A)\text{mixed} = \frac{V_L}{2V_f} + \frac{V_C}{V_f} \qquad 3.33$$

where V_L is the volume of the delivery line (47 µl) and V_C is the volume of the electrode channel (8 µl). These values define a theoretical factor given by:

$$\varphi' = \frac{(t_A)\text{laminar}}{(t_A)\text{mixed}} = \frac{V_L + V_C}{V_L + 2V_C} \qquad 3.34$$

which takes the value of 0.87. This agrees quite well with the experimental value.

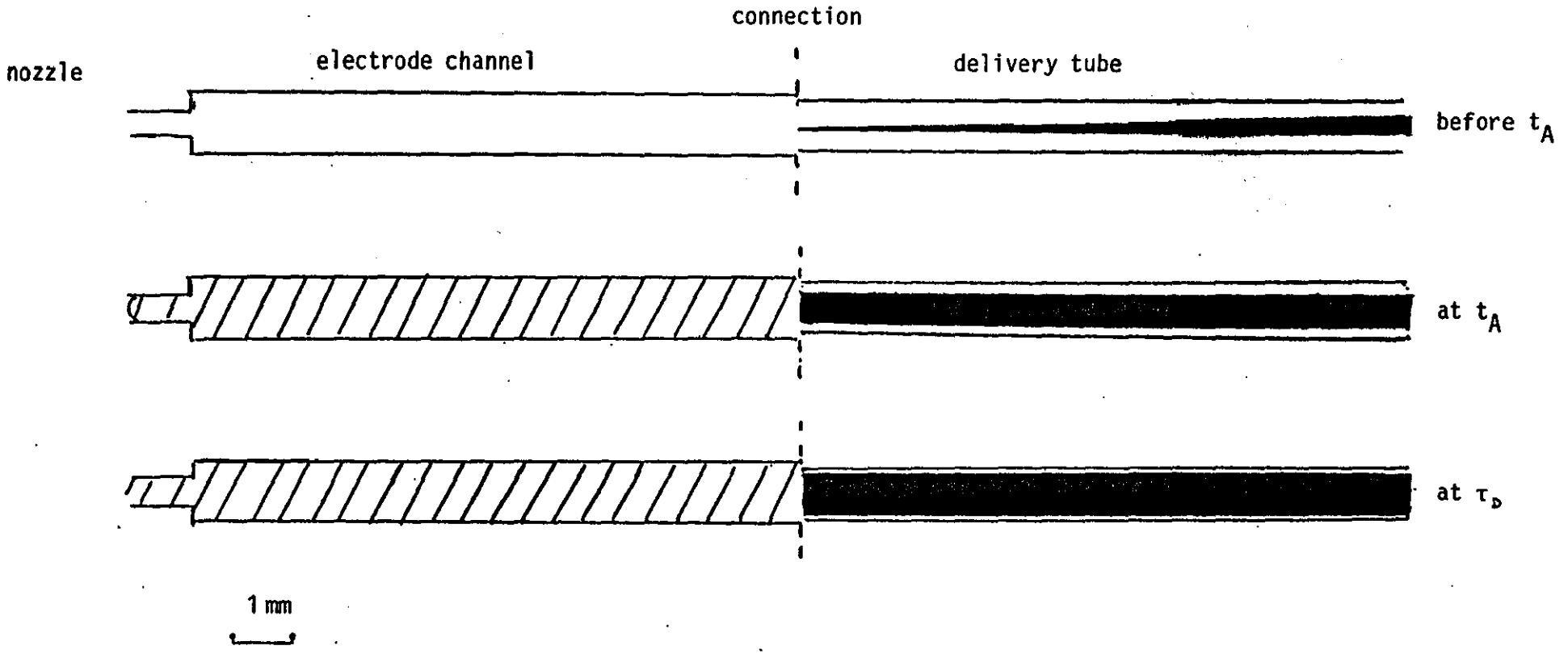

Fig. 3.22 Hypothetical flow model. Electrode channel and part of delivery tube drawn to scale. Laminar flow assumed in delivery tube, with plug flow accompanied by mixing in the electrode channel and nozzle. Laminar flow calculations based on V_f = 0.60 ml min^{-1} using parabolic flow profile equation, $U = U_o\ (1-r^2/a^2)$. U is the linear velocity.

Near plug flow in the electrode channel may be induced by turbulence arising from entry effects at the connection between detector and delivery line and at the narrow inlet to the electrode cavity.

3.4.4.2 Detector response volume

The rapid response of the detector defines a small effective detector volume of a ca. 7 μl. This value compares favourably with these reported for the structurally similar Metrohm EA/1096/2 wall-jet detector (79), and with the values of 5.3 and 4.0 μl for confined wall-jet configurations using GC and C paste electrodes respectively (84). However all these values are considerably less than that recorded at a C paste wall-jet assembly having the relatively large geometric volume of 80 μl (83).

3.4.4.3 Response curve form

Fig. 3.23 shows a pen recorder trace of an experimental response curve in comparison with those from four well defined theoretical cases:

I. Experimental response curve.

II. Plug flow with electrode process rate determining.

The jet from the detector nozzle strikes the electrode normally defining a stagnation zone of radius R_o = 0.021 cm. The flow then progresses at a mean radius r_m, given by:

$$r_m = \left(\frac{V_f t}{\pi b \, 60} \right)^{1/2} \quad , t = 0 \text{ at } t_A \qquad 3.35$$

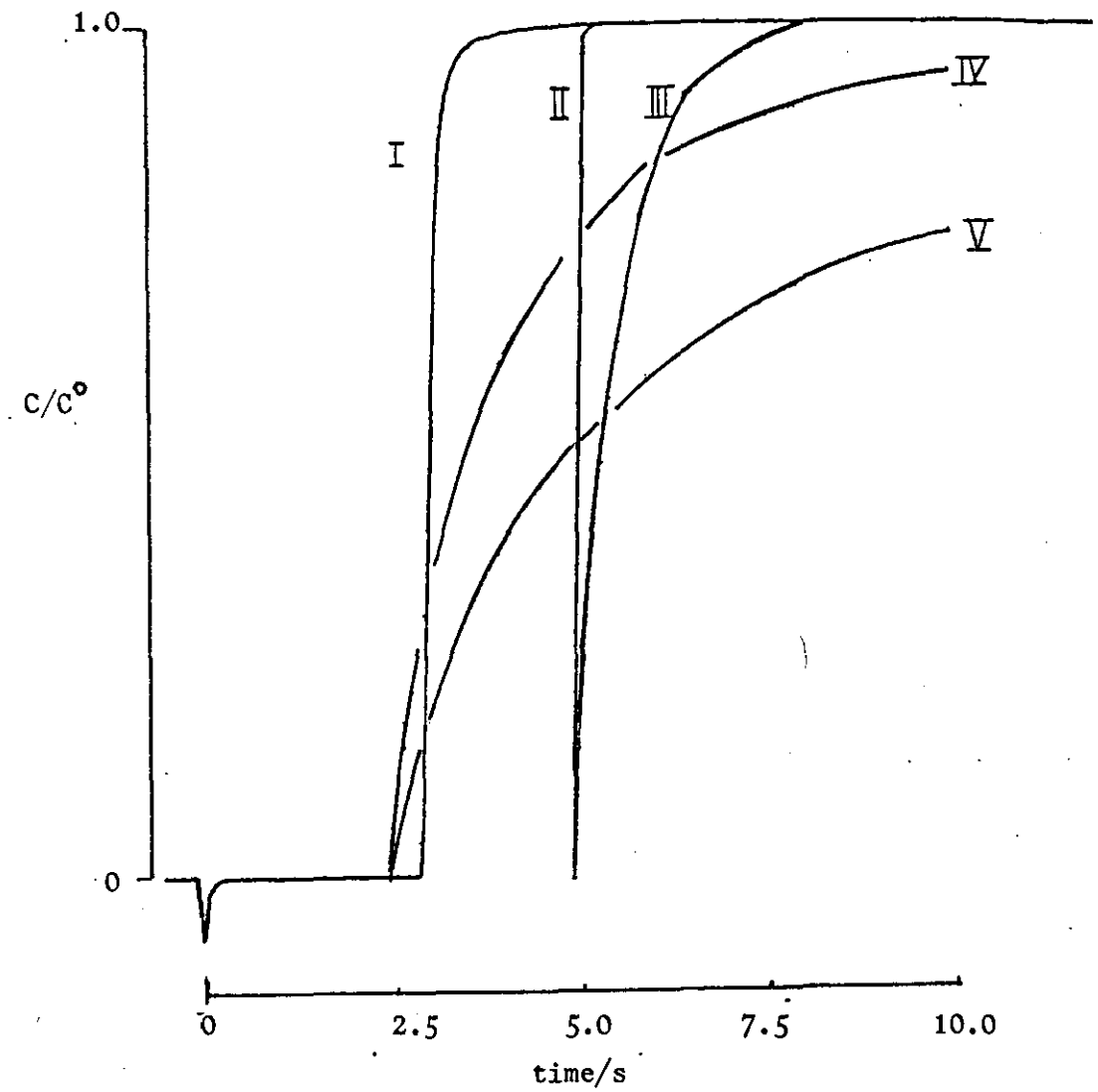

Fig. 3.23 Experimental (I) and theoretical (II-V) response curves. V_f = 0.66 ml min^{-1}, so for laminar flow t_A = 2.5s, and for plug flow t_A = 5.0s. II is plug flow with electrode response, equation 3.36. III is plug flow with exponential mixing; equation 1.1 with τ_p = 0.6s based on the mean V_D value of 7 µl. IV is laminar flow with mixed cup detection, equation 1.12. V is laminar flow with mean value detection, equation 1.13.

This expansion continues out to the electrode radius of 0.143 cm. V_f is the volumetric flow rate in ml min^{-1} and b is the chamber depth equal to 0.025 cm. Due to this shallow depth and low flow rate used the flow development is essentially parabolic, any wall-jet component is curtailed and may be neglected as a first approximation. The detector thus functions effectively as a stagnation/thin layer device with component currents given by equations 3.14 and 3.17. The total response being the sum of these components. The evolution from partially covered electrode to full covered electrode then defines the response curve, and with substitutions is given by:

$$\frac{C}{C^o} = \frac{1.72\ V_f^{1/2} + 224.7\ (r_m^2 - 4.41\times10^{-4})^{2/3}\ V_f^{1/3}}{1.72\ V_f^{1/3} + 16.56\ V_f^{1/3}} \qquad 3.36$$

r_m being obtained from equation 3.35.

This response is very rapid with a response time of the order of 0.1s for the 0.66 ml min^{-1} flow rate case.

III. Plug flow with exponential mixing

A mixing stage of residence time τ_p modifies a step input of concentration C^o. The response is given by equation 1.2 viz.

$$\frac{C}{C^o} = (1 - e^{-t/\tau_p}), \qquad t = 0 \text{ at } t_A$$

As noted in Section 1.3.1, this relation has often been used in amperometric response studies.

IV. Laminar flow with mixed cup detection

Small volumes of solute are completely mixed just prior to the sensing event. Combined with laminar flow this response is given by equation 1.12, viz.

$$\frac{C}{C^o} = 1 - \frac{t_A^2}{(t_A+t)^2} \quad , \qquad t = 0 \text{ at } t_A$$

With $\tau_D = t_A$

V. Laminar flow with mean value detection

The sensing element measures cross-sectional average concentration at right angles to the flow. This response is given by equation 1.13, viz.

$$\frac{C}{C^o} = 1 - \frac{t_A}{(t+t_A)} \quad , \qquad t = 0 \text{ at } t_A$$

With $\tau_D \longrightarrow \infty$

Examination of Fig. 3.23 reveals that although the experimental appearance time is close to the laminar flow value, the response is more rapid than expected from the extended dispersion accompanying pure laminar flow.

The relationship between the experimental and models II and III are better examined using the corresponding oscilloscope trace (Fig. 3.24). Datum points from this response are transposed to Fig. 3.25 where theoretical curves are also drawn. It is evident that the electrode response model II underestimates the response time indicating that some dispersion persists in the flow. However, the exponential mixer model provides a reasonable fit when the mean effective detector volume (V_D) of 7 µl is used to calculate τ_D as in IIIa. The fit can be improved by extending the mixing concept by

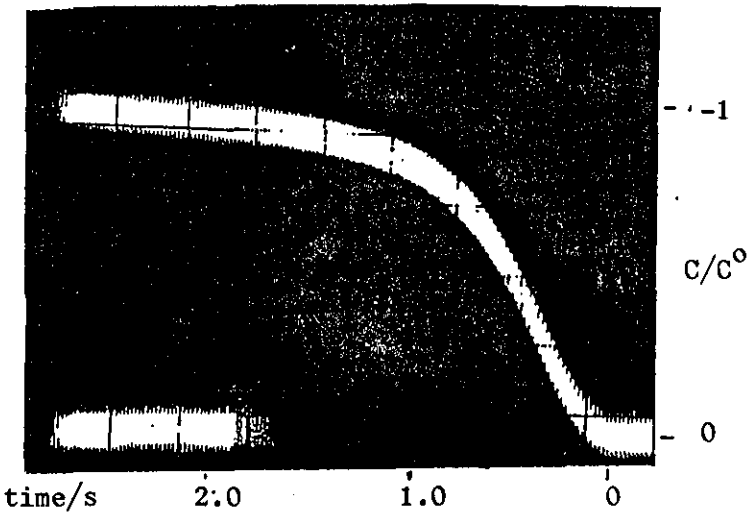

Fig. 3.24 Oscilloscope trace of response curve shown in Fig. 3.23I ie. with V_f = 0.66 ml min^{-1}

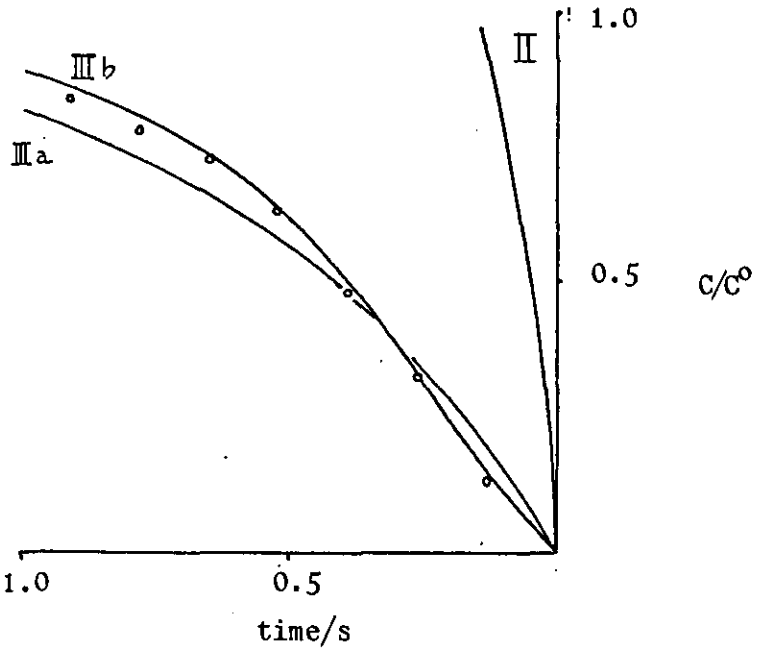

Fig. 3.25 Experimental and theoretical response curves for V_f = 0.66 ml min^{-1}. Circles represent experimental points interpolated from Fig. 3.24. II is the theoretic electrode response curve, equation 3.36. IIIa is the theoretical exponential mixing curve, equation 1.1 with τ_p = 0.6s based on the mean V_D value of 7 µl. IIIb is the theoretical exponential mixing curve, equation 3.37 with τ_p = 0.5s consisting of two components of ratio τ_{p1}/τ_{p2} = 4.

selecting a suitable τ_D and using a multi-parameter model of successive mixing stages. In this way the curve IIIB, which fits the experimental data well, was generated from a two tank model, with mixing stages of τ_{D1} = 0.4s and τ_{D2} = 0.1s using (73):

$$\frac{C}{C^o} = \frac{1}{(\tau_{D1} - \tau_{D2})}\left[\tau_{D1}(1-e^{-t/\tau_{D1}}) - \tau_{D2}(1-e^{-t/\tau_{D2}})\right] \quad 3.37$$

3.4.5 Conclusion

The classic dynamic response experiment has been critically examined and attention drawn to the state of flow in the delivery tube. Appearance time data suggested a degree of pre-mixing prior to contact with the electrode, and this was attributed primarily to the connection to the detector and to the narrowing of the channel at the jet-nozzle. As these are permanent features of the detector their contribution to the overall detector variance ($\sigma^2_{detector}$) are real. The response of the electrode was rapid with an effective volume of ca 7 µl, comparable to similar wall-jet electrodes. This value ensures that the device will not contribute significantly to signal distortion when used in flow analysis. As with other amperometric sensors (78,79,83,84), the response could be described by means of an exponential mixer model, although close examination indicated that a two-stage mixing model was preferable.

SECTION FOUR

FLOW TITRATIONS IN A VARIABLE VOLUME TANK REACTOR

EXPERIMENTAL

4.1 Tank Reactor and Flow Manifolds

The experiment was centred around a tank reactor with inlet and outlet flow, f_1 and f_2 respectively, as in Fig. 4.1. The tank reactor was a 30 ml PTFE vial containing a small magnetic stirrer bar situated above a rotating motor. Equal flow rates could be attained readily with a single pump using two channels with identical pump tubing as in Fig. 4.1a: this configuration was also used for unequal flows provided the relation required between f_1 and f_2 was not an exact multiple. In the latter case, balancing the flows in a single pump with different diameter pump tubing was tedious. This problem was circumvented either by using a dual exit line and three identical pump tubes as in Fig. 4.1b or by utilising the extra degree of freedom afforded by using a second pump as in Fig. 4.1c. The former configuration is the more economical. The pumps used were the multi-channel Ismatec Reglo/8, the multi-channel Ismatec Reglo/100 or the LKB 1200 Variopex as available.

The composition of the exit stream was monitored photometrically in a flow-through optical cell using a monochromatic light beam passing longitudinally through the 1 cm path length as in Fig. 1.11. The absorbance values were measured by a Tecator FIAstar 5023 spectrophotometer, the voltage outputs from which were stepped down by a x10 factor using the laboratory built op. amp. signal matching box for display on a Howe YT-1000 pen recorder, 100 mv full scale deflection.

The lines between inlet reservoir, reactor and detector were primed with the appropriate reagents before each run. Soft PVC tubing was used in the pumps and the rest of the line was 0.58 mm i.d. PTFE tubing. The line length between reactor and detector was minimised, so that the delivery volume was only 90 µl. Although the flow cell had a nominal optical path volume of just 18 µl, the total volume of the cell was found to be 168 µl by indirect measure with water.

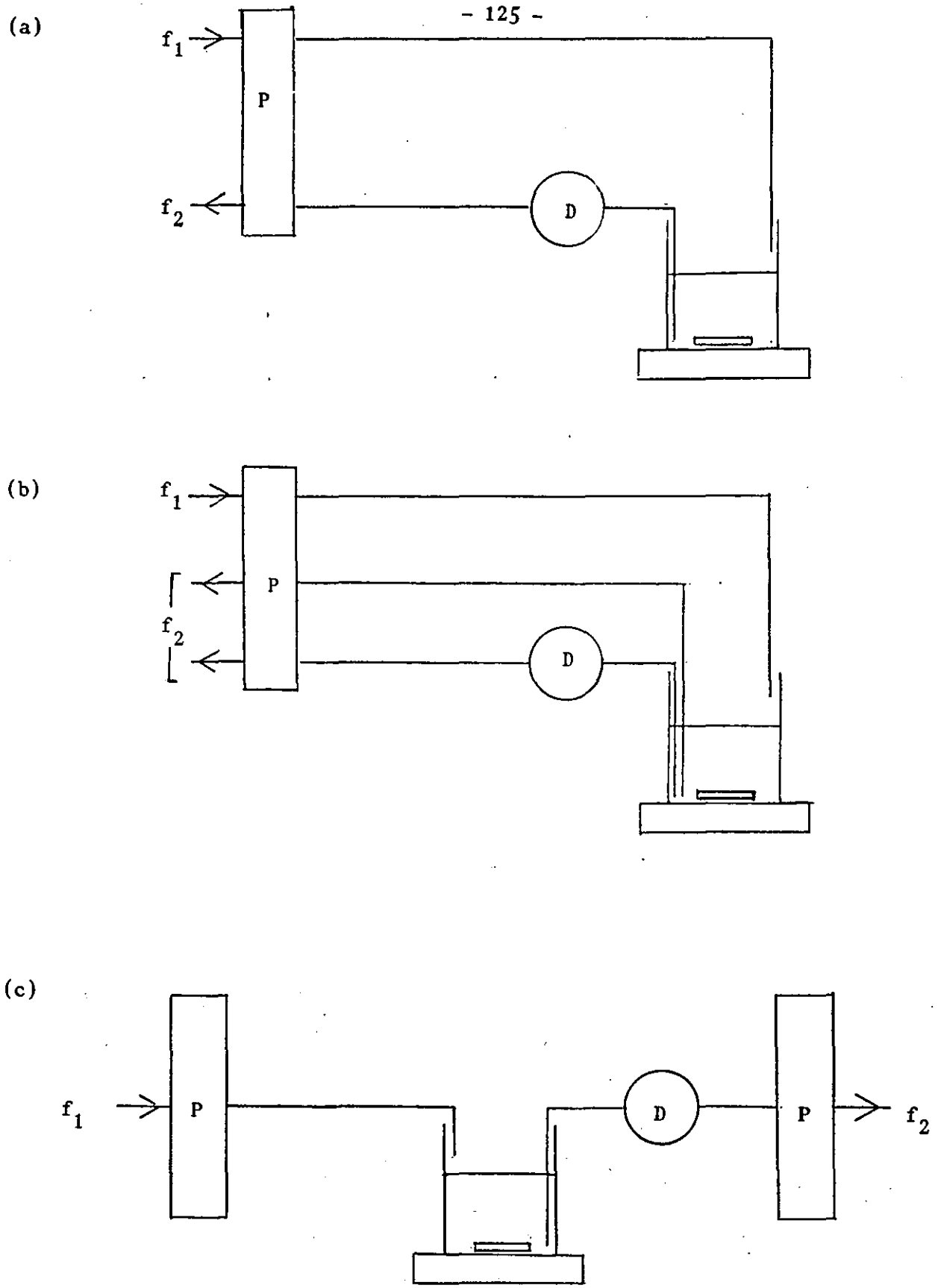

Fig. 4.1 Flow manifolds.
Pumps P, detector D.
(a) Single pump, single exit line manifold. (b) Single pump, double exit line manifold. (c) Two pump, single exit line manifold.

Because of the U-shape symmetrical design of the cell, its effective volume, comprising the entry limb and optical path, was estimated to be 93 µl. Thus the total external volume between tank and detector was 183 µl.

4.2 Concentration Gradients

(a) Solutions:
0.02 M di-sodium tetraborate
15.76 mg l^{-1} bromothymol blue in 0.02 M di-sodium tetraborate.

(b) Method:
The tank was charged with $V_o$ml buffer and bromothymol blue solution was delivered from a reservoir to produce F curves. By reversing the solutions, W curves were produced. Flow rates were measured volumetrically before and after a run. The 15.76 mg l^{-1} solution of the marker gave an absorbance of 0.915 at its λ_{max} of 611 nm; but, for display, initial, final and transient readings were converted into relative concentrations using Beer's law.

4.3 Appearance Time

The time taken for a slug of material to travel between the tank and the detector was measured directly by a stimulus-response experiment. The transmission line and detector, of total volume 183 µl, was primed with buffer solution and 10 ml. of the dye solution was placed in the tank reactor. On activating the pump and recorder event marker simultaneously, the appearance time (t_p) was read off the chart recorder operating at its maximum speed.

4.4 Flow Titrations

General Method:
$V_o$ml of analyte, of concentration C_A^o, was pipetted into the reactor. The exit line to the detector was also primed with this solution. Titrant, of concentration C_T^o, was delivered

at f_1 ml min^{-1} and the reaction mixture pumped out at f_2 ml min^{-1}. Within experimental error, f_2 was $2f_1$. These flow rates were measured volumetrically. The mean net flow out of the tank was taken as $1/2\ (f_1 + f_2/2)$ to calculate the emptying time. The titrations were followed by absorbance measurements at a suitable wavelength.

Each flow titration was duplicated by a batch photometric or visual titration which served as an internal standardisation. After correcting for dilution, the batch method rendered the C_T°/C_A° ratio for each titration.

The flow method was explored using a number of classic self-indicating photometric titrations.

4.4.1 Follow analyte titration of Fe(III)-salicylic acid by EDTA

Fe(III) forms a red complex with salicylic acid and a colourless complex with EDTA. Below pH 2.4, the latter complex is the more stable. Thus EDTA can be used to titrate Fe(III) in the presence of salicylic acid by monitoring the disappearance of the red colour photometrically (179).

Fe(III)-salicylic acid + EDTA $\longrightarrow$ Fe(III)-EDTA + Salicylic acid
(red)

Solutions

Stock 0.01M Fe(III)	Made by dissolving A.R. ammonium iron (III) sulphate in 0.01 M H_2SO_4
6% salicylic acid in acetone	

pH2 buffer	Made with 0.8 M acetic acid/ 0.2 M sodium acetate by adding conc. HCl to required pH. Sulphuric acid was unsuitable for this adjustment as the excessive sulphate subsequently discharged the red colour of the complex prematurely, presumably due to the formation of the relatively stable $FeSO_4^+$ species (180).
5×10^{-4}M Fe(III)-salicylic acid	10 ml. Fe(III) stock, 2 ml. salicylic acid reagent diluted to 200 ml. with pH2 buffer
EDTA solutions	A 0.1 M stock solution of the solution of the sodium salt of EDTA was used; this was diluted to strength as required. Low concentrations, below 2×10^{-3}M, were made up fresh in pH2 buffer to avoid possible rise in pH due to dilution on titration. However the free acid form of EDTA has limited water solubility and higher concentrations were made up in distilled water. The limited dilution reached in titrations with these stronger solutions had no measurable effect on the pH in the reactor.

Method

10 ml. of the 5 x 10^{-4} M Fe(III)-salicylic acid solution was titrated with a range of EDTA solutions at 530 nm. The initial absorbance was 0.75 but relative concentrations (C_A/C_A^o) calculated from Beer's law are displayed on the recorded titration curves. Comparative studies were made using both single pump and dual pump manifolds as in Figs. 4.1(b) and 4.1(c). Internal standardisation was carried out by batch photometric titration.

4.4.2 Follow Titrant. Titration of Fe(II) by Mn(VII)

The oxidation of Fe(II) by Mn(VII) affords a method of photometric titration followed by utilising the absorbance of the excess Mn(VII) titrant (181):

$$5Fe^{2+} + MnO_4^- + 8H^+ \longrightarrow 5Fe^{3+} + Mn^{2+} + 4H_2O$$
(coloured)

Solutions

0.02 M $KMnO_4$	Stock reagent
Fe(II) solutions	A stock solution of 0.08 M Fe(II) was made by dissolving A.R. ammonium iron (II) sulphate in 0.5 M H_2SO_4. This was diluted to the required strength by 0.5 M H_2SO_4

Method

10 ml. of the Fe(II) solution was titrated with 0.02M $KMnO_4$ solution, using the dual pump manifold, at 532 nm. The initiation of the titration was recorded on

the flow titration trace by using the recorder's event marker activated simultaneously with the start of the titration. Internal standardisation was carried out by batch visual titration.

4.4.3 Follow product

In self-indicating titrations where the product is monitored, the shape of the photometric titration curve is thermodynamically determined by the formation constant of the product, K_f. Two extreme situations of a weakly and strongly dissociated product were examined in this flow titration context.

4.4.3.1 Titration of Fe(III) by thiocyanate

At low concentrations, a 1:1 complex forms (182):

$$Fe^{3+} + SCN^- \rightleftharpoons \underset{(red)}{Fe\ SCN^{2+}}$$

However, this is a weak complex, with $K_f = 1.4 \times 10^2$ (183).

Solutions

1×10^{-3}M and 0.5 M $\times 10^{-3}$ M Fe(III)	As $Fe(NO_3)_3$ in 0.01M HNO_3
1×10^{-3} M and 5×10^{-3} M SCN^-	As KSCN in 0.015 M HCl

Method

5 ml. of Fe(III) was titrated with SCN^- solution in a dual pump manifold at 454 nm.

4.4.3.2 Titration of 2,4-dinitrophenol by hydroxide ion

Advantageous inductive and mesomeric effects stabilise the yellow phenolate anion relative to its conjugate acid, so that the latter can be titrated photometrically (184):

$$C_6H_3(NO_2)OH + OH^- \rightleftharpoons \underset{\text{(yellow)}}{C_6H_3(NO_2)_2O^-} + H_2O$$

$K_f = 4.7 \times 10^{11}$, based on a pKa for 2,4-dinitrophenol of 4.07 (185).

Solutions

0.1 and 0.01M NaOH	Standard solutions
Saturated 2,4-dinitrophenol	
Approx. 1×10^{-3}M 2,4-dinitrophenol	0.23 g of crystalline acid dissolved in 1 litre of water and filtered.

Method

Acid solution (10 ml.) was titrated with standard NaOH in a dual pump manifold. The product was monitored at 470 nm after first zeroing the spectrophomoter against distilled water. This wavelength is longer than λ_{max} for the product to counter the high molar extinction coefficient of the phenolate anion. Dilution of the sample at λ_{max} is not recommended as the hydrogen and hydroxyl ion concentrations would be modified by the dissociation of water (184). The flow titration was internally standardised by a batch photometric titration.

4.5 Physical Analogue of Linear Concentration Gradients

Linear voltage sweeps of $-5mvs^{-1}$ and $+ 10mvs^{-1}$ from a EDT Model ECP 100 polarograph module were recorded both with and without the low pass filter circuit, of time-constant 10s, in operation. The signals were displayed via a 1 MΩ dummy resistor and op. amp. signal matching box on a Howe YT-1000 potentiometric recorder.

SECTION FIVE

FLOW TITRATIONS IN A VARIABLE VOLUME TANK REACTOR
RESULTS AND DISCUSSION

5. Flow Titrations in a Variable Volume Tank Reactor

The concentration gradients existing within a tank reactor were first examined under a variety of flow conditions using a marker dye. Next, flow titrations using the reactor were performed in the manner described by Bound and Fleet (139). Photometric detection was employed, and the titration curves were rigorously examined theoretically.

5.1 Concentration Gradients in the Tank Reactor

Flow manifolds shown in Fig. 4.1 were used with the particular conditions as depicted in Fig. 5.1:

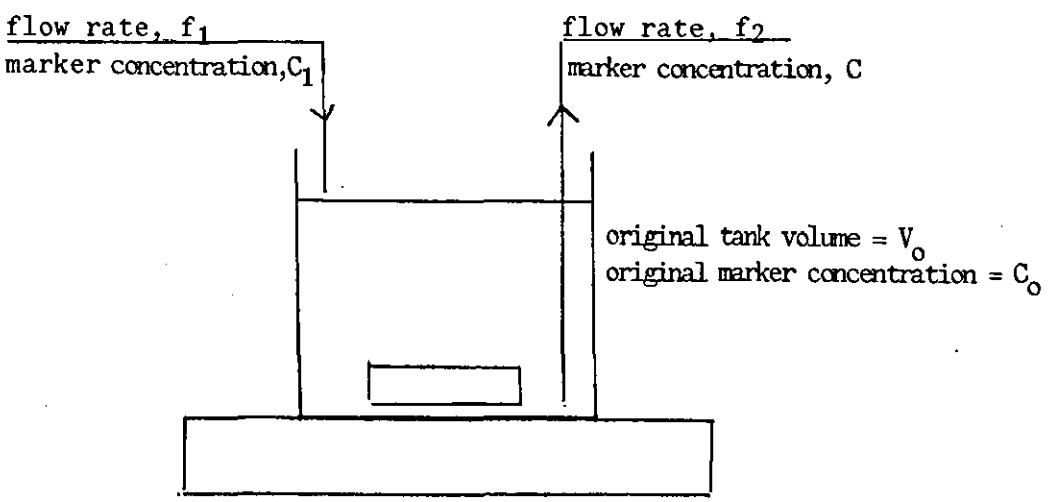

Fig. 5.1 Tank Reactor, Concentration Gradients Study

The reactor, originally containing solution at volume V_o, operates with constant inlet and outlet flows f_1 and f_2 respectively.

The volume in the tank at time t is:

$$V = V_o - (f_2 - f_1)\, t \qquad 5.1$$

Unless the flows are equal, this volume changes linearly with time. Concentration transients expected from this system can be described in terms of the dye marker bromothymol blue, originally present in the tank at a concentration C_o and solution volume V_o and fed at a rate f_1 from a reservoir at concentration C_1 producing a concentration C in the outlet stream. Assuming complete mixing in the tank, the appropriate differential equation based on the mass balance of marker is:

$$f_1C_1 = \frac{d(VC)}{dt} + f_2C \qquad 5.2$$

For the constant volume case ($f_1 = f_2 = f$), the solution is (61):

$$C = C_1 - (C_1 - C_o)e^{-ft/V_o} \qquad 5.3$$

and for the variable volume case, the solution is (132):

$$C = C_1 - (C_1 - C_o)\left\{1 - \left(\frac{f_2 - f_1}{V_o}\right)t\right\}^{f_1/(f_2-f_1)} \qquad 5.4$$

In the special case where $f_2 = 2f_1$, a linear concentration should be obtained, and has been demonstrated experimentally (186).

When $C_o = 0$, a concentration rise or F curve is obtained. when $C_1 = 0$ a wash or W curve is obtained. Under identical flow conditions, these curves are symmetrically related (187):

$$F + W = 1 \qquad 5.5$$

5.1.1 Results

(i) Constant Volume Reactor ($f_1 = f_2 = f$)

Flow manifold as in Fig. 4.1a
$C_o = 15.76$ mg l^{-1}
$C_1 = 0$
$V_o = 10$ ml
mean $f_1 = 1.50 \pm 0.02$ ml min^{-1}
mean $f_2 = 1.50 \pm 0.03$ ml min^{-1}
mean $V_o/f = 6.67 \pm 0.11$ min

V_o/f is a direct measure of the residence time in the reactor.

These conditions produce a W curve, which from equation 5.3, should be of the form:

$$C = C_o \, e^{-t/\tau} \qquad 5.6$$

The experimental curve is shown in Fig. 5.2a and when plotted in the linearised form as in Fig. 5.2b is seen to conform to equation 5.6 with a residence time (τ), calculated from the slope of the regression line, of 6.77 ± 0.04 min, which agrees well with the directly measured value above.

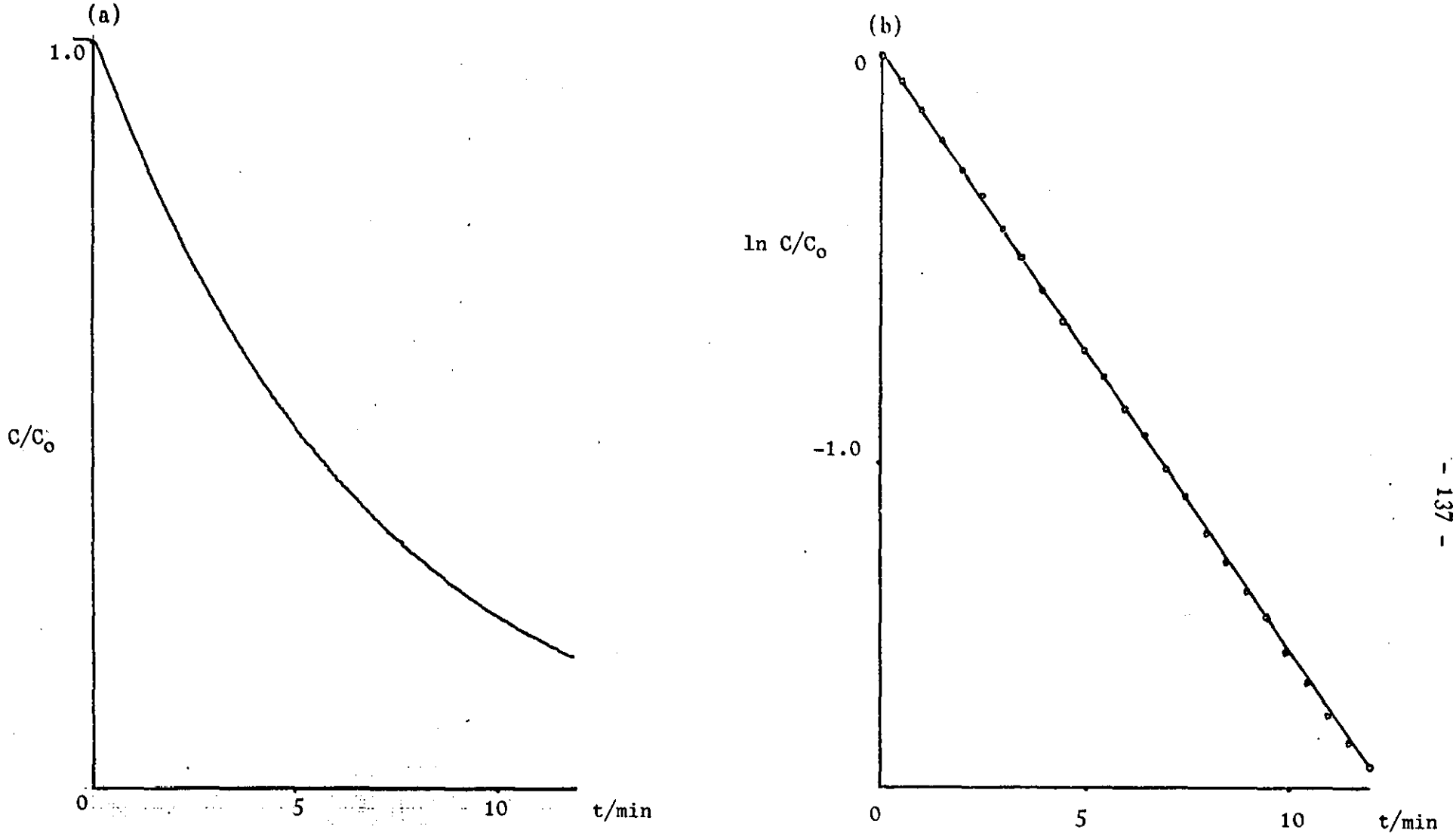

Fig. 5.2 Constant Volume tank reactor. V_o = 10 ml, Meat flow rate = 1.50 ± 0.025 ml min^{-1}, Experimental residence time = 6.67 ± 0.11 min. (a) C/C_o vs. t. (b) Linearised form of equation 5.6, ln C/C_o vs. t. Calculated residence time = 6.77 ± 0.04 min

(ii) Filling Tank Reactor ($f_1 > f_2$)

Flow manifold as in Fig. 4.1a
F and W curves were produced under identical flow conditions

	F curve	W curve
C_o/mg l^{-1}	0	15.76
C_1/mg l^{-1}	15.76	0
V_o/ml	5	5
mean f_1/ml min^{-1}	2.82	2.82
mean f_2/ml min^{-1}	1.23	1.23

Experimental results, together with theoretical values calculated from equation 5.4, are shown in Fig. 5.3a,b. It is noteworthy that F and W curves are superimposable by reflection and translation symmetry operations in accordance with equation 5.5, since flow conditions are identical.

(iii) Emptying Tank Reactor ($f_2 > 2f_1$, $f_2 < 2f_1$)

Flow manifold is in Fig. 4.1a.
Two F curves were produced corresponding to the conditions $f_2 < 2f_1$ and $f_2 > 2f_1$.

	F curve, $f_2 < 2f_1$	F curve, $f_2 > 2f_1$
C_o/mg l^{-1}	0	0
C_1/mg l^{-1}	15.76	15.76
V_o/ml	5	10
mean f_1/ml min^{-1}	1.05	0.92
mean f_2/ml min^{-1}	1.85	3.51

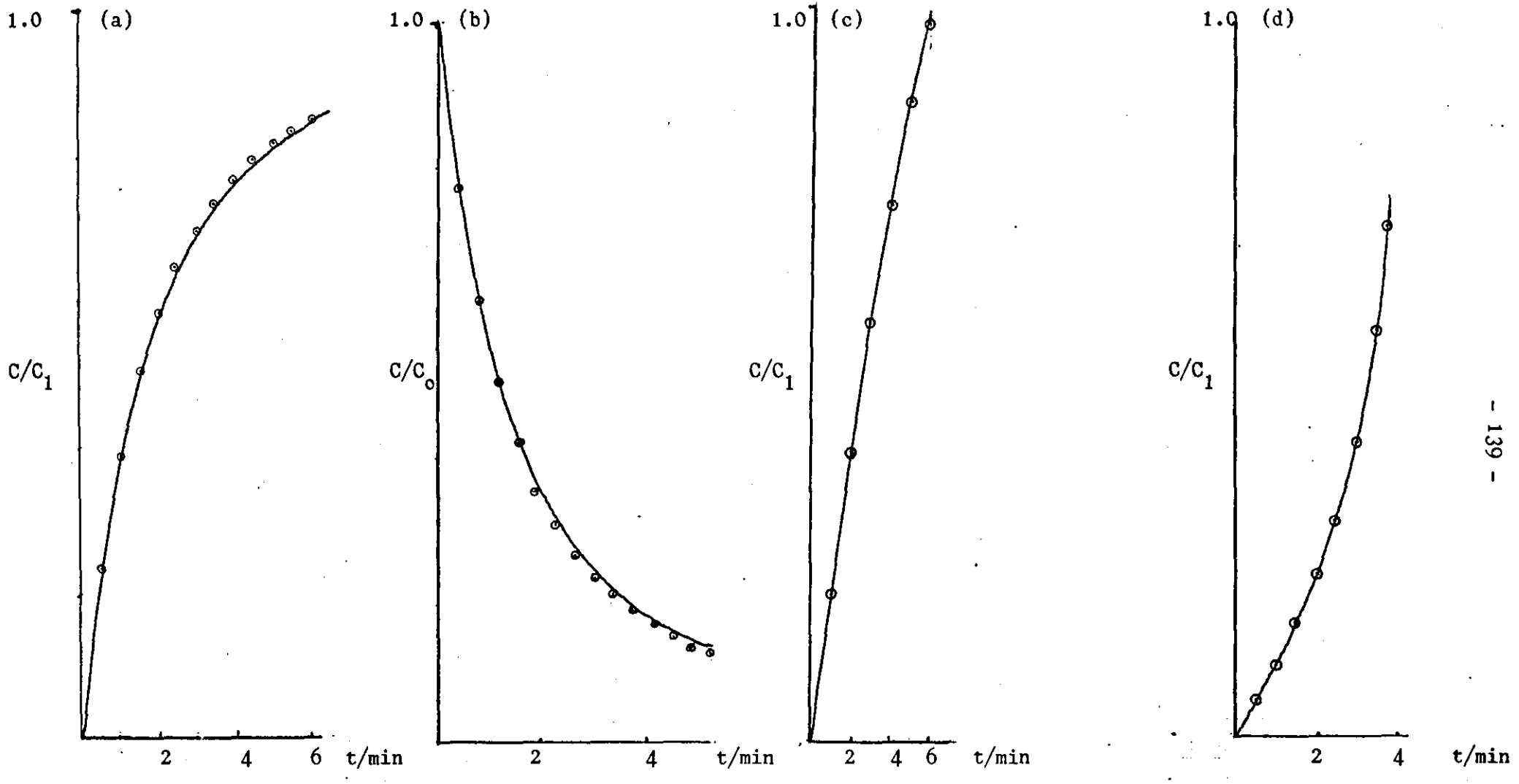

Fig. 5.3 Non-linear concentration gradients.
Filling tank: V_o = 5 ml, f_1 = 2.82 ml min^{-1}, f_2 = 1.23 ml min^{-1}. (a) F Curve. (b) W Curve.
Emptying tank F curves: (c) V_o = 5 ml, f_1 = 1.05 ml min^{-1}, f_2 = 1.85 ml min^{-1}
(d) V_o = 10 ml, f_1 = 0.92 ml min^{-1}, f_2 = 3.51 ml min^{-1}. Experimental results full line, circles represent points calculated from equation 5.4.

In accordance with equation 5.4, a convex curve is produced when $f_2 < 2f_1$ and a concave curve is produced when $f_2 > 2f_1$, as shown in Fig. 5.3c,d.

(iv) Emptying Tank Reactor ($f_2 = 2f_1$)

Two pump, single exit line manifold as in Fig. 4.1c. F and W curves were produced under different flow conditions.

	F curve	W curve
C_o/mg l^{-1}	0	15.76
C_1/mg l^{-1}	15.76	0
V_o/ml	5	5
mean f_1/ml min^{-1}	0.99	0.85
mean f_2/ml min^{-1}	2.00	1.66

As expected from equation 5.4, linear gradients are obtained under these conditions extending over most of the period whilst the tank is emptying, as depicted in Fig. 5.4.

Further results with this manifold are shown later in Table 5.1, together with a similar set obtained with twin exit line manifold of Fig. 4.1b for comparison.

5.1.2 Discussion

The coincidence of measured and calculated residence times in the constant volume mode of operation is indicative of perfect mixing of fluid elements at the macroscopic level in the tank. Such a situation is to be expected when the residence time greatly exceeds the circulation time (61). The absence of fluctuations is also indicative of satisfactory micro-mixing at the molecular diffusion level (188).

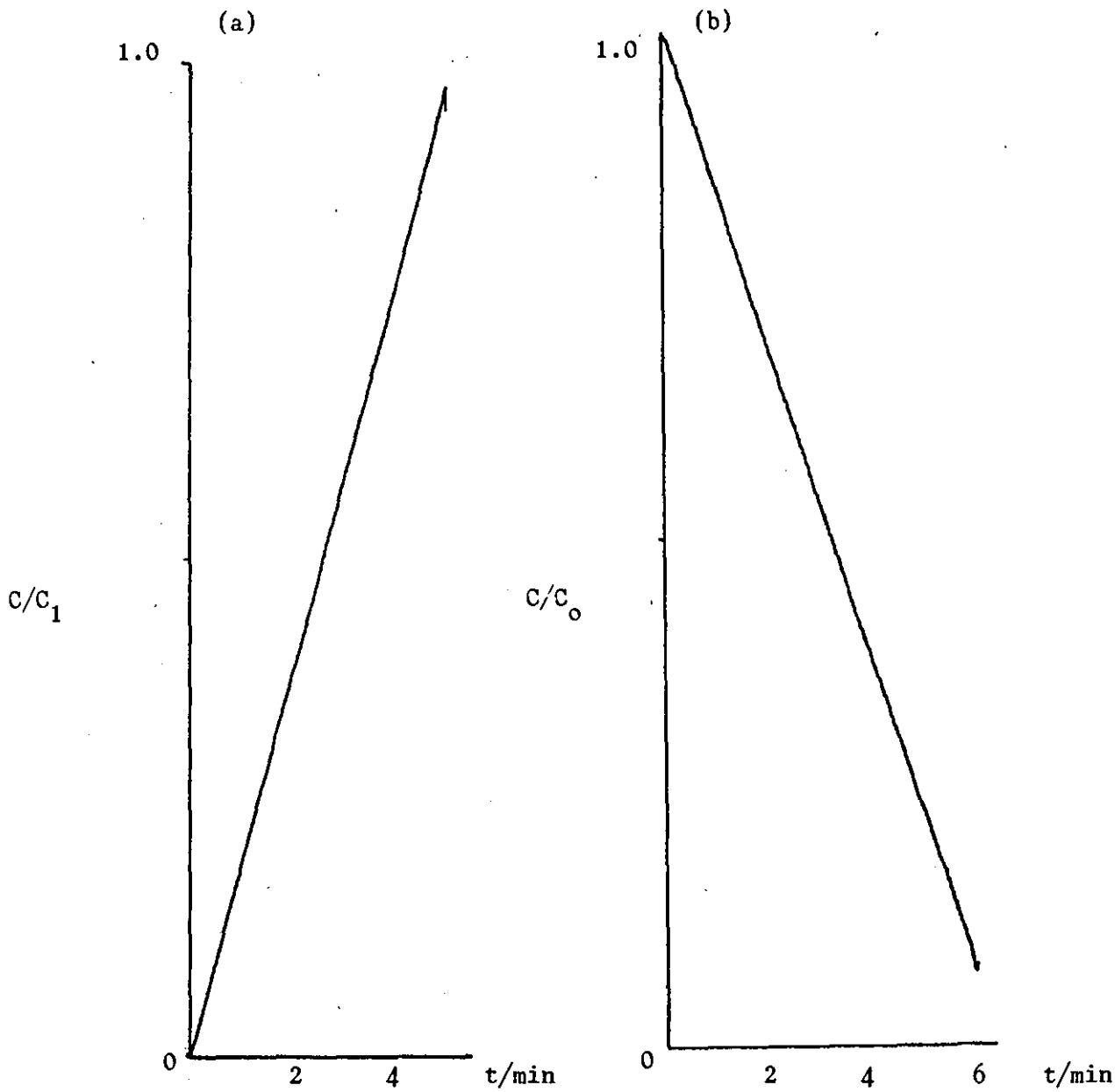

Fig. 5.4 Linear concentration gradients. (a) F curve. V_o = 5ml, mean emptying rate $(f_2 - f_1)$ = 1.01 ml min^{-1}, slope = 0.202 min^{-1}. (b) W curve. V_o = 5ml, mean emptying rate $(f_2 - f_1)$ = 0.81 ml min^{-1}, slope = 0.160 min^{-1}.

The satisfactory result also suggests that under these conditions any dispersion in the short reactor-detector line does not contribute significantly to the overall process (189).

The traces obtained with the variable volume tank reactor shown in Fig. 5.3 afford experimental confirmation of the Sorin relation, equation 5.4. Any residual error is probably attributable to the imprecision in the flow rates when using peristaltic pumping.

In the production of linear gradients, $f_2 = 2f_1$, so equation 5.4 can be written:

W curve $$C/C_o = 1 - (\underline{f_2 - f_1})t \qquad 5.7$$
$$V_o$$

F curve $$C/C_1 = (\underline{f_2 - f_1})t \qquad 5.8$$
$$V_o$$

The gradients are thus characterised by the function $|(f_2-f_1)/V_o|$ min^{-1}.

The relative standard deviation of the flow rate delivered by a peristaltic pump was carefully measured over a 2 hour period and found to be not greater than 2 per cent. The relative standard error in the measured flows of paired values taken before and after a run using single entry and exit lines would them be expected to be 2.8 per cent at the 95 per cent confidence level. These errors would then combine in the linear slope function $|(f_2-f_1)/V_o|$ to produce an uncertainty of approximately 4 per cent (190). This estimate was confirmed by a simulation using $f_1 = 1.00 \pm 0.02$ ml min^{-1} and $f_2 = 2.00 \pm 0.02$ ml min^{-1} with $V_o = 5$ ml. in equation 5.8.

Computation was carried out to within 10 per cent of the tank emptying time. Straight lines were generated with a poorest correlation coefficient of 0.9996 and a range of slopes within 0.200 ± 0.008 min^{-1}. Of course, using the three line configuration of Fig. 4.1b, this uncertainty is greater and a parallel calculation to that above indicates a 5 per cent variability in the linear slope function. Using these error estimates, experimental and theoretical slopes can be compared as in Table 5.1

Table 5.1 Comparison of Theoretical and Linear Gradients

(a) Two line manifold as in Fig. 4.1c

Curve	V_o/ml	(f_2-f_1)/ ml min^{-1}	$(f_2/f_1)/V_o$ / min^{-1}	Exptal. slope/min^{-1}
F	5	1.00	0.200±0.008	0.200
F	5	1.01	0.202±0.008	0.202
W	5	1.00	-0.200±0.008	-0.194
W	5	0.81	-0.162±0.007	-0.160

(b) Three line manifold as in Fig. 4.1b

Curve	V_o/ml	(f_2-f_1)/ ml min^{-1}	$(f_2-f_1)/V_o$ / min^{-1}	Exptal. slope/min^{-1}
F	5	1.03	0.206±0.010	0.211
F	5	1.06	0.212±0.010	0.218
F	5	0.76	0.152±0.008	0.151
F	5	1.98	0.396±0.020	0.409

Thus experimental and theoretical results are concordant.

In conclusion, the tank reactor described here functions in a predictable manner and, in particular, can be used to produce linear gradients using a single or dual pump system with a precision limited by the variability of the flow rates.

For later convenience, the linear gradient relations in equations 5.7 and 5.8 are expressed in the form:

F curve, relative concentration $(C/C^o) = t/m$ 5.9

W curve, relative concentration $(C/C^o) = 1-t/m$ 5.10

where C^o represents the undiluted concentration, and m is $V_o/(f_2-f_1)$, the tank emptying time.

5.1.3 Transportation Lag and Dispersion

With the detector placed external to the reactor, two inherent distortion effects are anticipated. Firstly, there will be a transportation lag between the mixing event in the reactor and its detection; and secondly, dispersion will occur in the line-detector system.

The transportation lag was measured directly as the appearance time (t_p) of the signal from a stimulus-response experiment using the travel of a dye slug through the transmission line.

At a mean flow rate of 1 ml min^{-1}, t_p was 6.9 ± 0.1 s based on four replicate runs. On increasing the mean flow rate to 2 ml min^{-1}, t_p was not reduced commensurately but rather was 4.3 ± 0.2 s based on nine replicates.

In view of the complex hydrodynamic conditions existing in the system, due to the pulsed motion and diameter changes between the narrow feed line and the wider cell channel, this flow may be treated, semi-empirically, by a fractional turbularity model (191). In this, the flow is regarded as having a plug component of effective volume V_p and a mixing stage component, to allow for some dispersion, of effective volume V_s:

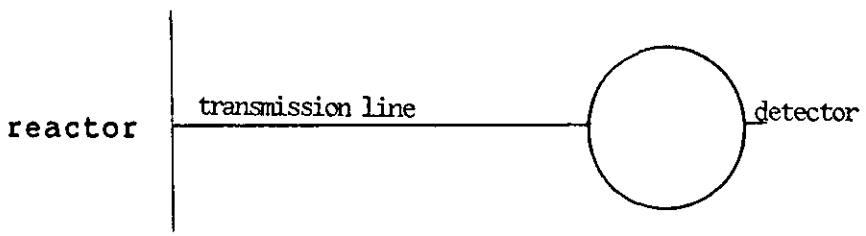

(a) actual line-detector system, total volume = 183ul

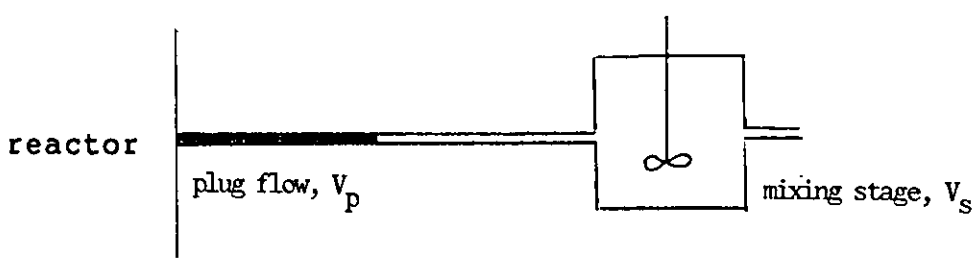

(b) model, total volume = 183µl

Fig. 5.5 Actual flow system and its fractional tubularity model

When the mean flow rate is 2 ml min^{-1}, V_p(= t_p x mean flow rate) is estimated to be 143 µl and hence V_s is 40 µl. But at 1 ml min^{-1} there is an apparent increase in dispersion and V_s rises to 68 µl.

Any linearly increasing concentration from the tank reactor, having a limit C^o, produces a ramp input into the transmission line system of the form:

$$C_{in}/C^o = At$$

where A is a proportionality constant.
The dispersed output C_{out} produced by the model may be obtained by the convolution of this input with the unit mixing stage response described by:

$$1/\tau_s \ (e^{-t/\tau_s})$$

τ_s (= $^{Vs}/f$) being the residence time in the mixing stage of volume V_s at a flow rate f. Thus:

$$\frac{C_{out}}{C^o} = I(t) \ * \ E(t) \qquad 5.11$$

I(t) is the input function = At
E(t) is the unit impulse response function = $1/\tau_s . e^{-t/\tau_s}$
Introducing t' as a dummy time variable, with real time t becoming parametric, equation 5.11 can be written in the form (192):

$$\frac{C_{out}}{C^o} = \int_o^t I(t') \ E \ (t-t') \ dt' \qquad 5.12$$

or explicity,

$$\frac{C_{out}}{C^o} = \frac{Ae^{-t/\tau_s}}{\tau_s} \int_o^t t' \ e^{t'/\tau_s} \ dt' \qquad 5.13$$

On integration,

$$\frac{C_{out}}{C^o} = A \ [t - \tau_s \ (1 - e^{-t/\tau_s})] \qquad 5.14$$

This dispersion modified F curve is a well known dynamic response relation in process control theory (193).

The complementary W curve, responding to the decreasing ramp input $C_{in}/C^o = 1 - At$, is readily obtained from equation 5.5, and is:

$$\frac{C_{out}}{C^o} = 1 - A\,[t - \tau_s\,(1 - e^{-t/\tau_s})] \qquad 5.15$$

In relations 5.14 and 5.15, the second term in brackets describes the effect of dispersion. It may be noted that at sufficiently long run times (t), the slope displays the undistorted value A.

For linear gradients produced from the variable volume tank reactor, the constant A is identical with the term 1/m as is apparent from the equations 5.9 and 5.10.

The full fractional tubularity model can be evaluated at a flow rate of 2 ml min^{-1} and using 300 s as a typical value for m, by taking t_p as 4.3s and evaluating the dispersion effects from equations 5.14 and 5.15 assuming V_s to be 40 µl, i.e. τ_s is 1.2 s.

The result is shown plotted in Fig. 5.6 and the insets demonstrate that the response is subject to transportation and dispersive lags of t_p and τ_s respectively, acting additively. The full F and W lines in this diagram, which simulate the actual gradients reported earlier, are hardly affected however; since time is measured from the onset of the concentration rise or fall and the initial curvature is negligible in the context of the long duration of the experiment. However, these transportation and dispersion effects may assume significance in applications in flow titrations where experimental transition times are shorter and the initial time position may not be self-indicating.

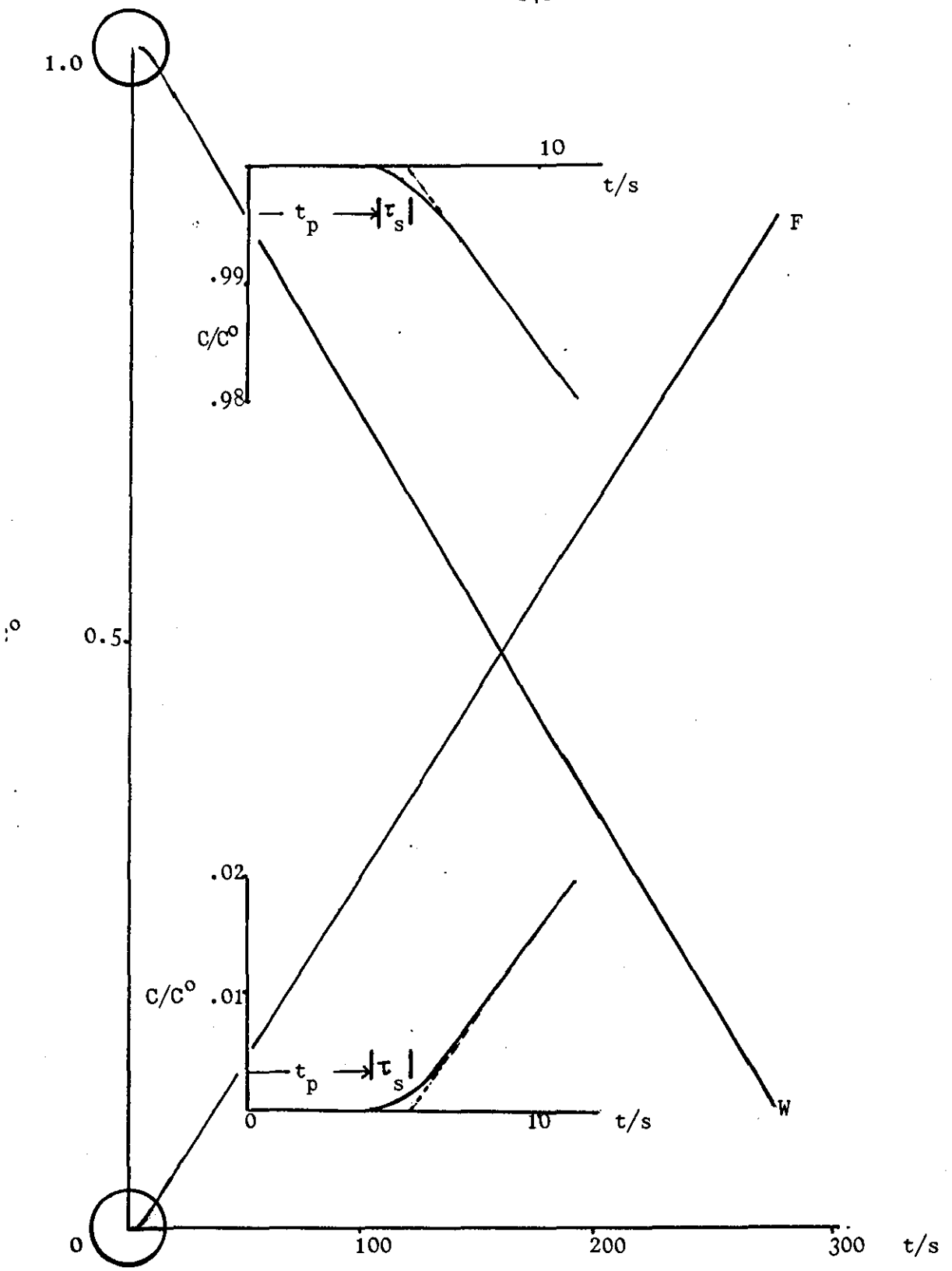

Fig. 5.6 Effect of fractional tublarity model for detection on linear concentration gradient. Emptying time (m) = 300s, t_p = 4.3s, τ_s = 1.2s. F curve constructed from equation 5.14. W curve constructed from equation 5.15. Insets are enlarged versions of circled regions.

5.2 Flow Titrations

Since, in a well mixed reactor, the concentration gradients described in the previous section exist within the tank; then it is possible to titrate a batch of analyte by a flowing titrant scheme, as in Fig. 5.7.

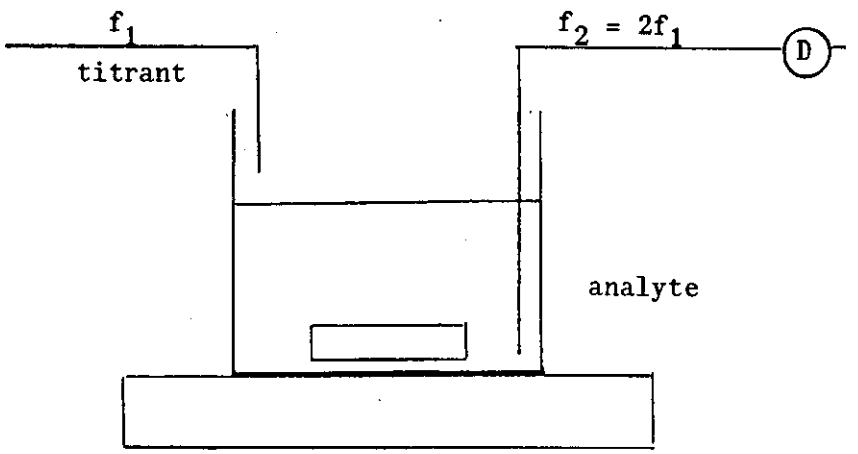

Fig. 5.7 Tank Reactor Flow Titration using Linear Concentration Gradients

The technique was used by Bound and Fleet to titrate chloride ion potentiometrically (139). Here a full theoretical exposition of the method is given for the 1:1 reaction between analyte (A) and titrant (T) to produce product (P):

$$A + T \longrightarrow P$$

The reaction is assumed to be thermodynamically complete and to occur at a rate infinitely faster than the residence time. Intuitively, the concentration gradients expected during the titration are shown in Fig. 5.8.

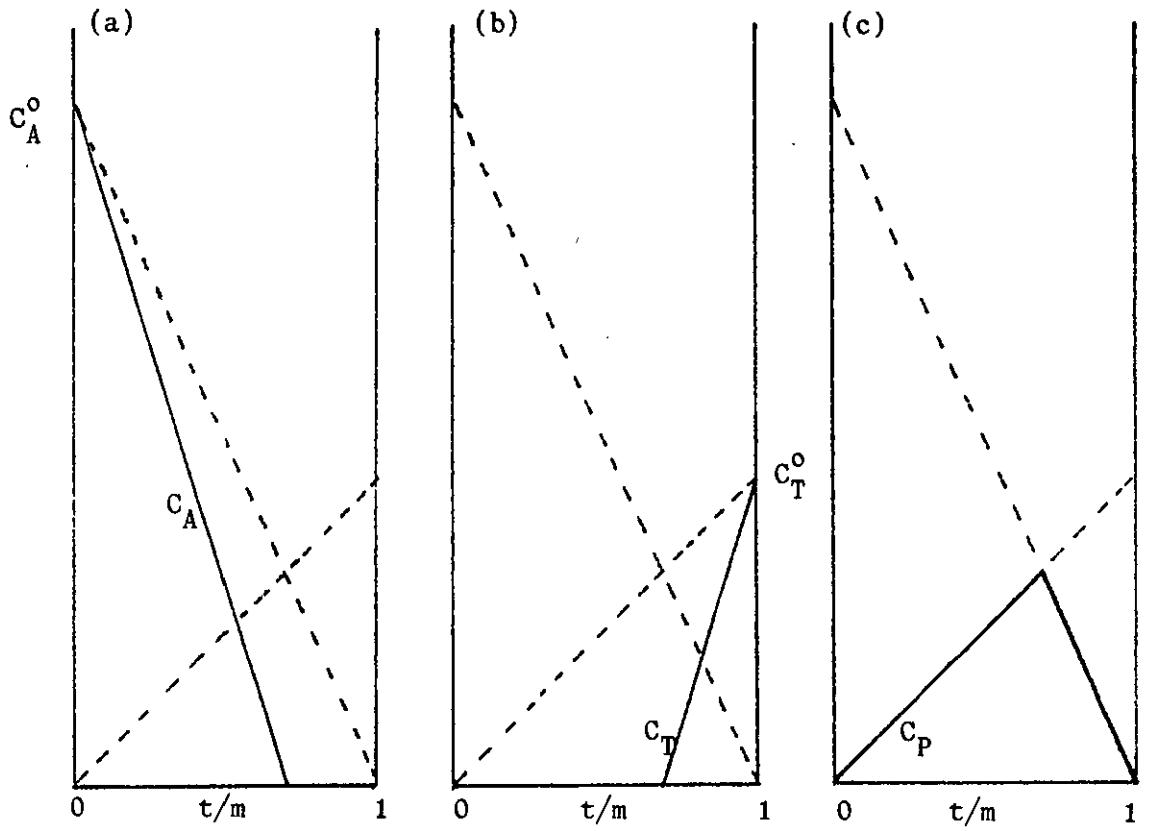

Fig. 5.8 Linear concentration gradients in tank for the reaction A + T→P at reduced times t/m, m being the emptying time of the variable volume tank reactor. C_A^o is the original analyte concentration and C_T^o is the concentration of titrant added. (a) Net analyte concentration, C_A; (b) net titrant concentration, C_T; (c) net product concentration, C_P. The dotted lines represent pure dilution effects on C_A^o and C_T^o.

To the analyte, orginally present at concentration C_A°, is added titrant at concentration C_T°. In the absence of reaction, the concentration gradients are described by equations 5.9 and 5.10 in the specific forms:

$$C_A = C_A^\circ (1 - t/m) \qquad 5.16$$

$$C_T = C_T^\circ t/m \qquad 5.17$$

These relations are shown as dashed lines in Fig. 5.8.

When reaction occurs there is further depletion in the concentration of A, which follows Fig. 5.8a, and is given by:

$$C_A = C_A^\circ (1 - t/m) - C_T^\circ t/m, \qquad t<t_e \qquad 5.18a$$

The first term represents the effect of dilution and the second the effect of reaction on adding titrant.

Titrant accumulates in the tank post-equivalence point, where the concentration (C_T) approaches C_T° as the tank empties following Fig. 5.8b, which is algebraically:

$$C_T = C_T^\circ t/m - C_A^\circ (1 - t/m), \qquad t>t_e \qquad 5.19a$$

Finally, the product concentration (C_p) follows Fig. 5.8c. Up to the equivalence point, the amount of product present is the total amount of titrant added less the quantity washed out by the mixing process. The concentration of product then follows the accumulation curve of equation 5.17. This concentration is a maximum at the equivalence point, thereafter decreasing as the product is washed out following equation 5.16, viz:

$$C_p = C_T^\circ \, t/m \quad , \qquad t < t_e \qquad 5.20$$

$$C_p = C_A^\circ \, (1 - t/m) \quad , \qquad t > t_e \qquad 5.21a$$

$$(C_p)_{max} = C_A^\circ \, (1 - t_e/m) = C_T^\circ \, t_e/m, \qquad t = t_e \qquad 5.22$$

The equivalence point (t_e/m) occurs when $C_T = C_A = 0$, and from equation 5.22, is given by:

$$\frac{t_e}{m} = \frac{C_A^\circ}{C_A^\circ + C_T^\circ} \qquad 5.23$$

This expression is the same as equation 1.29 deduced by Bound and Fleet (139) by a geometric argument, and can be used to obtain identities of previous relations, convenient in further discussion, e.g.

$$C_A = C_A^\circ \, (1 - t/t_e) \quad , \qquad t < t_e \qquad 5.18b$$

$$C_T = C_T^\circ \, \frac{(t - t_e)}{(m - t_e)} \quad , \qquad t > t_e \qquad 5.19b$$

$$C_p = (C_p)_{max} \, \frac{(m - t)}{(m - t_e)} \quad , \qquad t > t_e \qquad 5.21b$$

These concentration relations during titration can be established more formally by means of instantaneous material balances in the tank:

(i) For A; pre-equivalence point, ($t < t_e$)

input = accumulation + output + reaction (removal)

$$0 = \frac{d(VC_A)}{dt} + f_2 C_A + f_1 C_T^\circ$$

Using $f_2 = 2f_1$, $V = f_1 \, (m - t)$ and expanding, then

$$\frac{dC_A}{dt} + \left(\frac{C_A + C_T^\circ}{m - t} \right) = 0$$

The solution of which, between the limits 0, C_A° and t, C_A is:

$$C_A = C_A^\circ (1 - t/m) - C_T^\circ \, t/m \qquad 5.18a$$

(ii) For T; post-equivalence point, ($t > t_e$)

input = accumulation + output

$$f_1 C_T^\circ = \frac{d(VC_T)}{dt} + f_2 C_T$$

proceeding as above

$$\frac{dC_T}{dt} + \left(\frac{C_T - C_T^\circ}{m - t}\right) = 0$$

The solution of which, between the limits, t_e,0 and t,C_T is:

$$C_T = C_T^\circ \left(\frac{t - t_e}{m - t_e}\right) \qquad 5.19b$$

(iii) For P; pre-equivalence point, ($t < t_e$)

reaction (production) = accumulation + output

$$f_1 C_T^\circ = \frac{d(VC_p)}{dt} + f_2 C_p$$

proceeding as previously

$$\frac{dC_p}{dt} + \left(\frac{C_p - C_T^\circ}{m - t}\right) = o$$

The solution of which between the limits 0,0 and C_p,t is:

$$C_p = C_T^\circ \, t/m \qquad 5.20$$

(iv) For P; post-equivalence point, ($t > t_e$)

input = accumulation + output

$$0 = \frac{d(VC_p)}{dt} + f_2 C_p$$

proceeding as previously

$$\frac{dC_p}{dt} - \frac{C_p}{(m-t)} = 0$$

The solution of which between the limits $(C_p)_{max}$, t_e and C_p,t is:

$$C_p = (C_p)_{max} \left(\frac{m - t}{m - t_e} \right) \qquad 5.21b$$

It is instructive to compare these relations with those pertaining to the analogous conventional batch titration, where to a volume V_o of analyte is added a volume b of titrant, as in Table 5.2. The batch titration is evaluated in the presence and absence ($V_o >> b$) of dilution.

Table 5.2 Concentration of Analyte, Titrant and Product in Batch and Flow Titrations

	Component	Batch	Batch with dilution	Flow
(a)	T	0	0	0
	P	$C_T^\circ \frac{b}{V_o}$	$C_T^\circ \frac{b}{(V_o + b)}$	$C_T^\circ \frac{t}{m}$
	A	$C_A^\circ - C_T^\circ \frac{b}{V_o}$	$C_A^\circ \cdot \frac{V_o}{(V_o+b)} - C_T^\circ \cdot \frac{b}{(V_o+b)}$	$C_A^\circ (1-t/m) - C_T^\circ t/m$
(b)	A	0	0	0
	P	C_A°	$C_A^\circ \cdot \frac{V_o}{(V_o+b)}$	$C_A^\circ (1 - t/m)$
	T	$C_T^\circ \frac{b}{V_o} - C_A^\circ$	$C_T^\circ \cdot \frac{b}{(V_o+b)} - C_A^\circ \cdot \frac{V_o}{(V_o+b)}$	$C_T^\circ \frac{t}{m} - C_A^\circ(1-t/m)$

(a) before equivalence point

(b) after equivalence point

It may be noted that the modifications to the basic relations produced by accumulative dilution in the batch method are non-linear but the modifications in the flow case are linear and so are free of a curvature distortion.

The theoretical concentration gradients established in this section for the variable volume tank reactor can be directly examined by a study of classic, self-indicating photometric titrations carried out in the flow mode.

5.2.1 Follow Analyte. Titration of Fe(III) - salicylic acid by EDTA

Typical titration curves are shown in Figs. 5.9 and 5.10 and are linear as expected although end-effects, presumably due to dispersion, are also present. These end-effects get progressively more important with reduction in titration time, (Fig. 5.9). The construction for the calculation of the end-point (t_e) is indicated in the figures.

The slopes of the titration curves calculated from equation 5.18a agree well with the experimental values calculated from Figs. 5.9 and 5.10 and are shown in Table 5.3:

Table 5.3 Comparison of Experimental and Theoretical Titration Curves

$\frac{C_T^\circ}{C_A^\circ}$	m/s	Theoretical slope/s^{-1} $(C_T^\circ/C_A^\circ + 1)$ 1/m	Experimental slope/s^{-1}
1.005	617	3.25×10^{-3}	3.21×10^{-3}
10.20	601.5	18.6×10^{-3}	17.9×10^{-3}
10.204	588	19.1×10^{-3}	18.9×10^{-3}
38.095	600	64.7×10^{-3}	64.9×10^{-3}

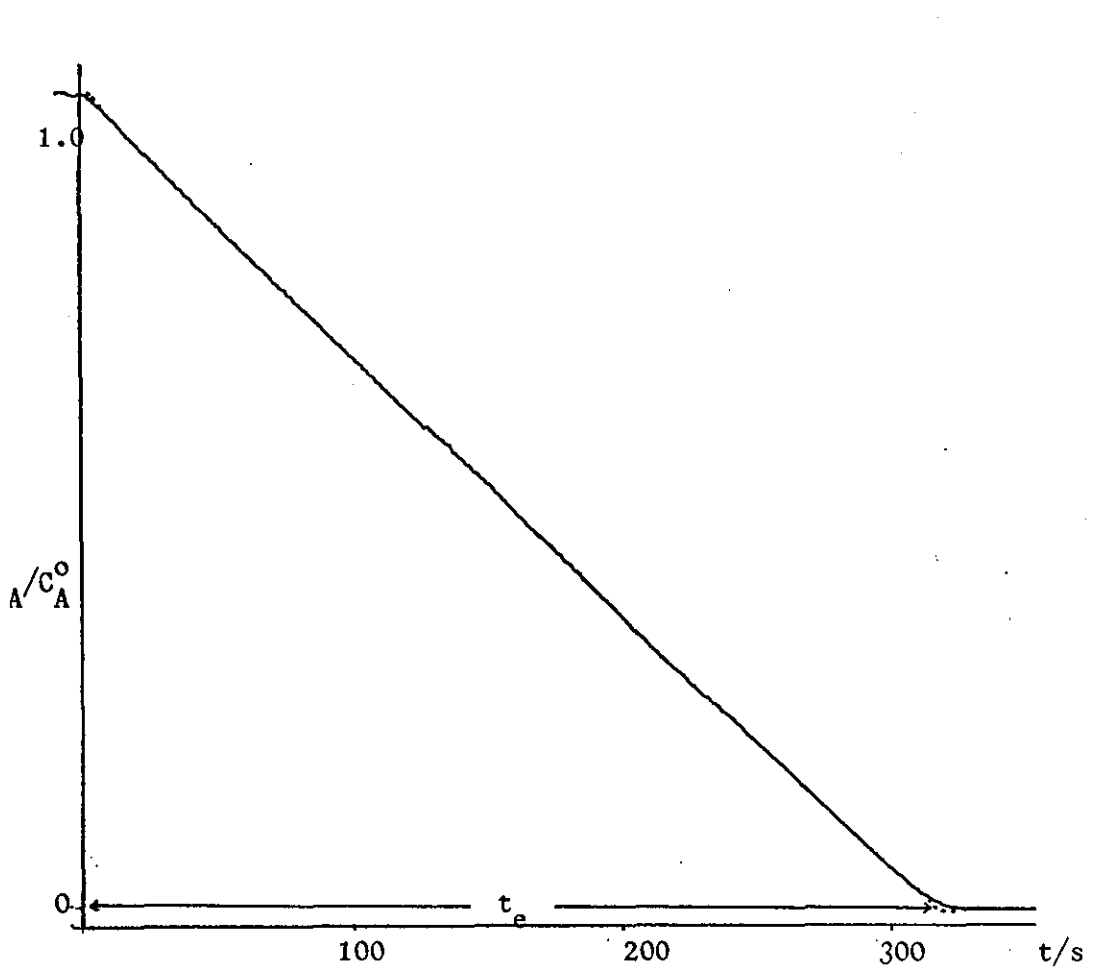

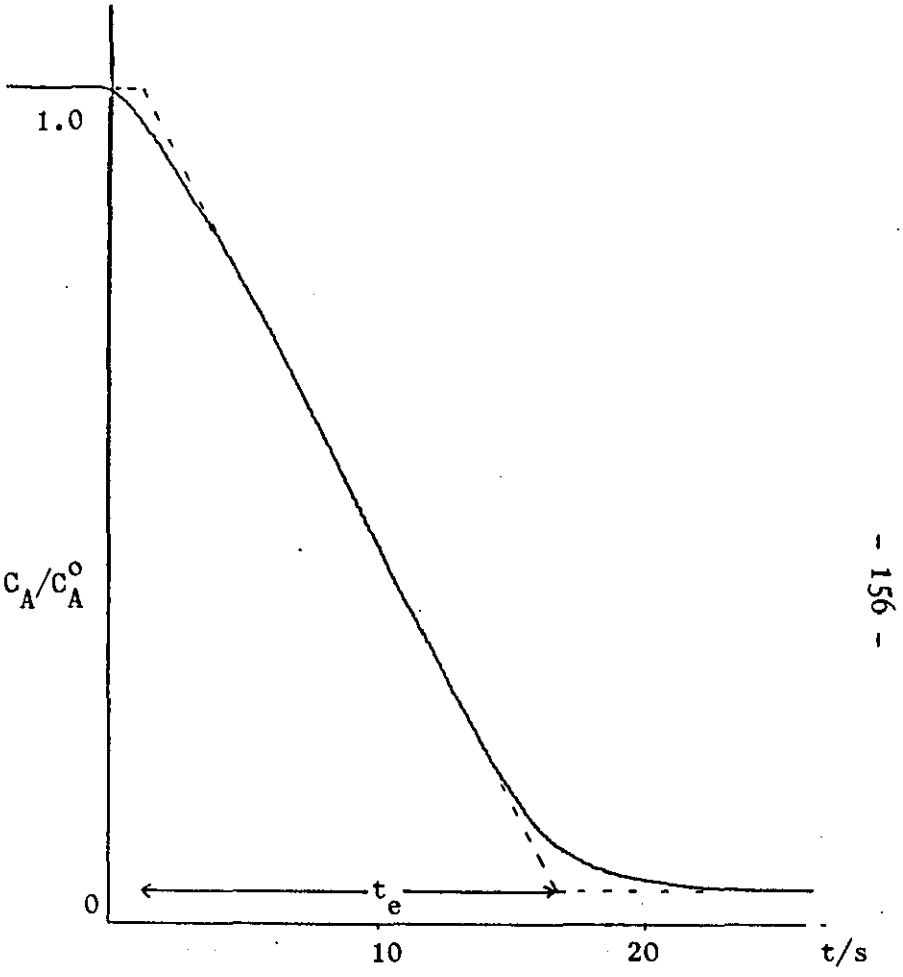

Fig. 5.9 Fe(III)-salicylic acid vs. EDTA. Flow titration.
Double pump, single exit line manifold. (a) Titrant to analyte concentration ratio (C_T^o/C_A^o) = 1.005, emptying time (m) = 617s, equivalence point (t_e) = 312s. (b) C_T^o/C_A^o = 38.095, m = 600s, t_e = 15.4s.

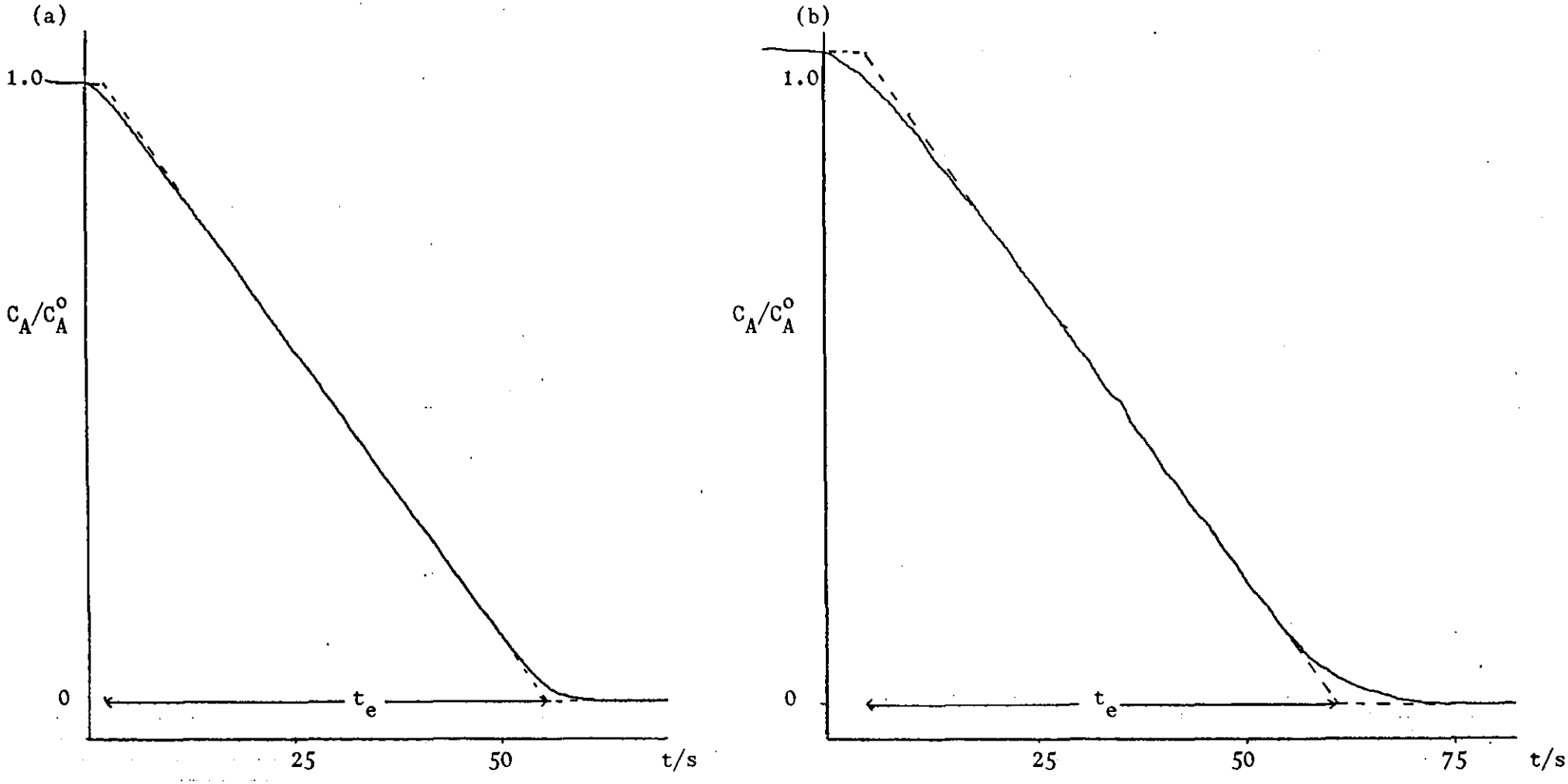

Fig. 5.10 Fe(III)-salicylic acid vs. EDTA. Flow Titration. (a) Double pump, single exit line manifold. Titrant to analyte ratio (C_T^o/C_A^o) = 10.204, emptying time (m) = 588s, equivalence point (t_e) = 53s. (b) Single pump, twin exit line manifold. C_T^o/C_A^o = 10.200, m = 601.5s, t_e = 56s.

Experimental end-points are compared with those predicted from equation 5.23 over an extensive range of values. Results were obtained using both the two pump, single exit line manifold of Fig. 4.1c and with the single pump, twin exit line manifold of Fig. 4.1b.

Results with the single exit line manifold are shown in Table 5.4. Theoretical and experimental titration times (t_e) agree with an overall coefficient of variation for the n = 27 datum points of 1.42 per cent. Since the theoretical value is based on the C_T°/C_A° ratio established from the corresponding batch titration assuming negligible error, the regression of t_e (expt) on t_e (theory) is a test of the compatibility of batch and flow titration modes. The parameters of the regression at the 95 per cent confidence level were (194):

$$t_e \text{ (expt)} = (1.002 \pm 0.006) t_e \text{ (theory)} - 0.6 \pm 0.9$$

Thus no systematic difference exists between flow and batch methods. The same conclusion applies when m is calculated from a net flow based on the directly measured (f_2-f_1) value; or even when this difference is assumed to be 1 ml min^{-1}, justified on the basis that the majority of flows accepted were within 2 per cent of 1 ml min^{-1} and 2 ml min^{-1} for f_1 and f_2 respectively.

Results with the single pump, twin exit line manifold are shown in Table 5.5. Regression of t_e (expt) on t_e (theory) again failed to detect any significant difference at the 95% confidence level between flow and batch titrations:

$$t_e \text{ (expt)} = (1.02 \pm 0.04)\ t_e \text{ (theory)} - 0.5 \pm 3.6$$

TABLE 5.4 Evaluation of titration times using two pump manifold

C_T°/C_A°	f_1/ ml/min^{-1}	f_2/ ml min^{-1}	m/min	t_e(theory)/s	t_e(expt)/s	Coeff. of variation/%
1.005	0.99	1.96	10.150	304	300	
	0.97	1.96	10.252	307	305	
	0.97	1.95	10.288	308	312	
	0.96	1.90	10.458	313	316	1.26
1.98	0.99	2.00	10.050	202	202	
	1.01	2.02	9.901	199	198	
	1.02	2.01	9.876	199	201	
	1.01	2.02	9.901	199	198	0.71
5.00	1.00	2.00	10.000	100	100	
	1.00	2.01	9.975	100	100	
	0.99	2.00	10.050	101	100	
	0.98	1.98	10.151	102	102	0.57
9.48	1.02	2.04	9.804	56	55	
	1.01	2.02	9.901	57	56	
	0.99	2.00	10.050	57.5	56.5	
	0.99	1.97	10.127	58.5	57	
	1.00	1.99	10.025	58	57	2.88
19.231	1.01	2.01	9.926	29.4	29.4	
	1.00	2.02	10.050	29.8	30.0	
	1.01	2.01	9.926	29.4	29.6	
	1.00	2.01	9.975	29.6	29.0	
	1.01	2.03	9.877	29.3	29.5	1.17
38.095	0.99	1.99	10.076	15.5	15.4	
	1.00	2.00	10.000	15.3	14.9	
	1.00	2.04	9.901	15.2	15.2	
	1.02	2.02	9.852	15.1	15.3	
	0.99	1.99	10.076	15.5	15.2	1.81

$$V_o = 10 \text{ ml.}, \quad m = \frac{v_o}{(f_1 - 0.5\, f_2)\, 0.5}$$

$$\text{Coeff. of variation} = \sqrt{\frac{\Sigma\ (\text{deviation})^2}{n - 1}} \quad \text{per cent}$$

$$\text{deviation} = \frac{t_e\ (\text{exptal}) - t_e\ (\text{theory})}{t_e\ (\text{theory})} \times 100 \text{ per cent}$$

TABLE 5.5 Evaluation of titration times using single pump manifold

C_T°/C_A°	f_1/ ml min^{-1}	f_2/ ml min^{-1}	m/min	t_e(theory)/s	t_e(expt)/s	Coeff. of variation/%
1.000	0.98	1.95	10.230	307	309	
	0.99	1.99	10.076	302	301	
	1.00	1.99	10.025	301	320	4.74
1.99	1.00	2.01	9.95	200	210	
	1.01	2.09	9.73	195	206	
	0.97	1.91	10.39	208	206	
	0.97	2.00	10.15	204	210	3.85
3.38	1.10	2.17	9.153	125	128.5	
	1.09	2.17	9.195	126	127	
	1.13	2.17	9.029	123.5	122.5	2.14
10.20	1.00	1.99	10.025	54	56	
	1.00	2.04	9.901	53	55	
	1.02	2.06	9.756	52	55	5.51

V_o = ml., $m = \dfrac{V_o}{(f_1 + 0.5\, f_2)0.5}$

Coeff. of variation $= \sqrt{\dfrac{\Sigma\,(\text{deviation})^2}{n-1}}$ per cent

deviation $= \dfrac{t_e\,(\text{exptal}) - t_e\,(\text{theory})}{t_e\,(\text{theory})} \times 100$ per cent

However for the n=13 datum points collected, the coefficient of variation between theoretical and experimental values was increased to 3.65 per cent. This was because of the greater uncertainty in the value of f_2 since it was made from the combination of two flows and also because of the increase in the dispersion effect in the detector-transmission line since flow through this was fifty per cent slower at 1 ml min^{-1} than in the previous case. This increased dispersion is apparent in Fig. 5.10, where the titration was performed with each manifold under comparable conditions. Despite the better economy of the single pump manifold it was not used in further work because of its reduced performance.

5.2.2 Follow Titrant. Titration of Fe(II) by Mn(VII)

A typical titration curve is shown in Fig. 5.11. Since the start of this titration is not auto-indicated, the total appearance time (t_A) includes the transportation lag of 4.3 ± 0.2s, and allowance is made for this in the calculation of equivalence time (t_e) as indicated. The foot of the rise curve also indicates the presence of a dispersion lag; but estimation of this was not included in calculations, since it would be uncompensated in a single event end-point location of this type.

Theoretical end-points are calculated from equation 5.23, modified to account for the stoichiometry of the reaction involved, viz:

$$\frac{t_e}{m} = \frac{C_A^\circ}{C_A^\circ + 5C_T^\circ} \qquad 5.24$$

Calculated and experimental values are thus compared in Table 5.6 for a set of titrations at $C_A^\circ/C_T^\circ = 1.00$.

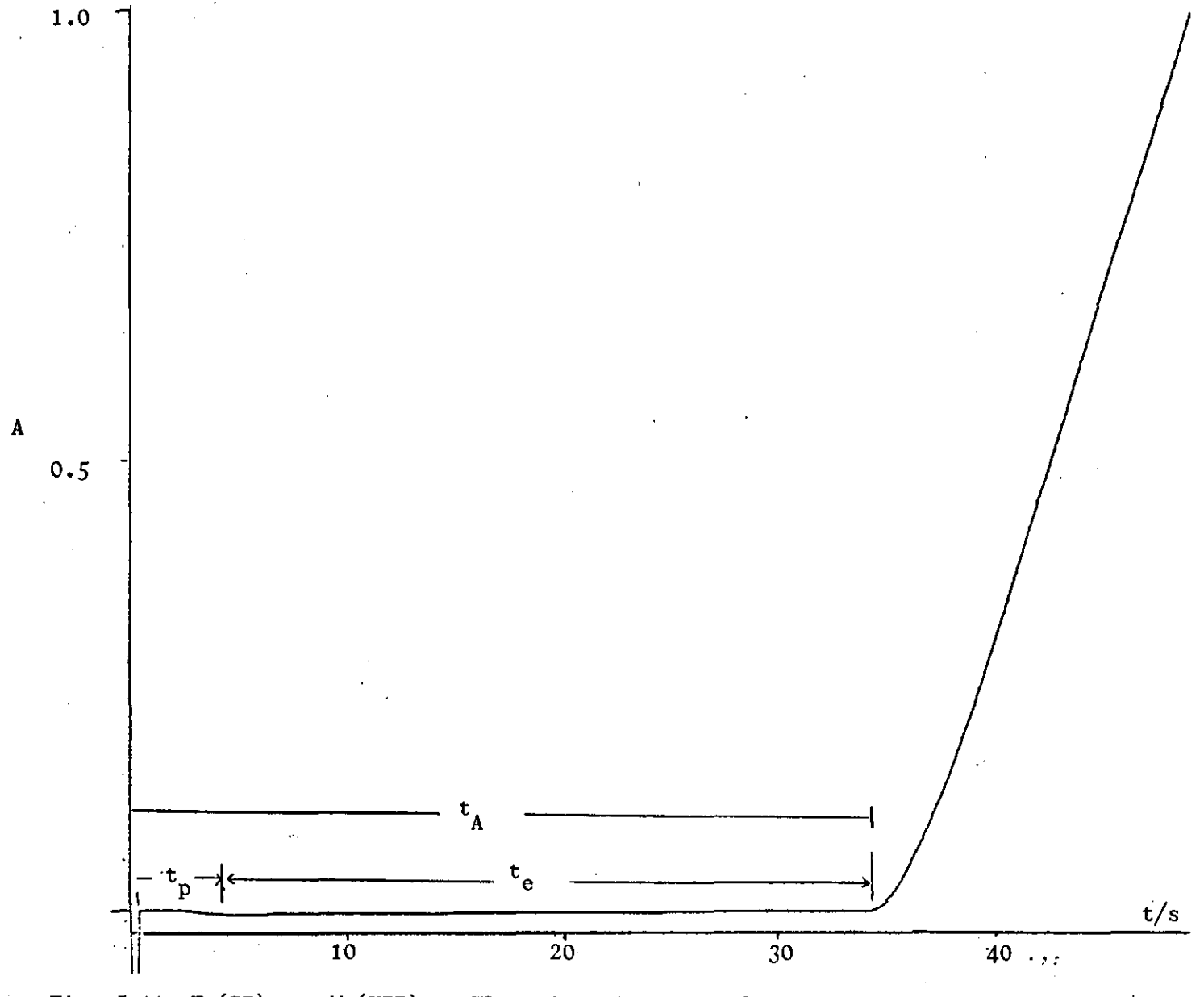

Fig. 5.11 Fe(II) vs. Mn(VII). Flow titration. Analyte to titrant concentration ratio (C_A^o/C_T^o) = 0.250, emptying time (m) = 595.5s. Total appearance time (t_A) = 34.0s. Transportation lag (t_p) = 4.3s. Thus equivalence time (t_e) = $t_A - t_p$ = 29.7s.

Table 5.6 Follow Titrant. Fe(II) vs Mn(VII). Evaluation of Titration Times

$C_A^\circ/C_T^\circ = 1.00$
$V_O = 10$ ml
$t_p = 4.3 \pm 0.2$ s ~ 4 s
t_e (expt) $= t_A - t_p$
t_e (theory) from equation 5.24

f_1/ml min^{-1}	f_2/ml min^{-1}	m/s	t_A/s	t_e(expt)/s	t_e(theory)/s
0.99	1.98	606	104	100	101
0.99	1.99	605	105	101	101
1.00	1.98	603	103.5	99.5	100.5
1.00	2.02	597	105	101	99.5

Coefficient of variation between t_e(expt.) and t_e(theory) is 1.4%.

Flow photometric titrations of this type are thus demonstratably reproducible with an accuracy comparable to that found by following the analyte. Further confirmation of this is displayed in Fig. 5.12, where experimental data obtained by titrating various Fe(II) concentrations with 0.02 M $KMnO_4$ (shown in Table 5.7) fall on the theoretical line expected from:

$$\frac{t_e}{m - t_e} = \frac{C_A^\circ}{5C_T^\circ} \qquad 5.25$$

This relation is an identity of equation 5.24, the time function $t_e/(m-t_e)$ being analogous to the V_T/V_A ratio of a batch titration in being proportional to the analyte concentration when the analyte is titrated by a standard titrant solution.

Table 5.7 Follow Titrant. Fe(III) vs. Mn(VII). Experimental Results at Various analyte to titrant ratios

C_A°/C_T°	f_1/ml min^{-1}	f_2/ml min^{-1}	m/s	t_A/s	t_e/s	$t_e/m-t_e$
0.25	1.01	2.01	595.5	34.0	29.7	0.052
0.518	1.00	1.97	604.5	62.5	58.2	0.106
1.000	0.99	1.99	604.5	105.0	100.7	0.200
2.078	1.00	2.00	600	181.5	177.2	0.419
4.170	1.00	2.01	597.5	274	269.7	0.835

$t_e = t_A - t_p$

$t_p = 4.3\ (\pm 0.2)$s

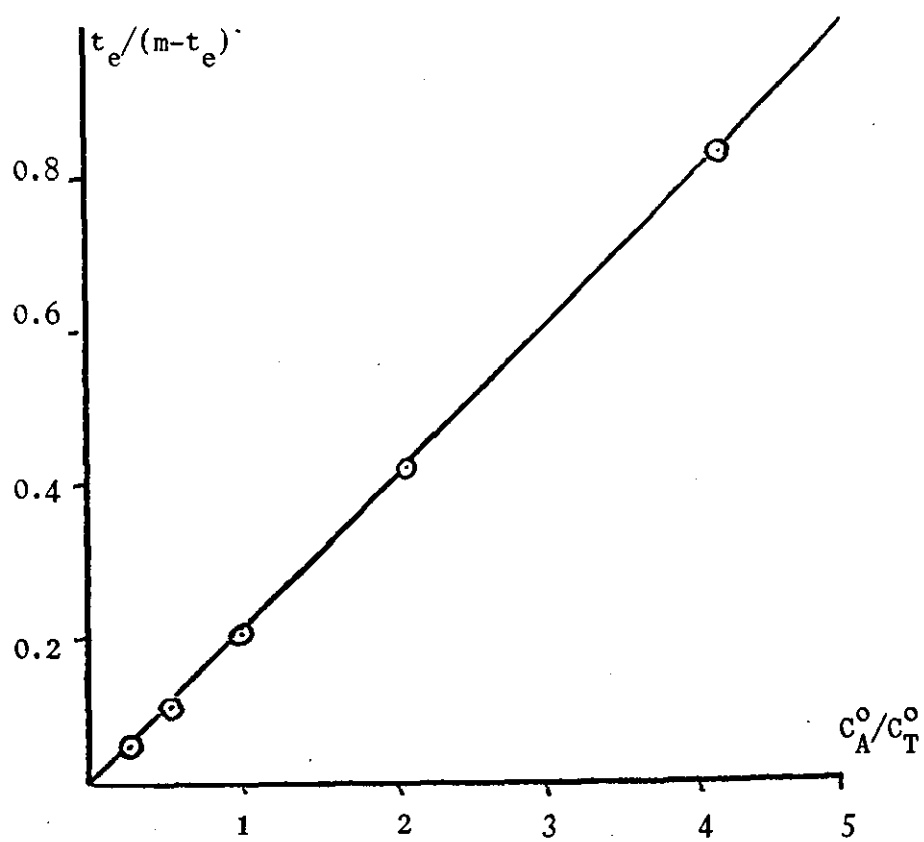

Fig. 5.12 Flow titration results. Fe(II) vs. Mn(VII).
Time function $t_e/(m-t_e)$ against analyte to titrant ratio, C_A°/C_T°. Full line is the theoretical relation, equation 5.24; circles represent experimental results from Table 5.7.

5.2.3 Follow Product

5.2.3.1 Titration of Fe(III) by SCN^-

Fig. 5.13 shows the titration curves for $C_T^\circ = C_A^\circ$ and $C_T^\circ = 10\ C_A^\circ$. In each case a broad maximum is displayed, but in the former case only does the maximum occur in the region of the expected end-point.

This curvature is probably attributable to the weak nature of the complex formed. The exposition given earlier for the formation of an undissociated product can be readily modified to this situation, however. Following Flashka (195) the product concentration can be calculated for the reaction:

$$A + T \rightleftharpoons P$$

The following stoichiometric and thermodynamic relations apply:

$$C_A = [A] + [P]$$

$$C_T = [T] + [P]$$

$$K_f = \frac{[P]}{[A][T]}$$

[A], [T] and [P] are actual concentrations, C_A and C_T are concentrations in the absence of reaction and K_f is the conditional formation constant relevant to the conditions existing in the titration. Defining a titration factor (a) as C_T/C_A, the relations above generate (195):

$$[P]^2 - [P]\ (1/K_f + C_A + aC_A) + aC_A^2 = 0 \qquad 5.26$$

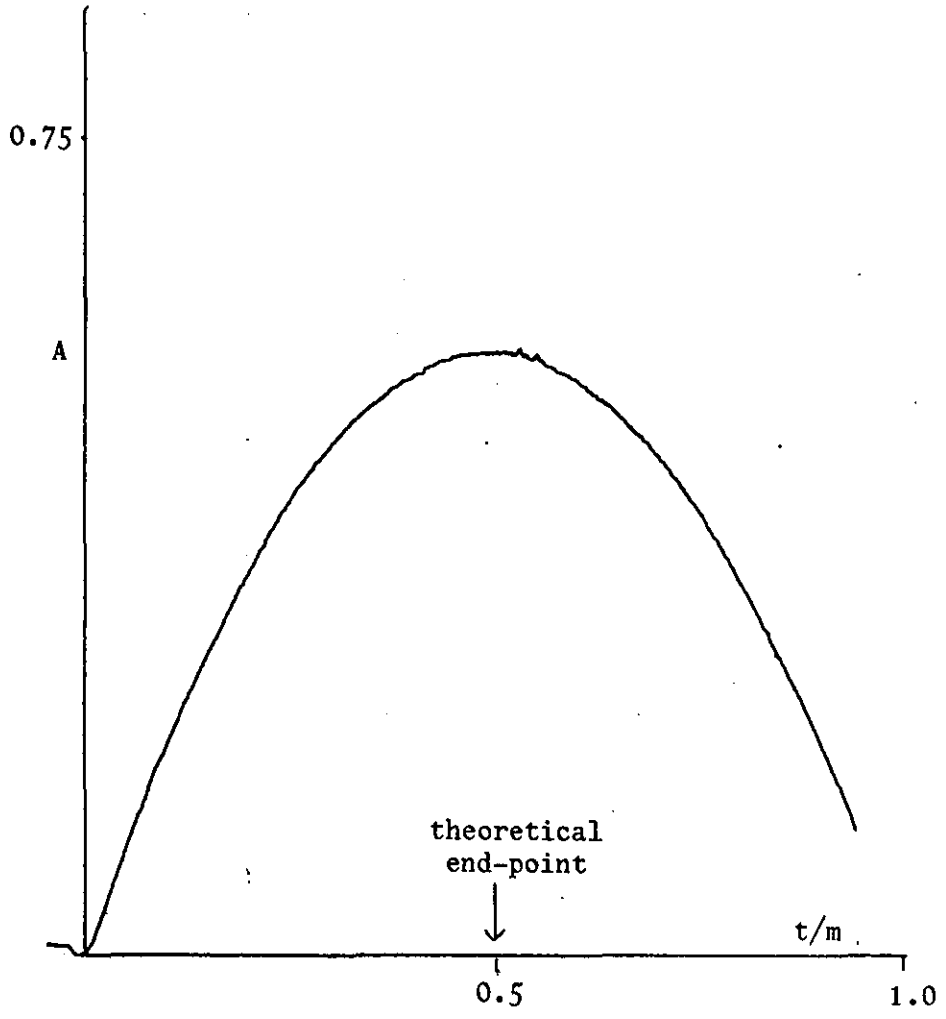

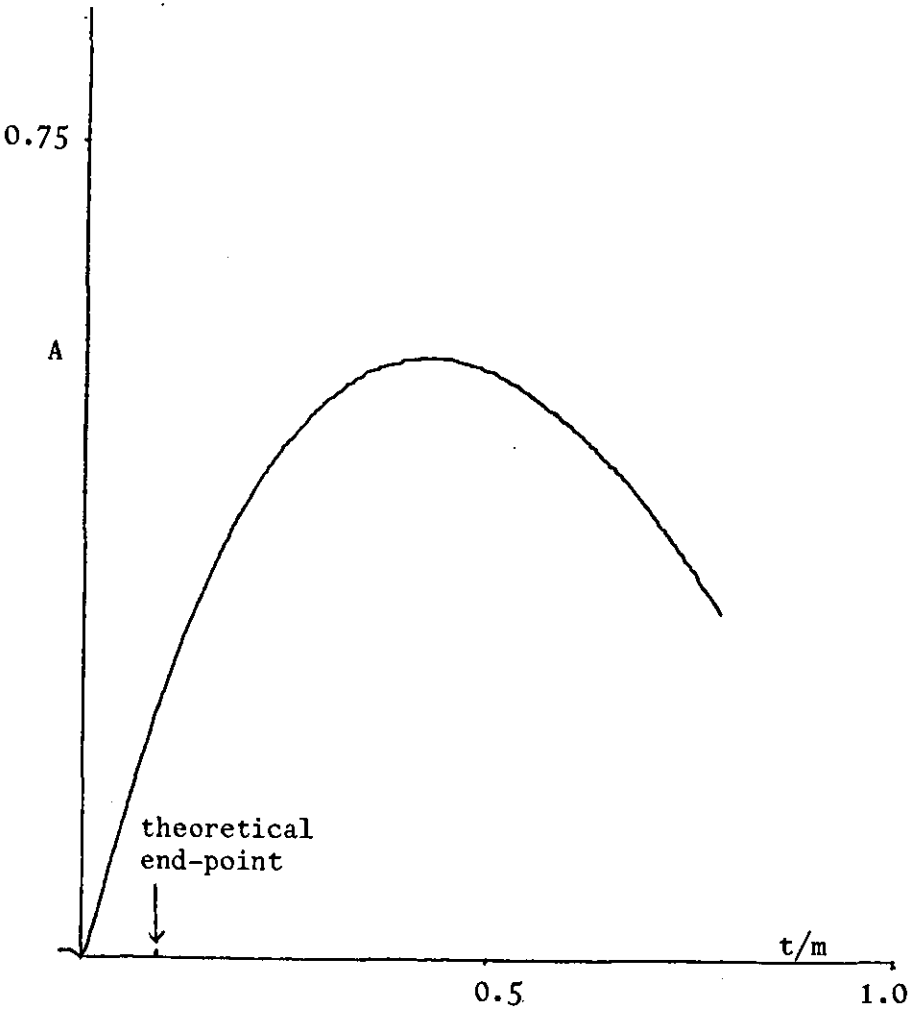

Fig. 5.13 Fe(III) vs. CNS^- titration curves. (a) $C_T^o/C_A^o = 1$, 1×10^{-3} M Fe(III), 1×10^{-3} M CNS^-. $V_o = 5$ ml, $f_1 = 0.98$ ml min^{-1}, $f_2 = 1.97$ ml min^{-1}. (b) $C_T^o/C_A^o = 10$, 5×10^{-4} M Fe(III), 5×10^{-3} M CNS^-. $V_o = 5$ ml, $f_1 = 1.00$ ml min^{-1}, $f_2 = 2.00$ ml min^{-1}.

This relation is directly applicable to a batch titration, where if dilution is neglected C_T/C_A is C_T°/C_A°. The expression can also be applied to the flow titration, where, as previously, $C_A = C_A^\circ(1-t/m)$ and $C_T = C_T^\circ\ t/m$.

Equation 5.26 is applied to the Fe(III)/SCN^- system in Fig. 5.14. The flow titration theoretical curves have the same limitation from an analytical point of view as the experimental ones, also the theoretical undiluted batch titration curve is equally unsatisfactory. The same effect is apparent in an actual dilution distorted batch photometric titration curve for this system (183, Fig. 2a). This universal limitation of the photometric method is attributable to the unfavourable thermodynamics of the system.

The $C_T^\circ = C_A^\circ$ flow titration example above fulfils the conditions of the continuous variation or Job method for the investigation of complexes (196). (Likewise, a batch titration is a form of the molar ratio method). The continuous range of dilutions afforded by this flow method would be expected to offer some advantages over its discrete Job method counterpart, particularly when subtle effects arising from the formation of multiple complexes exist (197).

Furthermore if equation 5.26 is differentiated with respect to the flow titration time variable t/m:

$$\frac{d[P]}{d(t/m)}\left[2[P] - 1/K_f - C_A^\circ + C_A^\circ\ t/m - C_T^\circ\ t/m\right] = 2\ C_T^\circ\ C_A^\circ\ t/m - C_T^\circ\ C_A^\circ + [P]\ (C_T^\circ - C_A^\circ) \qquad 5.27$$

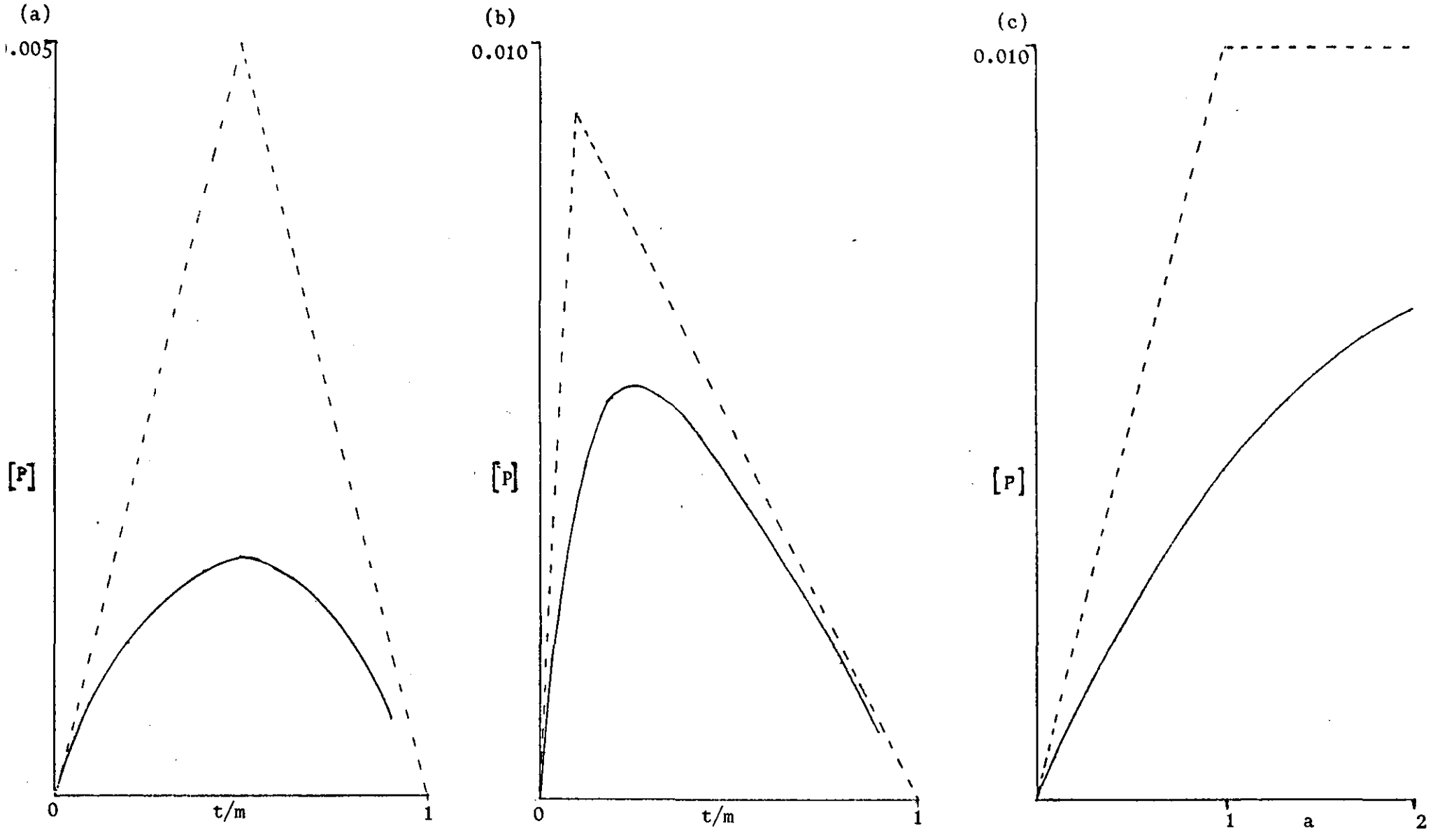

Fig. 5.14 Fe(III) vs. CNS^-. Calculated titration curves, full lines with $K_f = 1.4 \times 10^2$ (183);
(a) Flow titration, equation 5.26 for $C_A^o = C_T^o = 0.01$ M. (b) Flow titration, equation 5.26 for $C_A^o = 0.01$ M, $C_T^o = 0.1$ M.
(c) Batch titration, equation 5.26 for $C_A^o = C_T^o = 0.01$ M. Dotted lines, corresponding titrations with $K_f = \infty$

At the maximum of the flow titration curve,

$$\left[\frac{d[P]}{d(t/m)}\right]_{max} = 0, \text{ and}$$

$$(t/m)_{max} = \frac{1}{2} - \frac{[P]\,(C_T^\circ - C_A^\circ)}{2\,C_T^\circ\,C_A^\circ} \qquad 5.28$$

Thus for very weak 1:1 complexes, [P] is small and $(t/m)_{max}$ will always be fairly close to 0.5, actually attaining this value under the $C_T^\circ = C_A^\circ$ condition. This insight corroborates an earlier observation that the Job curve maximum is central over a range of conditions when the complex formed is weak (198), and explains the relative success of the equimolar flow titration.

5.2.3.2 Titration of 2,4-dinitrophenol by OH^-

10 ml of a saturated solution by 2,4-dinitrophenol was titrated with standard 0.01M NaOH at m=600s, the ensuing titration curve is shown in Fig. 5.15a. A titration time of 92s was obtained by extrapolating the linear parts of the curve, so that from equation 5.23, the acid strength was estimated to be 1.811×10^{-3}M. Because of the stability of the product, the form of the curve in the vicinity of the end-point more closely resembles the theoretical curve of Fig. 5.8c than is the case of the previous titration, although the initial high absorbance reading is due to pre-formation of some product at the natural pH of the analyte (approx. 3.4).

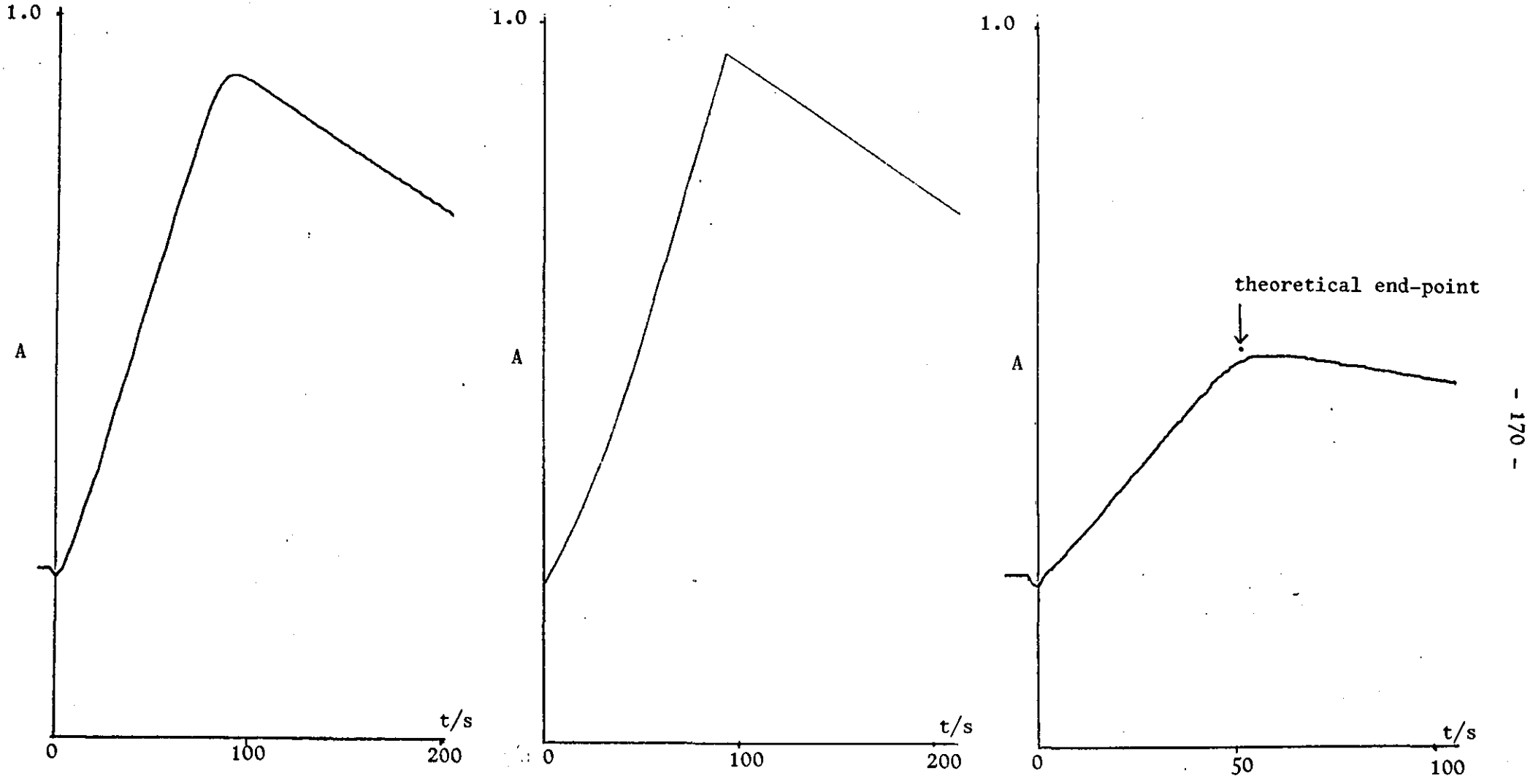

Fig. 5.15 2:4 dinitrophenol vs. OH^-. Flow titration curves. (a) saturated 2:4 dinitrophenol, 0.01M NaOH, emptying time(m) = 600s, t_e = 92s. Experimental curve. (b) 1.811×10^{-3} M 2:4 dinitrophenol, 0.01 M NaOH, m = 600s, t_e = 92s, A_{max} = 0.88, $K_A = 8.5 \times 10^{-5}$. Theoretical curve, equations 5.29, 5.31 (c) 0.95×10^{-3} M 2:4 dinitrophenol, 0.01 M NaOH, emptying time(m) = 594s, t_e = 52s. Experimental curve.

Following the exposition of Leonard (199), the titration is readily analysed quantitatively:

$$HX + NaOH \rightleftharpoons X^- + Na^+ + H_2O$$

Thermodynamic relationships are:

$$K_A = \frac{[H^+]\,[X^-]}{[HX]}$$

$$K_W = [H^+]\,[OH^-]$$

The charge balance relationship is:

$$[Na^+] + [H^+] = [OH^-] + [X^-]$$

And, in the case of the flow titration, mass balance relationships are:

$$[HX] + [X^-] = C^\circ_{HX}\,(1 - t/m)$$

$$[Na^+] = C^\circ_{NaOH} \cdot t/m$$

On combining, we obtain expression for the titration parameters t/m and $[X^-]$, viz:

$$t/m = \frac{\frac{K_W}{[H^+]} - [H^+] + \frac{C^\circ_{HX} K_A}{[H^+] + K_A}}{C^\circ_{NaOH} + \frac{C^\circ_{HX} K_A}{[H^+] + K_A}} \qquad 5.29$$

$$[X^-] = \frac{C^\circ_{HX}\,(1 - t/m)\,K_A}{[H^+] + K_A} \qquad 5.30$$

This product concentration can be compared to the theoretical end-point value for a perfectly stable complex $[X^-]_{max}$, which is given by equation 5.22. Also, in view of Beer's law, the ratio $[X^-]/[X^-]_{max}$ can be identified with A/A_{max}, so that:

$$\frac{A}{A_{max}} = \frac{K_A (1 - t/m)}{([H^+] + K_A)(1 - t_e/m)} \qquad 5.31$$

Equations 5.29 and 5.31 are used to reconstruct the titration curve for a range of pH values from 3.6 to 11.5 by adopting the experimental parameters, viz: $C_{HX} = 1.811 \times 10^{-3}$M, $C^{\circ}_{NaOH} = 0.01$M, $K_A = 8.5 \times 10^{-5}$ (185), $t_e = 92$s and $A_{max} = 0.88$ (the absorbance corresponding to the extrapolated end-point value in Fig. 5.15a). The ensuing theoretical curve, shown in Fig. 5.15b, is almost superimposable on the experimental one. However, there is some residual curvature in the region of the end-point in practice, which apart from theoretical inadequacies might also be attributable to a degree of dispersion at the completion of the reaction as discussed later.

In contrast to the Fe(III)/SCN^- case, this titration gives satisfactory results at higher titrant to analyte ratios. Using a C°_T/C°_A ratio of 10.526, as determined from a batch photometric titration, 10 ml of the phenol was titrated with 0.01M NaOH at m = 594s to produce the titration curve of Fig. 5.15c. From the measured titration time of 52.0s, a theoretical value for C°_T/C°_A of 10.424 was calculated from equation 5.23, which is within one per cent of the expected value.

5.2.4 Quantitative Treatment of Dispersion and Transportation Lag in Flow Titrations

5.2.4.1 Follow Analyte

(i) Pre-end point, $t < t_e$

The undistorted, linearly decreasing titration trace may be described by equation 5.18b, viz: $C_A/C_A^o = (1 - t/t_e)$. Thus on applying equation 5.15 to allow for dispersion, the constant A takes the form $1/t_e$, so that the analyte titration curve with dispersion becomes:

$$\frac{C_A}{C_A^o} = 1 - \frac{t}{t_e} + \frac{\tau_s}{t_e}\left(1 - e^{-t/\tau_s}\right) \qquad 5.32$$

(ii) Post end-point, $t > t_e$

At $t = t_e$, reaction in the tank is complete and the concentration of the analyte there is zero, but the concentration of analyte in the detector is finite at $(C_A)_{te}$. This concentration is then washed out of the system according to the exponential decay equation 5.6 appropriate to this situation, viz:

$$C_A = (C_A)_{t_e}\, e^{-(t-t_e)/\tau_s} \qquad 5.33$$

These relations are used to construct the titration curves of Fig. 5.16, for titration times of 15.4 and 54.5s, by taking τ_s as 1.2s as informed in section 5.1.3. These curves are directly comparable with the experimental ones in Figs. 5.9 and 5.10 and qualitative agreement is demonstrated. In this titration, consideration of the transportation lag is not relevant as the start of the titration is taken from the onset of concentration change.

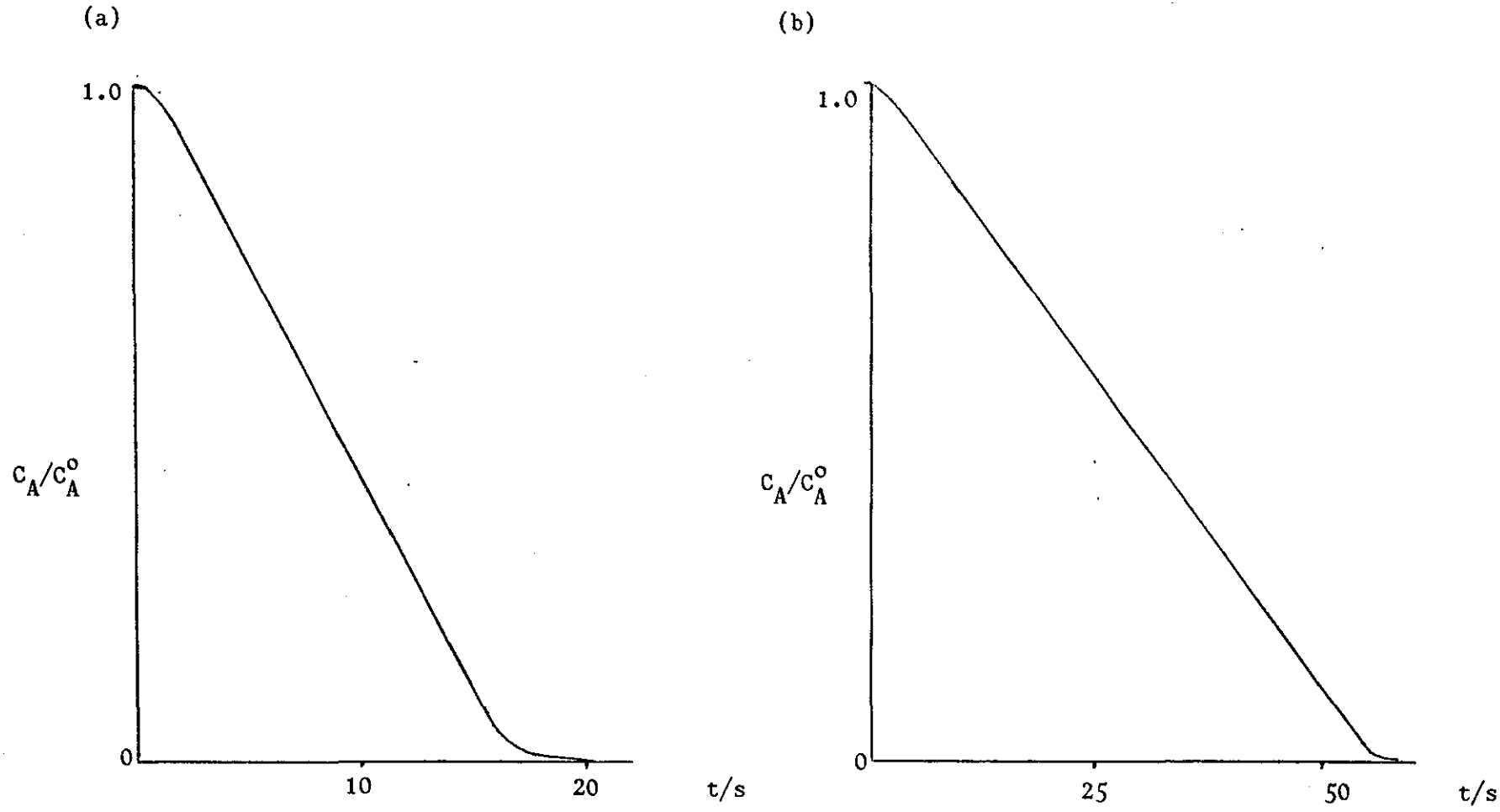

Fig. 5.16 Simulation of dispersion effect in flow titration, following analyte τ_s = 1.2s, (a) t_e = 15.4s, (b) t_e = 54.5s. Eqn. 5.32 used from t = 0 to t = t_e, eqn. 5.33 for remaining wash-out process

The dispersion effect places a lower limit on practical titration times, although experimental results demonstrate that satisfactory results may be obtained down to at least 15s.

5.2.4.2 Follow Titrant

The effect of dispersion on this type of titration is also amenable to theory. The undistorted titration curve is given by equation 5.19b, viz:

$$C_T/C_T^o = (t-t_e)/(m-t_e)$$

At post-equivalence times $(t-t_e)$, this is a linear gradient with constant term A given by $1/(m-t_e)$. Thus when in convolution with the detection mixing stage, the gradient is modified according to equation 5.14 to give:

$$\frac{C_T}{C_T^o} = \frac{1}{(m-t_e)} [(t - t_e) - \tau_s (1-e^{-(t-t_e)/\tau_s})] \quad 5.34$$

This relation was used to construct the rise curve in Fig. 5.17 by taking τ_s as 1.2s as previously, a titration time of 29.7 s and an emptying time of 595.5s. The simulation is completed by additively incorporating a transportation lag of 4.3s. Close agreement between this curve and the parent experimental curve of Fig. 5.11 is again demonstrated.

5.2.4.3 Follow product

Curvature in the region of the end-point may arise both from incomplete reaction and from dispersion. In order to isolate the effect of the latter, the theoretical construction which follows is based on a $K_f = \infty$ system.

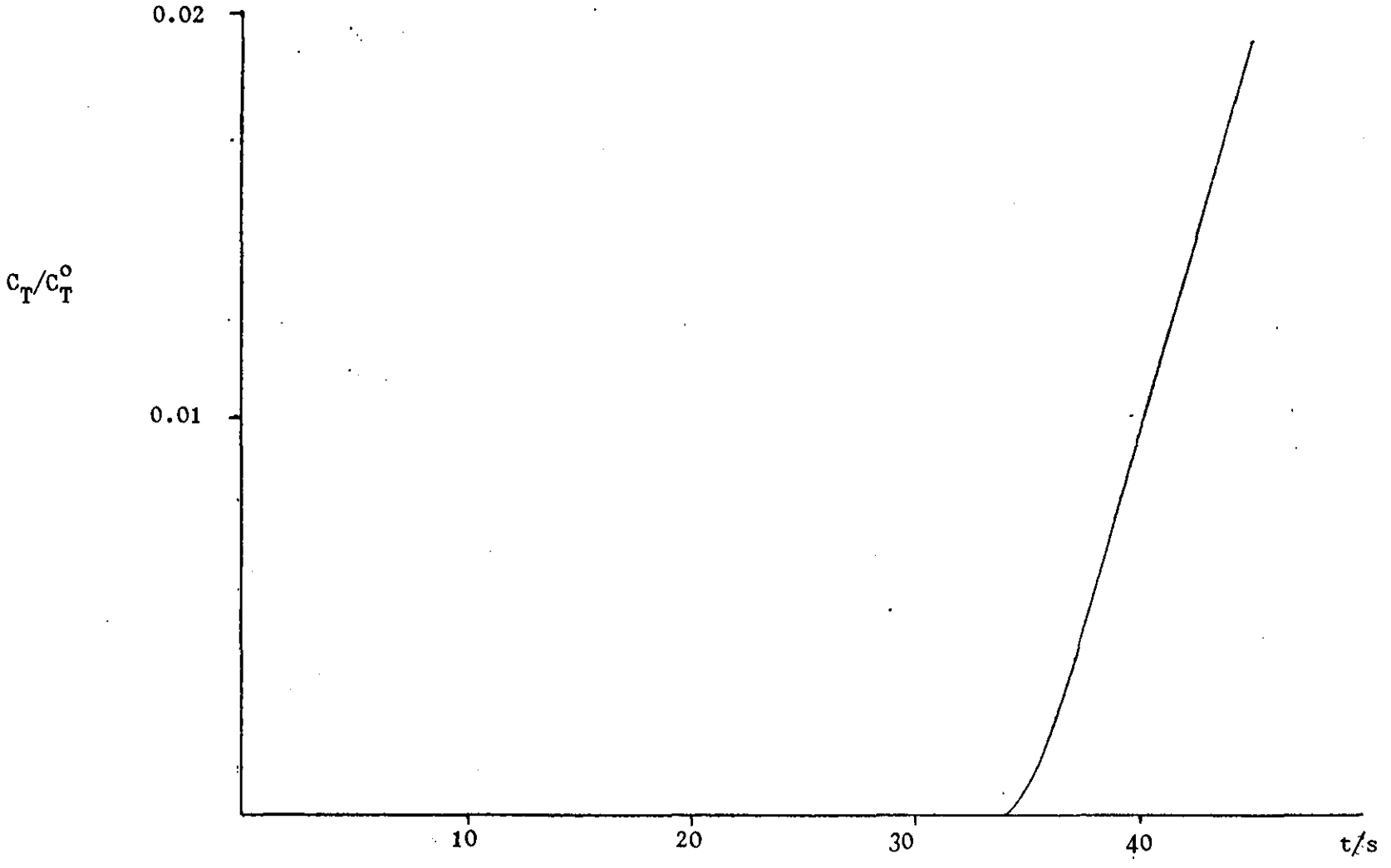

Fig. 5.17 Simulation of dispersion and transportation lag effects in flow titration. Following titrant, t_e = 29.7s, m = 595.5s, τ_s = 1.2s, t_p = 4.3s
Equation 5.34 used for rise curve.

(i) Pre-equivalence point, $t < t_e$

In this region, the undistorted titration curve is given by equation 5.20 viz $C_p/C_T^\circ = t/m$. On applying equation 5.14 to correct for dispersion, and identifying the constant A with 1/m, the titration curve becomes:

$$\frac{C_p}{C_T^\circ} = \frac{t}{m} - \frac{\tau_s}{m}(1 - e^{-t/\tau_s}) \qquad 5.35$$

(ii) Post equivalence point, $t > t_e$

When the reaction is complete at t_e, the product concentration in the tank is a maximum at $(C_p)_{max}$, but has a lower value $(C_p)_{te}$ in the detector. Thereafter, the concentration in the detector rises, following equation 5.3, which in this context is:

$$C_p = (C_p)_{max} - [(C_p)_{max} - (C_p)_{t_e}]e^{-(t-t_e)/\tau_s} \qquad 5.36$$

The overall rise curve thus has an exponential tail which merges with the final declining limb of the titration arising from the dilution of the maximum product concentration, $(C_p)_{max}$, as given by equation 5.21b.

The relations above are used to construct the titation curve in Fig. 5.18 taking τ_s = 1.2s as before, and with C_T° = 0.01M, m = 600s, t_e = 92s and calculating $(C_p)_{max}$, from equation 5.22 at $t=t_e$, to be 1.533×10^{-3} M. The inset in this figure illustrates the dispersion curvature in the region of the end-point; but the effect, in the context of the overall titration, is quite small. The

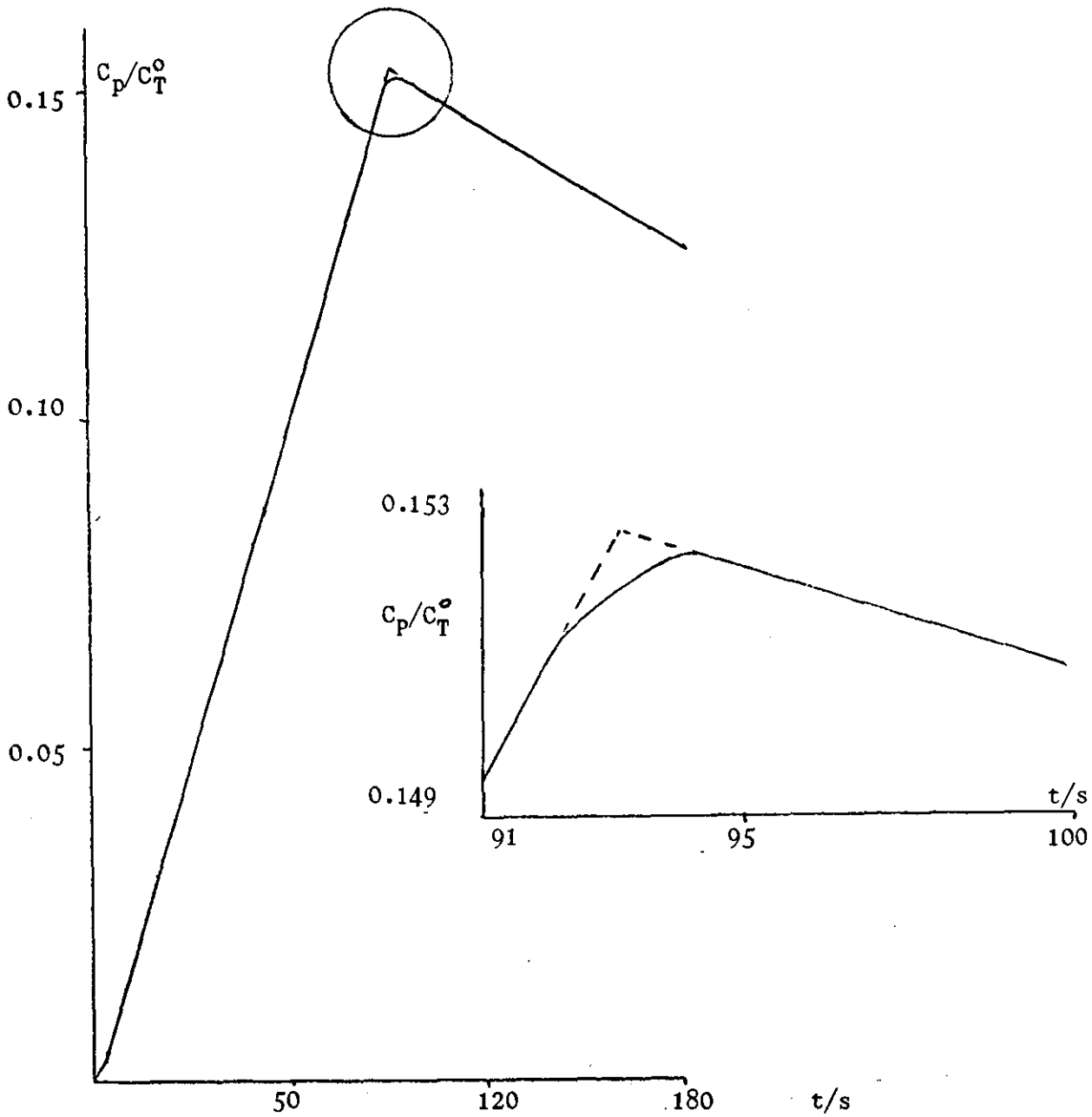

Fig. 5.18 Simulation of dispersion effect in flow titration

Following product t_e = 92s, m = 600s, C_T^o = 0.01M, $(C_p)_{max}$ = 1.533 x 10^{-3} M, τ_s = 1.2s. Curve to 92s follows eqn. 5.35, curve from 92 to 94.4 s follows eqn. 5.36, curve thereafter follows eqn. 5.21b.

Inset is expanded version of circled end-point region.

conditions used in this simulation mimic those in Fig. 5.15, thus on this evidence the curvature displayed in practice is somewhat greater than expected from dispersion alone.

As with the flow titration in which the analyte is monitored, the start of the titration is auto-indicated and no correction for transportation lag is required.

5.2.4.4 Physical Analogue of Dispersion

The essential physical nature of the dispersion effect is demonstrated in Fig. 5.19; where a ramp voltage input, functioning as the linear concentration gradient, is convoluted with a low-pass filter. The time constant of the filter circuit corresponds to the residence time (τ_s) of the mixing stage in the fractional tubularity model of the transmission line/detector system. Curves analogous to flow titrations are obtained.

5.2.5 Conclusion

Linear concentration gradients have been successfully used to perform flow photometric titrations in a variable volume tank reactor on self-indicating systems when the reaction involved is thermodynamically favourable. Titration curves are continuously recorded by this method and follow theoretical prediction. However, using an external detection system, dispersion and transportation lags are experienced but these effects can be accounted for. Precision is ultimately limited to that of the flow rates employed. Using peristaltic pumping, this precision is typically between one and two per cent. Rapid titrations are possible and the method has scope for automation.

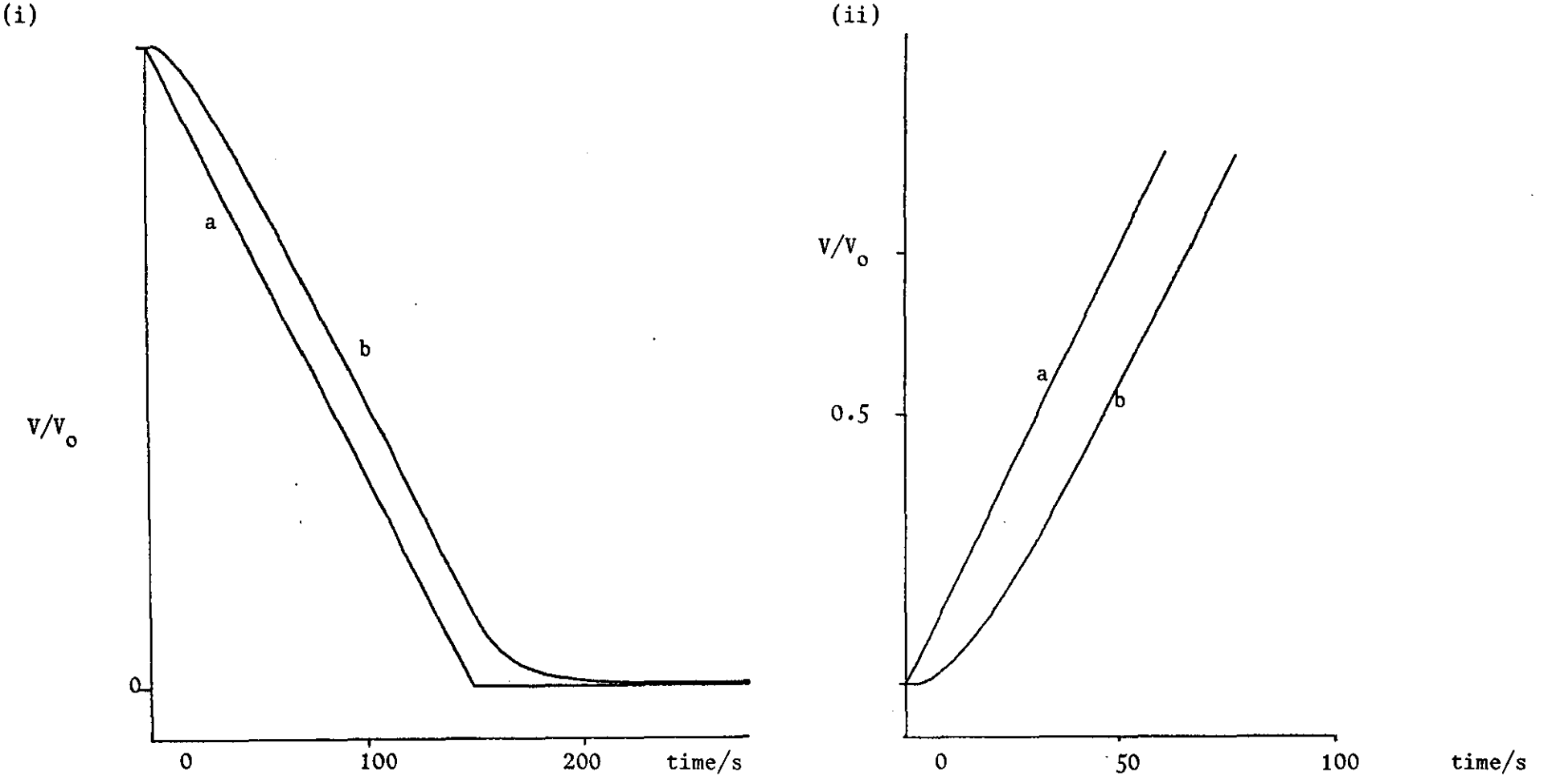

Fig. 5.19 Physical Analogues of Flow Titrations

Voltage ramps (V/V_o) produced by EDT Model ECP100 polargraph module, (i) at -5 mVs^{-1} and (ii) at 10 mVs^{-1}. 1 M Ω dummy resistance - (a) without filtering, (b) with low-pass filter in circuit, time constant = 10 s.
(i) Follow analyte simulation, Linear gradient = 6.7×10^{-3} s^{-1}, τ_s = 10s.
(ii) Follow titrant simulation, Linear gradient = 10^{-2} s^{-1}, τ_s = 10s.

Application of the method to titrations where the equivalence point is determined by potentiometric or chemical indicator means would introduce further considerations. Firstly, these titrations are based on p(Analyte) vs added titrant curves which would differ between batch and flow modes due to the dilution effect present in the latter mode. This effect would be most marked at short transition times. Secondly, both transportation and dispersion lags might be expected to produce an apparent titration time in excess of the true value. In this situation, an empirical calibration may be resorted to (139); but a better solution may be sought by the use of a triangular programmed gradient from a suitably designed flow manifold to copy the coulometric method of Pungor et. al. (40), to subtract out the error due to uncertain origin.

As well as these applications in titrimetry, linear gradients have potential application to methods requiring serial dilution, e.g. in the study of equilibria and in the production of calibration curves. The advantages of the continuous production of such dilutions has already been demonstrated using exponential gradients (35, 189).

LIST OF SYMBOLS

a	nozzle diameter (cm)
	tube radius
	titration factor
A	electrode area
	absorbance
A_1, A_2	consecutive cross-sectional tube areas in hydrostatic head manifold
b	electrode chamber depth (cm)
	volume of titrant added in a batch titration
C	concentration variable
C^o	undiluted concentration
C_o	original concentration in tank
C_1	tank feed concentration
C_A	analyte concentration
C_T	titrant concentration
C_p	product concentration
	concentration at FIA peak maximum
C_R^o	original reagent concentration
C_S^o	original sample concentration
C_d	coefficient of discharge
d	tube diameter
D	diffusion coefficient ($cm^2\ s^{-1}$)
D_S	sample dispersion coefficient
D_R	reagent dispersion coefficient
E	exit distribution of unit impulse function
$E_{1/4}$, $E_{1/2}$, $E_{3/4}$	quarter, half, three-quarter wave potentials
E_p	peak potential
$E^\ominus$	standard electrode potential
f	Volumetric flow rate
	fraction of peak signal
F	normalised response curve
	Faraday (96, 453, C mol^{-1})
g	acceleration due to gravity (9.81 ms^{-2})
h	hydrostatic head
I	input function
i_L	limiting current

i_p	peak current
i_r	residual current
i_s	stagnation current
i_{WJ}	wall-jet current
i_{TL}	thin-layer current
j	matrial flux
k, k'	numerical constants in hydrodynamic voltammetry
K_A	acid dissociation constant
K_f	formation constant
K_w	ionic product of water
l	electrode length
L	tube length
m	tank emptying time
n	number of tanks
	number of electrons transferred in electrode reaction
Pe	Peclet Number
r	electrode radial distance
	radial distance in tube
r_{Hg}	mercury drop radius
R	gas constant (8.314 JK^{-1} mol^{-1})
	electrode radius
R_o	stagnation zone radius
R_1	wall-jet zone radius
R_{max}	ratio of sample to reagent concentration at FIA peak maximum
Re	Reynolds Number
S	signal variable
S^o	steady state signal value
Sc	Schmidt Number
Sh	Sherwood Number
t	time variable
t_A	appearance time
t_e	equivalence time
t_p	transportation lag time
t'	dummy time variable
	reduced time

U	linear velocity
U_o	maximum linear velocity
V	volume variable
V_o	original tank volume
V_c	volume of electrode channel
	capacitor voltage in FI electrical analogue
V_D	effective detector volume
V_f	volumetric flow rate (ml min^{-1})
V_L	volume of delivery line
V_s	volume of injected sample
	volume of mixing stage
V_p	plug flow volume
V_A	volume of analyte in batch titration
V_T	volume of titrant in batch titration
v	voltage sweep rate
W	normalised wash curve
w	electrode width
x	radial distance from centre of electrode (cm)
α	Reynolds Number flow exponent
β	Schmidt Number flow exponent
δ_{bl}	boundary layer thickness
δ_{dL}	diffusion layer thickness
η	coefficient of viscosity (kg m^{-1} s^{-1})
ν	kinematic viscosity of supporting electrolyte ($cm^2 s$)
	sine-wave frequency defining recorder response time
ρ	density (kg m^{-3})
σ^2	variance
τ	residence time
τ_D	detector response time
τ_s	residence time in mixing stage
ϕ	accommodation factor
ϕ_v	volumetric flow rate (cm^3 s^{-1})

REFERENCES

1. Cussler, E.L., "Diffusion", C.U.P., Chapter 3, 1984
2. Levich, V.G., "Physicochemical Hydrodynamics", Prentice-Hall, Chapter 2, 1962
3. Frenzel, W., Analyst, 1988, 113, 1039
4. Skeggs, L.T., Am. J. Clin. Pathol., 1957, 28, 311
5. Nagy, G., Feher, Z. and Pungor, E., Anal. Chim. Acta., 1970, 52, 47
6. Ruzicka, J., and Hansen, E.H., Anal. Chim. Acta., 1975, 78, 145
7. Tyson, J.F., Analyst, 1984, 109, 319
8. Karlberg, B. and Thelander, S., Anal. Chim. Acta., 1980, 114, 129
9. Tyson, J.F., Appleton, J.H.M., and Idris, A.B., Anal. Chim. Acta., 1983, 145, 159
10. Vanderslice, J.T. Beecher, G.R., and Rosenfeld, A.G., Anal. Chem., 1984, 56, 268
11. Nekimken, H.L., Smith, B.F., Jarvinen, G.D., Petersen, E.J., and Jones, M.M., Anal. Chem. 1988, 60, 1390
12. Reis, B.F., Bergamin F°. H., Zagatto, E.A.G., and Krug, F.J., Anal. Chim. Acta., 1979, 107, 309
13. Johnson, K.S., and Petty, R.L., Anal. Chem., 1982, 54, 1185
14. Fogg, A.G., Analyst, 1986, 111, 859
15. Riley, C., Rooks, B.F., and Sherwood, R.A., Anal. Chim. Acta., 1986, 179, 69.
16. Ruzicka, J., and Hansen E.H., Anal. Chim. Acta., 1978, 99, 37.
17. Janata, J., and Ruzicka, J., Anal. Chim. Acta., 1982, 139, 105
18. Rios, A., de Castro, M.D.L., and Valcarcel, M., J. Chem., Ed., 1986, 63, 552
19. Betteridge, D., Oates, P.B. and Wade, A.P., Anal. Chem., 1987, 59, 1236
20. Basson, W.D., and van Standen, J.F., Analyst, 1979, 104, 419

21. Ekstrom, L.G., J.A.O.C.S. 1981, 58, 1988
22. Memon, M.H. and Worsfold, P.J., Anal. Proc., 1986, 23, 418
23. Canete, F., Rios, A., de Castro, M.D.L., and Valcarcel M., Anal. Chem., 1988, 60, 2354
24. Valcarcel, M., and Gallego, M., Trends in Anal. Chem., 1988, 8, 34
25. Cook, I.G., McLeod, C.W., and Worsfold, P.J., Anal. Proc., 1986, 23, 5
26. Cremonesi, P., and Bovara, R., Biotechn. Bioeng., 1976, 16, 1487
27. Gine, M.F., Bergamin, F°. H., Zagatto, E.A.G., Reiss B.F., Anal. Chim. Acta., 1980, 114, 191
28. Faizullah, A.T., and Townshend, A., Anal. Chim. Acta., 1986, 179, 233
29. Hauser, P.C., Tan, S.S., Cadwell, T.J., Cottrall, W.S., and Hamilton, I.S., Analyst, 1988, 113, 1551
30. Linares, P., de Castro, M.D.L., and Valcarcel, M., Anal. Chem., 1985, 57, 2101
31. Masoom, M., and Townshend, A., Anal. Proc., 1985, 22, 6
32. Levenspiel, O., "Chemical Reaction Engineering" 2nd ed. Wiley, 1972, Chapter 9
33. Horvai, G., Toth, K., and Pungor, E., Anal. Chim. Acta., 1976, 82, 45
34. Scott, R.P.W., "Liquid Chromatography Detectors", Elsevier, 2nd ed. 1986, Chapter 2
35. Miller, J.N., Abdullahi, G.L., Sturley, H.N., Gossain, V. and McCluskey, P.L., Anal. Chim. Acta. 1986, 179, 81
36. Pungor, E., Feher, Z., Nagy, G., Toth, K., Horvai, G., and Gratzl, M., Anal. Chim. Acta., 1979, 109, 1
37. Pardue, H.L., and Fields, B., Anal. Chim. Acta., 1981, 124, 39, 65
38. Pardue, H.L., and Jager, P., Anal. Chim. Acta., 1986, 179, 169.
39. Ruzicka, J., Hansen, E.H., and Mosbaek, H., Anal. Chim. Acta., 1977, 92, 235

40. Gisin, M., and Thommen, C., Trends in Anal. Chem., 1989, 8, 62.
41. Ruzicka, J., and Hansen, E.H., Anal. Chim. Acta. 1978, 99, 37
42. Reijn, J.M., Van der Linden, W.E., and Poppe H., Anal. Chim. Acta., 1981, 126, 1
43. Tijssen, R., Anal. Chim. Acta., 1980, 114, 71
44. Kagenow, H., and Jensen, A., Anal. Chim. Acta, 1980, 114, 227
45. Kobayashi, S., and Imai, K., Anal. Chem., 1980, 52, 1548
46. Clark, G.D., Hungerford, J.M., and Christian, G.D., Anal. Chem., 1989, 61, 973
47. Nagy, G., Toth, K., and Pungor, E., Anal. Chem., 1975, 47, 1460
48. Taylor, G.I., Proc. Roy. Soc. 1953, 219A, 186
49. Ananthakrishnan, V., Gill, W.N., and Barduhn, A.J., A.I.Ch.E.J., 1965, 11, 1063
50. Bate, H., Rowlands, S., Sirs, J.A., and Thomas, H.W., Brit.J. Appl. Phys. (J.Phys.D.), 1969, 2, 1447
51. Bate, H., Rowlands, S., and Sirs, J.A., J. Appl. Physiol., 1973, 34, 866
52. Golay, M.J.E., and Atwood, J.G., J. Chromatography, 1979, 186, 353
53. Atwood, J.G., and Golay, M.J.E., J. Chromatography, 1981, 218, 97
54. Vanderslice, J.T., Stewart, K.K., Rosenfeld, A.G., and Higgs, D.J. Talanta, 1981, 28, 11
55. Vanderslice, J.T., Rosenfeld, A.G., and Beecher, G.R., Anal. Chim. Acta., 1986, 179, 119
56. Wada, H., Hiraoka, S., Yuchi, A., and Nakagawa, G., Anal. Chim. Acta., 1986, 179, 181
57. Horvai, G., and Pungor, E., C.R.C. Crit. Rev. Anal. Chem., 1987, 17, 231
58. Gomez-Nieto, M.A., de Castro, M.D.L., and Valcarcel, M., Talanta, 1985, 32, 319
59. Vanderslice, J.T., and Beecher, G.R., Talanta, 1985, 32, 334

60. Tyson, J.F., and Idris, A.B., Analyst, 1981, 106, 1125
61. Denbigh, K.G., and Turner, J.C.R., "Chemical Reactor Theory", C.U.P., 3rd ed. 1984, Chapter 5
62. Stone, D.C., and Tyson, J.F., Analyst, 1987, 112, 515
63. Stone, D.C., and Tyson, J.F., Anal. Chim. Acta., 1986, 179, 427
64. Tyson, J.F., Anal. Chim. Acta., 1986, 179, 131
65. Betteridge, D., Marczewski, C.Z., and Wade, A.P., Anal. Chim. Acta., 1984, 165, 227
66. Janse, T.A.H.M., van der Wiel, P.F.A. and Kateman, G., Anal. Chim. Acta., 1983, 155, 89
67. Betteridge, D., Taylor, A.F., and Wade, A.P., Anal. Proc., 1984, 21, 373
68. Flow Injection Analysis Bibliography, Tecator Ltd., 1985
69. Reijn, J.M., Van der Linden, W.E., and Poppe, H., Anal. Chim. Acta., 1980, 114, 105
70. Sternberg, J.C., in "Advances in Chromatography" ed. Giddings, J.C., Keller, R.A., M. Dekker, 1966, p.205
71. Larkins, L.A., and Westcott, S.G., Anal. Proc., 1986, 23, 258
72. Curran, D.J., and Tougas, T.P., Anal. Chem., 1984, 56, 672
73. Appleton, J.M.H., and Tyson, J.F., J.A.A.S, 1986, 1, 63
74. Stulik, K., and Pacakova, V., "Electroanalytical Measurements in Flowing Liquids", Ellis Horwood, 1987, Chapters 2 and 3
75. Blaedel, W.J., and Todd, J.W., Anal. Chem., 1958, 30, 1821
76. Blaedel, W.J., and Strohl, J.H., Anal. Chem., 1964, 36, 445
77. Scarano, E., Bonicelli, M.G. and Forina, M., Anal. Chem., 1970, 42, 1470
78. Forina, M., Ann. Chim., 1973, 63, 763
79. Hanekamp, H.B., Bos, P., Brinkman, U.A.Th., and Frei, R.W., Fres. Zeit. Anal. Chem. 1979, 297, 404
80. Dieker, J.W., Van der Linden, W.E., and Poppe, H., Talanta, 1979, 26, 511

81. Dieker, J.W., and Van der Linden, W.E., Anal. Chim. Acta., 1980, 114, 267
82. Kutzner, W., Debrowski, J., and Kemula, W., J.Chromatography, 1980, 191, 47
83. Brunt, K., Analyst, 1982, 107, 1261
84. Stulik, K., and Pacakova, V., Ann. Chim., 1986, 76, 315
85. Kristensen, E.W., Wilson, R.L. and Wightman, R.M., Anal. Chem., 1986, 58, 986
86. Kristensen, E.W., Kuhr, W.G., and Wightman, R.M., Anal. Chem., 1987, 59, 1752
87. Hanekamp, H.B., and van Nieuwerk, H.J., Anal. Chim. Acta., 1980, 121, 13
88. Blaedel, W.J., Olson, C.L., and Sharma, L.R., Anal. Chem., 1963, 35, 2100
89. Wranglen, G., and Nilsson, O., Electrochim. Acta., 1962, 7, 121
90. Elbicki, J.M., Morgan, D.M., and Weber, S.G., Anal. Chem. 1984, 56, 978
91. Dalhuijsen, A.J., van der Meer, Th.H., Hoogendorn, C.J., Hooguliet, J.G., and van Benekom, W.P., J. Electroanal. Chem., 1985, 182, 295
92. Marchiano, S.L., and Arvia, A.J., Electrochim. Acta., 1967, 12, 801
93. Matsuda, H., J. Electroanal. Chem., 1967, 15, 109
94. Yamada, J., and Matsuda, H., J. Electroanal. Chem., 1973, 44, 189
95. Hanekamp, H.B., and de Jong, H.G., Anal. Chim. Acta., 1982, 135, 351
96. Blaedel, W.J., and Iverson, D.G., Anal. Chem., 1977, 49, 1563
97. Meschi, P.L. and Johnson D.C., Anal. Chem., 1980, 52, 1304
98. Weber, S.G., J. Electroanal. Chem., 1983, 145, 1
99. Brunt, K., and Bruins, C.H.P., J. Chromatography, 1979, 172, 37

100. Matsuda, H., and Yamada, J., J. Electroanal. Chem., 1971, 30, 261
101. Coeuert, F., Chem. Eng. Sci., 1975, 30, 1257
102. Chin, D-T. and Tsang, C-H., J. Electrochem. Soc., 1978, 125, 1461
103. Olson, J.B. and Koval, C.A., Anal. Chem., 1988, 60, 88
104. Glauert, M.B., J. Fluid Mechs. 1956, 1, 625
105. Gunasingham, H., and Fleet, B., Anal. Chem., 1983, 55, 1409
106. Gunasingham, H., Tay, B.T., and Ang, K.P., Anal. Chem., 1984, 56, 2422
107. Meschi, P.L., and Johnson, D.C., Anal. Chim. Acta., 1981, 124, 303
108. Prabhu, S., and Anderson, J.L., Anal. Chem., 1987, 59, 157
109. Stulik, K. and Pacakova, V., "Electroanalytical Measurements in Flowing Liquids", Ellis Horwood, 1987, Ch.6
110. Zittel, H.E., and Miller, F.J., Anal. Chem., 1965, 37, 200
111. Wang, J., Golden, T., and Li, R., Anal Chem., 1988, 60, 1642
112. Cosgrove, M., Moody, G.J. and Thomas, J.D.R., Analyst, 1988, 113, 1811
113. Moody, G.J., Sanghera, G.S. and Thomas, J.D.R., Analyst, 1986, 111, 1235
114. Fogg, A.G., Chamsi, A.Y. and Abdalla, M.A., Analyst, 1983, 108, 464
115. Fogg, A.G., Scullion, S.P., and Edmonds, T.E., Analyst, 1989, 114, 579
116. Fogg, A.G., Ali, M.A. and Abdalla, M.A., Analyst, 1983, 108, 840
117. Fogg, A.G., Chamsi, A.Y., Barros, A.A., and Cabral, J.O., Analyst, 1984, 109, 901
118. Chamsi, A.Y., and Fogg, A.G., Analyst, 1986, 111, 879
119. Abdalla, M.A. and Hassan, M.A., Analyst, 1989, 114, 583
120. Fogg, A.G. and Bsebsu, N.K., Analyst, 1984, 109, 19
121. Fogg, A.G., Fernandez-Arciniega, M.A., and Alonso, R.M., Analyst, 1985, 110, 345, 1201

122. Wolff, C-M, and Mottola, H.A., Anal. Chem., 1977, 49, 2118
123. Lown, J.A., Koile, R., and Johnson, D.C., Anal. Chim. Acta., 1980, 116, 33
124. Hangos-Mahr, H., and Pungor, E., in "Modern Trends in Analytical Chemistry", ed. Pungor, E., and Buzas, I., Elsevier, 1984, p.307
125. Tougas, T.P., Jannetti, J.M., and Collier, W.G., Anal. Chem., 1985, 57, 1377
126. Roe, D.K., Anal. Letters, 1983, 16, 631
127. Abresch, K., and Claasen, I., "Coulometric Analysis", Chapman and Hall, 1965, p.125
128. Blaedel, W.J., and Laessig, R.H., Anal. Chem., 1984, 36, 1617
129. Jola, M., Chimia,1979, 33, 208
130. Abicht, S.M., Anal. Chim. Acta., 1980, 114, 247
131. Arnold, D.P., Peachey, R.M., Petty, J.D., and Sweatman, D.R., Anal. Chem., 1989, 61, 2109
132. Sorin, B., and Vargues, R., Ann. Biol. Clin., 1966, 24, 995
133. Eichler, D.L., "Technician Symposium 1969", Vol. 1, Medaid Inc., New York, 1970, p.51
134. Fleet, B., and Ho, A.Y.W., Anal. Chem., 1974, 46, 9
135. Nagy, G., Feher, Z., Toth, K., and Pungor, E., Anal. Chim. Acta., 1977, 91, 97
136. Nagy, G., Feher, Z., Toth, K., and Pungor. E., Anal. Chim. Acta., 1978, 100, 181
137. Feher, Z., Nagy, G., Toth, K., Pungor, E., and Toth, A., Analyst, 1979, 104, 560
138. Feher, Z., Kolbe, I., and Pungor, E., Analyst, 1988, 113, 881
139. Bound, G.P., and Fleet, B., Talanta, 1980, 27, 257
140. Stewart, K.K., and Rosenfeld, A.G., Anal. Chem., 1982, 54, 2368
141. Koupparis, M.A., Anagnostopoulou, P., and Malmstadt, H.V., Talanta, 1985, 32, 311

142. Turner, D.R., Knox, S., Whitfield, M., and dos Santos, M.C., Anal. Proc., 1987, 24, 360
143. Ramsing, A.U., Ruzicka, J., and Hansen, E.H., Anal. Chim. Acta, 1981, 129, 1
144. Woods, B.A., Ruzicka, J., and Christian, G.D., Anal. Chem., 1987, 59, 2767
145. Tyson, J.F., Analyst, 1987, 112, 523
146. Fogg, A.G., and Summan, A.M., Analyst, 1984, 109, 1029
147. Engstrom, R.C., Anal. Chem., 1982, 54, 2310
148. Engstrom, R.C., and Strasser, V.A., Anal. Chem., 1984, 56, 136
149. Poon, M., and McCreery, R.L., Anal. Chem., 1986, 58, 2745
150. Bergamin, F°. H., Reis, B.F., and Zagatto, E.A.G., Anal. Chim. Acta., 1978, 97, 427
151. MacKoul, D., Johnson, D.C., and Schick, K.G., Anal. Chem., 1984, 56, 436
152. Massey, B.S., "Mechanics of Fluids", Van Nostrand, 5th ed., 1983, Chapters 6 and 7.
153. Sheppard, C.W., "Basic Principles of the Tracer Method", Wiley 1962, Chapter 6.
154. McWilliam, I.G. and Bolton, H.G., Anal. Chem., 1969, 41, 1762
155. Poppe, H., Anal. Chim. Acta., 1980, 114, 59
156. Wang, J., J. Chem. Ed., 1982, 59, 691
157. Wang, J., and Dewald, H.H., Anal. Chim. Acta., 1982, 136, 77
158. Miller, J.C., and Miller, J.N., "Statistics for Analytical Chemistry", Wiley, 1984, Chapter 3.
159. Alder, J.F., Fleet, B., and Kane, P.O., J. Electroanal Chem., 1971, 30, 427
160. Panzer, R.E., and Elving, P.J., J. Electrochem. Soc., 1972, 109, 864
161. Adams, R.N., "Electrochemistry at Solid Electrodes", M. Dekker, 1969, Chapter 5.
162. Noel, M., and Anantharaman, P.N., Analyst, 1985, 110, 1095

163. Delahay, P., "New Instrumental Methods in Electrochemistry", Interscience, 1954, Ch. 6
164. Gerhardt, G., and Adams, R.N., Anal. Chem., 1982, 54, 2618
165. Koryta, J., Dvorak, J., and Bohackova, V., "Electrochemistry", Metheun, 1970, Chapter IIc.
166. Hubbard, A.T., and Anson, F.C., Anal. Chem., 1966, 38, 58
167. Keller, H.E. and Reinmuth, W.H., Anal. Chem., 1972, 44, 434
168. Caja, J., Czerwinski, A., Rubinson, K.A., Heinemann, W.R., and Mark, H.B., Anal. Chem., 1980, 52, 1010
169. Tougas, T.P., and Curran, D.J., Anal. Chim. Acta., 1984, 161, 325
170. Mason, W.D., Gardner, T.D., and Stewart, J.T., J. Pharm. Sci., 1972, 61, 1301
171. Koryta, J., Dvorak, J., and Bohackova, V., "Electrochemistry", Metheun, 1970, Chapters I, III.
172. Thornton, D.C., Corby, K.T., Spendel, V.A., Jordan, J., Robbat, A., Rustrom, D.J., Gross, M., and Ritzler, G., Anal. Chem., 1985, 57, 150
173. Rusling, J.F., Anal. Chem., 1984, 56, 575
174. Birkhoff, G., and Zarantonello, E.H., "Jets, Wakes and Cavities", Academic Press, 1957, pp. 259-272
175. Scholtz, M.T., and Trass, O., A.I. Ch.E.J., 1970, 16, 90
176. Brunt, K., Bruins, C.H.P., Doornbos, D.A., and Oosterhuis, B., Anal. Chim. Acta., 1980, 114, 257
177. Stulik, K., and Pacakova, V., J. Chromatography, 1981, 208, 269
178. Vandenheuvel, F.A., Anal. Chem., 1963, 35, 1193
179. Sweetser, P.B., and Bricker, C.E., Anal. Chem., 1953, 25, 253
180. Sykes, A.G., "Kinetics of Inorganic Reactions", Pergamon, 1966, p.244
181. Underwood, A.L., J.Chem. Ed., 1954, 31, 394
182. Lewin, S.Z., and Wagner, R.S., J.Chem. Ed., 1953, 30, 445
183. Hill, Z.D., and MacCarthy, P., J.Chem. Ed., 1986, 63, 162
184. Goddu, R.F. and Hume, D.N., Anal. Chem., 1954, 26, 1679

185. Albert, A., and Serjeant, E.P. "The Determination of Ionisation Constants", Chapman and Hall, Third Edition, 1984, p.145
186. Ayad, S.R., Bonsall, R.W., and Hunt, S., Anal. Biochem., 1968, 22, 533
187. Naumann, E.B., and Buffham, V.A., "Mixing in Continuous Flow Systems", Wiley, 1983, Chapter 1.
188. Ibid, Chapter 5.
189. Tyson, J.F., and Appleton, J.M.H., Talanta, 1984, 31, 9
190. Miller, J.C., and Miller, J.N., "Statistics for Analytical Chemistry", Ellis Horwood, 1984, Chaper 2.
191. Naumann, E.B., and Buffham, B.A. "Mixing in Continouous Flow Systems", Wiley, 1983, Chapter 2.
192. Simon, W., "Mathematical Techniques for Biology and Medicine", Dover, 1986, Chapter 5.
193. Campbell, D.C., "Process Dynamics", Wiley, 1958, p.22
194. Miller, J.C., and Miller, J.N., "Statistics for Analytical Chemistry", Ellis Horwood, 1984, Chapter 4.
195. Flaschka, H., Talanta, 1961, 8, 381
196. Job, P., Ann. Chim., 1928, 9, 113
197. Langmyhr, F.J., and Myhrstad, J.A., Anal. Chim. Acta., 1966, 35, 212
198. Moser, W., Chalmers, R.A., and Fogg, A.G., J. Inorg. Nucl. Chem., 1965, 27, 831
199. Leonard, M.A., in "Comprehensive Analytical Chemistry", Vol. VIII, ed. Svehla, G., Elsevier, 1977, Chapter 3.